Phase equilibria and thermochemical studies on oxide fuel materials

By

RIMPI DAWAR

(Enrolment No: CHEM02201104005)

Indira Gandhi Centre for Atomic Research, Kalpakkam

A thesis submitted to the

Board of Studies in Chemical Sciences

In partial fulfillment of requirements
for the Degree of

DOCTOR OF PHILOSOPHY
of
HOMI BHABHA NATIONAL INSTITUTE

August 2017

Homi Bhabha National Institute

Recommendations of the Viva Voce Committee

As members of the Viva Voce Committee, we certify that we have read the dissertation prepared by **Rimpi Dawar** entitled "**Phase equilibria and thermochemical studies on oxide fuel materials**" and recommend that it may be accepted as fulfilling the thesis requirement for the award of Degree of Doctor of Philosophy.

Chairman – Dr. M. Joseph	**Date:**
Guide / Convener – Dr. S. Anthonysamy	**Date:**
Examiner -	**Date:**
Member 1- Dr. T. S. Lakshmi Narasimhan	**Date:**
Member 2- Dr. N. V. Chandrasekhar	**Date:**

Final approval and acceptance of this thesis is contingent upon the candidate's submission of the final copies of the thesis to HBNI.

I/We hereby certify that I/we have read this thesis prepared under my/our direction and recommend that it may be accepted as fulfilling the thesis requirement.

Date:

Place:

Dr. S. Anthonysamy
Guide

STATEMENT BY AUTHOR

This dissertation has been submitted in partial fulfillment of requirements for an advanced degree at Homi Bhabha National Institute (HBNI) and is deposited in the Library to be made available to borrowers under rules of the HBNI.

Brief quotations from this dissertation are allowable without special permission, provided that accurate acknowledgement of source is made. Requests for permission for extended quotation from or reproduction of this manuscript in whole or in part may be granted by the Competent Authority of HBNI when in his or her judgment the proposed use of the material is in the interests of scholarship. In all other instances, however, permission must be obtained from the author.

Rimpi Dawar

DECLARATION

I, hereby declare that the investigation presented in the thesis has been carried out by me. The work is original and has not been submitted earlier as a whole or in part for a degree / diploma at this or any other Institution / University.

Rimpi Dawar

List of Publications arising from the thesis

Journals

1. **Chemical potential of oxygen in (U, Pu) mixed oxide with Pu/(U+Pu) = 0.46**

   Rimpi Dawar, V. Chandramouli, S. Anthonysamy

   Journal of Nuclear Materials, 2016, 473, 181.

2. **Thermodynamic characterization of Fe_2TeO_6**

   Rimpi Dawar, Ashish Jain, R. Babu, K. Ananthasivan, S. Anthonysamy

   Journal of Thermal Analysis and Calorimetry, 2015, 122(2), 885.

3. **Thermodynamic Characterization of Chromium tellurate**

   Rimpi Dawar, R. Pankajavalli, Jose Joseph, S. Anthonysamy, V. Ganesan

   Journal of Thermal Analysis and Calorimetry, 2013, 112(1), 95.

4. **Thermodynamic Characterization of Ni_3TeO_6, $Ni_2Te_3O_8$ and $NiTe_2O_5$**

   Rimpi Dawar, R. Babu, K. Ananthasivan, S. Anthonysamy

   Journal of Nuclear Materials, 2017, 493, 219.

5. **Kinetics of formation of lanthanum tellurate**

   Rimpi Dawar, S. Anthonysamy

   Journal of Thermal Analysis and Calorimetry, 2017, 29(3), 1823.

Manuscript Under Preparation:

6. **Thermochemical Studies On The System Cr-Te-O**

   Rimpi Dawar, S. Anthonysamy

Conferences

1. **Oxygen Potential of (U,Pu) mixed oxides**

   Rimpi Dawar, V. Chandramouli, S. Anthonysamy, P. R. Vasudeva Rao

   Paper presented at IGW-HTC-14, 3-4th November, 2014.

2. **Thermochemical Studies on Cr-Te-O system**

   Rimpi Dawar, S. Anthonysamy

   Paper presented at 11th ISEAC-DM, Amritsar, 20-25th February, 2014.

3. **Thermodynamic Functions of Iron Tellurate**

   Rimpi Dawar, R. Babu, K. Ananthasivan and S. Anthonysamy

   Paper presented at Thermans, BARC, Mumbai, 19-21st December, 2013.

4. **Thermodynamic Characterization of Iron Tellurate**

   Rimpi Dawar, Ashish Jain, R. Pankajavalli and S. Anthonysamy

   Paper presented at RTMC, VIT Vellore, 25-27th July, 2013.

5. **Thermochemical studies on Chromium tellurate**

   Rimpi Dawar, R. Pankajavalli, A. Jain, S. Anthonysamy and V. Ganesan

   Paper presented at Thermans-2012, 31 Jan-2 Feb, BARC Mumbai

6. **Kinetics of formation of lanthanum tellurate**

   Rimpi Dawar, Kitheri Joseph, Ashish Jain , S. Anthonysamy and V. Ganesan

   Paper presented at ICVC-2011, 11-13th October, IGCAR Kalpakkam.

Rimpi Dawar

Dedicated To My Beloved
“Parents”

ACKNOWLEDGEMENTS

I express my sincere thanks to my Ph.D. supervisor **Dr. S. Anthonysamy,** for his guidance, constant support, and valuable suggestions to improve the quality of work throughout my tenure. His innovative ideas, immense knowledge and keen interest made my research work challenging and stimulating. His mentorship and consolidated review have lead to the successful completion of the thesis work.

I take immense pleasure in thanking **Dr. V. Chandramouli** and **Dr. N. Pankajavalli** for their keen assessment of work, support, guidance, valuable suggestions and constant encouragement.

I am pleased to express my deep sense of gratitude to my doctoral committee chairman, **Dr. M. Joseph** and members **Dr. T. S. Lakshmi Narasimhan, Dr. N. V. Chandrashekar** for their valuable suggestions.

I would like to thank **Dr. Kitheri Joseph, Dr. M. V. Krishnaiah, Dr. T. Gnanasekhran, Dr. R. Asuvathraman** and **Dr. K. Ananthasivan** for the many useful suggestions.

I wish to express my special thanks to **Dr. R. Ganesan** for his constant support, kind help and valuable suggestions during fabrication of oxygen sensor for oxygen potential measurement experiments.

I also wish to express my special thanks to **Mr. G. Saravanan, Mr. P. Ravi Sankar** for their help and support in oxygen potential measurement experiments carried out in a glove box meant for handling radioactive materials.

I express my sincere thanks to **Dr. R. Sudha, Mr. Raja Madhvan, Dr. G. Paneer selvam, Dr. H. N. Jena** for their help in experimental work.

I am grateful to my colleagues **Mrs. Soja K. Vijay, Dr. Ashish Jain, Dr. Rahul Pal, Mrs. N. Ambika, Dr. R. Babu, Mr. Sanjay Kumar, Mr. V. Paramsivam, Mr.**

Ramamoorthy for their co-operation in the lab which helped me to plan and execute the experiments meticulously.

I am pleased to acknowledge committed cooperation my friends **Annie, Sreenivasulu Balija, Rama Krishna Pagoti, Prasant, Meera and Aishwarya** for their timely help in crucial moments. The lively environment provided by them was a real driving force for me.

I have praise galore for my husband **Tarun,** my beloved daughter **Radhika** and my parents **Sh. Rajinder, Mrs. Usha** for their constant support and encouragement in all my endeavors. I thank them most sincerely.

Above all, from the depth of my heart I express my deep and sincere thanks to the Almighty for his countless blessings upon me.

Rimpi Dawar

August, 2017

CONTENTS

CHAPTER 1

INTRODUCTION

CHAPTER 2

EXPERIMENTAL

CHAPTER 3

MEASUREMENT OF OXYGEN POTENTIAL OF URANIA-PLUTONIA SOLID SOLUTION $(U_{0.54}Pu_{0.46})O_{2-x}$

CHAPTER 4

THERMODYNAMIC STABILITY OF Cr_2TeO_6, Fe_2TeO_6, Ni_3TeO_6 BY TRANSPIRATION TECHNIQUE

CHAPTER 5

THERMOCHEMICAL STUDIES ON Cr-Te-O SYSTEM USING EMF TECHNIQUE

CHAPTER 6

THERMOCHEMICAL STUDIES ON Cr_2TeO_6, Fe_2TeO_6, Ni_3TeO_6, $Ni_2Te_3O_8$ AND $NiTe_2O_5$ USING CALORIMETRIC TECHNIQUE

CHAPTER 7

KINETICS OF FORMATION OF La_2TeO_6

CHAPTER 8

SUMMARY AND CONCLUSIONS

CHAPTER 9

FUTURE PERSPECTIVES

SYNOPSIS

In the developing country like India, nuclear energy plays an important role in meeting energy demand. Presently nuclear energy contribution in India is only about 3% to the total electricity generation [1]. Nuclear energy is considered to be clean energy because operation of nuclear reactor involves negligible greenhouse gases [2]. Also the energy density of nuclear fuels is million times higher than fossil fuels which reduces fuel requirement for nuclear reactor tremendously. India envisages three stage nuclear power programme using its naturally occurring uranium and vast thorium resources. In the first stage, power is derived from the uranium resources (energy released during the fission of ^{235}U isotope) using thermal reactors (LWR, BWR and PHWR). Natural uranium available in the earth crust contains only 0.7% ^{235}U (fissile isotope) and the rest 99.3% ^{238}U (fertile isotope). The uranium can be effectively utilised (~ 60-70%) in stage 2 i.e. in a fast reactor / fast breeder reactor (FBR). ^{238}U can be effectively converted to ^{239}Pu in a fast reactor with closed fuel cycle facility. The ^{239}Pu thus produced can be employed as fuel in subsequent reactors. In this stage another fertile isotope ^{232}Th (used in blanket material) can be converted to fissile isotope ^{233}U by the neutron capture reaction. ^{233}U thus produced in stage 2 will be used as fuel for stage 3 reactors. India has vast resources of thorium; hence, through this indigenous approach of coupling limited uranium reserves with vast thorium reserves our long term energy need can be fulfilled. Presently India is in its 2nd stage (FBRs) of nuclear power programme. In Fast reactors U and Pu mixed oxide/carbide/nitride or metallic alloys are employed as fuel and thorium as the blanket. Fast reactor programme was initiated in 1975 in India and the Fast Breeder Test Reactor (FBTR) was commissioned in 1985 which uses uranium and plutonium mixed carbide as the fuel [3]. The forms of fuel employed in nuclear reactor can be oxide, carbide, nitride, metal/alloy etc. In ceramics, carbides and nitrides have advantages of high breeding ratio, high thermal conductivity, high melting point but difficult to fabricate and reprocess. Oxides have high melting point, reasonably good compatibility with cladding material and coolant, considerable resistance to radiation damage. They are easy to fabricate and reprocess. There is well proven worldwide operational experience on oxides. The use of any material as the fuel in a nuclear reactor calls for very accurate measurement of its physicochemical properties viz., heat capacity, thermal conductivity, thermal expansion, free energy, entropy, enthalpy, vaporization behaviour and their variation with temperature. Among these, oxygen potential, which is a measure of driving force for numerous reactions that take place inside the fuel pin during irradiation, is very important property for oxide fuels [4, 5]. Oxygen potential controls vapour pressure inside fuel pin and redistribution of oxygen and actinides. Thermal conductivity of the fuel is a strong function of oxygen-to-metal ratio (O/M) which depends upon oxygen potential. It controls chemical state of fission products, their interaction with fuel and clad material (FCCI). In case of any breach interaction between fuel and coolant is also controlled by oxygen potential. FCCI is one of the important factors which decide the life time of fuel pin during irradiation. The thermochemical property which decides extent of FCCI is oxygen potential. The (uranium, plutonium) mixed oxide (MOX) containing up to 30 mol.% plutonia is considered as conventional fuel for fast reactors. Oxygen potential data of MOX containing up to 30 mol.% plutonia are available in literature. In the Fast breeder test reactor (FBTR), India 8 fuel subassemblies containing $(U, Pu)O_2$ having Pu content 45 mol.% are being irradiated [6]. The irradiation testing of this high plutonia content fuel in FBTR needs an understanding of the physicochemical properties of the fuel. Hence, in the present study, oxygen potential of $(U_{0.54} Pu_{0.46})O_{2-x}$ has been measured experimentally. In addition to oxygen potential, reactivity of various volatile fission products is of particular importance in the prediction of high-temperature fuel behaviour. A complete understanding (thermodynamically as well as kinetically) of FCCI in-reactor conditions is hence, necessary. There are economic incentives involved in selecting thickness of clad tube. If clad thickness is made more to accommodate FCCI, the breeding gain would reduce and system doubling time would increase (lesser thickness leads to more efficient heat transfer) [7]. But clad thickness has to be optimum taking into consideration FCCI. Among volatile fission products Tellurium (Te) is highly reactive whose interaction needs to be studied for complete understanding of clad corrosion [8]. Because of its volatile nature it has been found in fuel clad gap. Depending upon oxygen potential and tellurium potential prevailing inside the fuel pin formation of various compounds in M-Te-O (M is constituent of clad i.e., SS316) can take place which leads to intragranular corrosion (IGC) of clad. Hence, thermochemical data of the compounds formed in the systems M-Te-O (M = Fe, Cr, Ni) are essential. The thermochemical properties such as enthalpy and heat capacity are required for reactor safety calculations. Hence, in the present study, thermochemical stability of some of the ternary tellurates and tellurites has been determined. Since thermochemical data are applicable to equilibrium conditions, conditions inside the fuel pin viz., varying temperature, continuous generation of fission products etc. represent non equilibrium nature. In these conditions, along with thermodynamic stability, kinetics of formation of these compounds plays a vital role. Hence, in the present study, kinetics of formation of a ternary compound using isoconversional method [9] is also carried out.

Organization of the thesis

The thesis is divided into eight chapters and the details of these are described as follows.

Chapter 1: Introduction

Chapter 1 describes the significance of “three-stage nuclear programme” adopted by India for effective utilization of limited uranium reserves and abundant thorium reserves. The advantages of FBRs viz., effective utilization of uranium, breeding potential, high burn-up etc. have been highlighted. A brief description about significance of using oxide form of fuel is given. (U, Pu) mixed oxide is used as the fuel in conventional fast reactors worldwide. The importance of oxygen potential measurement for oxide fuels has been explained. The technique used for oxygen potential measurement in the present study i.e. gas equilibration-EMF technique is described. Phase separation in U-Pu-O system containing high plutonia content is briefly outlined. The role of volatile fission products (Cs, Te, I) in FCCI has been explained. The importance of measurement of thermodynamic properties of the compounds which might be formed due to this interaction has been outlined. Principles of the techniques used (transpiration, solid state EMF and calorimetry) for these measurements have been explained. The need for understanding kinetic aspects of formation of these compounds has been brought out. The isoconversional method used for this study has been explained in this section.

Chapter 2: Experimental

This chapter describes the experimental techniques and methods used in the preparation, characterization and measurement of thermochemical data of the compounds. Experimental procedures adopted in equilibration studies, vapour pressure studies, EMF studies, calorimetric techniques etc. are described. Instrumentation details and principles of X-ray diffraction (XRD), thermogravimetry and differential thermal analysis (TG/DTA), drop calorimeter, scanning electron microscopy (SEM), neutron activation analysis (NAA), γ spectrometry, X-ray fluorescence (XRF) etc. are also given in this chapter.

Chapter 3: Measurement of oxygen potential of $(U_{0.54}Pu_{0.46})O_{2-x}$

This chapter deals with the experiments carried out for oxygen potential measurements in unirradiated MOX using gas equilibration coupled with EMF technique at different temperatures and O/M ratio. In the present experiment, measurements are made in the temperature range 1073 – 1473 K and O/M range 1.98 to 2.00. Sample was characterized through chemical analysis and XRD. Uranium in the sample (MOX) was determined using modified Davis & Gray method and plutonium by Drummand and Grant method. A specially designed aluminum holder, which also served as internal standard for shift in peak position value due to possible height disposition was used as the sample holder for carrying out XRD studies.

$Ar-H_2$ gas mixture saturated with H_2O vapour was used as the carrier gas (equilibration gas mixture) for fixing the oxygen potential in the gas phase. This mixture was passed over the sample (MOX pellets) kept at a pre-determined temperature. Depending upon the difference in oxygen potential of MOX and equilibration gas mixture, sample will gain or loose weight. At equilibrium oxygen potential of the gas phase will be equal to oxygen potential of the solid phase (MOX). Oxygen potential of gas phase was monitored continuously using an electrochemical oxygen sensor. This sensor uses In, In_2O_3 as the reference electrode. Complete equilibration was ensured by the constancy in the value of EMF measured between reference electrode and sample electrode (equilibration gas mixture) of the electrochemical oxygen sensor. Once equilibration is established the sample was cooled rapidly to 873 K. Subsequently the equilibration gas mixture was replaced by ultra-high pure helium gas in order to minimize any possible change in O/M of the sample during cooling. The sample at room temperature was weighed and O/M was calculated. The total error in the values of oxygen potential measured in this study was ±2 kJ mol^{-1} and ±0.001 in O/M. Oxygen potential of $(U_{0.54}$

$Pu_{0.46})O_{2-x}$ obtained in this study was also calculated using Thermo-Calc software and compared in the present study. From the temperature dependence of oxygen potential at fixed O/M, partial molar quantities (enthalpy and entropy) were calculated and compared with values reported in literature.

Chapter 4: Thermodynamic stability of Cr_2TeO_6, Fe_2TeO_6, Ni_3TeO_6 by transpiration technique

This chapter deals with the thermodynamic stability of Cr_2TeO_6, Fe_2TeO_6 and Ni_3TeO_6 determined in the temperature range 1183 - 1293 K, 1103 – 1203 K and 1143 – 1272 K respectively by employing transpiration technique. All the ternary compounds were prepared by solid state reaction in air between their respective binary oxides. A vertical thermal analyzer was used to measure the vapour pressure of the samples. This thermal analyzer was validated for vapour pressure measurements using transpiration technique by measuring the vapour pressure of well-studied standard $CdCl_2$. Enthalpy of sublimation of $CdCl_2$ was obtained using ‘third-law analysis’ and compared with data available in the literature. After validation of the system for vapour pressure measurements, thermodynamic stability of the ternary oxides (Cr_2TeO_6, Fe_2TeO_6 and Ni_3TeO_6) was obtained by measuring the vapour pressure of volatile TeO_2 using oxygen as carrier gas. The decomposition reaction of these compounds was confirmed by XRD of intermediate (reaction stopped in between) and final (completion of reaction) mixture. Apparent vapour pressure of TeO_2 was plotted against flow rate (Chair curve), in order to determine the flow rate in which the carrier gas gets saturated with volatile species. The flow rate region in which carrier gas gets saturated with TeO_2 vapour is called as plateau region. The equilibrium vapour pressure of $TeO_2(g)$ at each experimental temperature was measured by taking the flow rate of carrier gas governed by plateau region of chair curve. Using temperature dependence of vapour pressure data of TeO_2 and Gibbs energy of formation data of respective binary oxides (taken from thermochemical tables), Gibbs energy of formation of the above mentioned ternary oxides were calculated. ‘Third-law anlaysis’ of vapour pressure data was carried out and enthalpy of formation of these ternary oxides at 298 K at each temperature was derived. The random scatter in the value of enthalpy of formation of these oxides at 298 K calculated from each experimental temperature around the mean value confirmed absence of temperature dependent errors in our measurement.

Chapter 5: Thermochemical studies on Cr-Te-O system using EMF technique

There are three stable ternary oxides in the system Cr-Te-O viz., Cr_2TeO_6, $Cr_2Te_3O_9$ and $Cr_2Te_4O_{11}$. In the present study the thermodynamic stabilities of Cr_2TeO_6, $Cr_2Te_3O_9$ and $Cr_2Te_4O_{11}$ in the temperature range 684 - 877 K, 725 - 824 K and 704 - 878 K respectively were obtained using solid state EMF technique. Oxygen potential over various phase fields was determined using a two compartment cell assembly. The experimental EMF assembly consists of calcia stabilized zirconia (15CSZ) tube as the solid electrolyte and air, Pt as reference electrode. This experimental assembly was validated for EMF measurements by measuring the EMF between air ($P_{O2} = 0.21$ atm), Pt and pure O_2 (1 atm), Pt electrodes. The observed EMF values were compared with the theoretical EMF values. It was found to be very close to the theoretical experession $E = 0.0337\ T$. In addition, the system was validated by comparing $\Delta_f G^o$ values of NiO(s) and $Cu_2O(s)$ obtained by measuring the EMF values between test electrode (Ni, NiO and Cu, Cu_2O) and the reference electrode (O_2 (1 atm)) with the values reported in the literature. After validation, EMF of following cells was measured

(i) (-) Pt, $Cr_2O_3(s)$, Te(s), $Cr_2TeO_6(s)$ │ CSZ │ air ($P_{O2} = 0.21$ atm), Pt (+)

(ii) (-) Pt, $Cr_2O_3(s)$, Te(l), $Cr_2TeO_6(s)$ │ CSZ │ air ($P_{O2} = 0.21$ atm), Pt (+)

(iii)(-) Pt, $Cr_2Te_3O_9(s)$, Te(s), $Cr_2TeO_6(s)$ │ CSZ │ air ($P_{O2} = 0.21$ atm), Pt (+)

(iv)(-) Pt, $Cr_2Te_4O_{11}$(s), TeO_2(s), Cr_2TeO_6(s) │ CSZ │ air (P_{O2} = 0.21 atm), Pt (+)

(v) (-) Pt, $Cr_2Te_4O_{11}$(s), Te(s), $Cr_2Te_3O_9$(s) │ CSZ │ air (P_{O2} = 0.21 atm), Pt (+)

(vi)(-) Pt, $Cr_2Te_4O_{11}$(s), Cr_2TeO_6(s), $Cr_2Te_3O_9$(s) │ CSZ │ air (P_{O2} = 0.21 atm), Pt (+)

EMF values obtained from these cells were corrected with respect to pure O_2 (1 atm). The co-existence of these phases was confirmed by phase equilibration studies. Using cells (i) and (ii) $\Delta_f G^o$ of Cr_2TeO_6(s) was obtained. In addition, using cells (i) and (ii) enthalpy of transition and transition temperature of Te(s) → Te(l) were calculated and compared with values reported in the literature. Using cell (iii) $\Delta_f G^o$ of $Cr_2Te_3O_9$(s) was obtained and from cell (iv) $\Delta_f G^o$ of $Cr_2Te_4O_{11}$(s) was obtained. $\Delta_f G^o$ of $Cr_2Te_4O_{11}$(s) was also obtained using cells (v) and (vi) and the values were compared with those of obtained using cell (iv). There is a good agreement among $\Delta_f G^o$ values of $Cr_2Te_4O_{11}$(s) obtained using cells (iv), (v) and (vi). Values of $\Delta_f G^o$ of Cr_2TeO_6(s) obtained using EMF technique and transpiration technique (Chapter 4) is compared. The comparison shows a good agreement between the values of $\Delta_f G^o$ of Cr_2TeO_6(s) obtained by two different techniques.

Chapter 6: Thermochemical studies on Cr_2TeO_6, Fe_2TeO_6, Ni_3TeO_6, $Ni_2Te_3O_8$ and $NiTe_2O_5$ using calorimetric technique

In this chapter calorimetric study on Cr_2TeO_6, Fe_2TeO_6, Ni_3TeO_6, $Ni_2Te_3O_8$, $NiTe_2O_5$ is presented. In this study enthalpy increments of the above compounds have been measured using isoperibol type high temperature calorimeter. The reference sample (α-alumina (SRM 720)) and the sample pellets were dropped alternatively from sample holder which was kept at ambient temperature into the sample crucible at experimental temperature. When the sample is dropped, the sample attains the temperature of the crucible and hence there is a small difference (ΔT) between the temperatures of sample and reference crucible. This temperature difference (ΔT), causes a heat flow, (Q) which is recorded as a function of time as the EMF output from the calorimetric detector. From the peak areas, enthalpy increments of samples were determined using critically assessed enthalpy increment values of the alumina. The expressions of enthalpy increment of these compounds are fitted in a polynomial of type AT + BT^2 + C/T +D using constraints (a) $H_T^o - H_{298K}^o = 0$ at T = 298 K (b) the derivative of this function at 298 K is equal to the value of the heat capacity of the respective compound. From the measured enthalpy increments other thermodynamic properties viz., heat capacity, entropy and free energy function (FEF) have been derived. Using FEF values enthalpy of formation of these compounds at 298 K has been calculated using ‘third-law’.

Chapter 7: Kinetics of formation of La_2TeO_6

In this chapter studies on the kinetics of formation of lanthanum tellurate (La_2TeO_6) is reported. The kinetics of formation of La_2TeO_6 in the temperature range 1023 – 1203 K was studied by means of thermogravimetric (TG) technique. La_2TeO_6 was formed by heating a stoichiometric mixture of $La(OH)_3$ and TeO_2 in a stream of pure oxygen. The kinetics of formation was studied by carrying out the TG experiments under isothermal as well as non-isothermal conditions. Model-free isoconversional method (Kissiner-Akahira-Sunose (KAS)) was employed to derive the kinetic parameters and to establish the dependence of effective activation energy on progress of the formation reaction. The amount of Te in the reaction product was measured by EDXRF and NAA techniques to exclude the possibility of significant loss of TeO_2 during the reaction. A typical SEM micrograph of the product obtained after heating the reaction mixture indicated the product to be highly porous.

The plot of E_α vs extent of reaction (α) was divided into three regions. This plot revealed the complex nature of the reaction which indicated typical behaviour of a competitive reaction. The mechanism of formation of La_2TeO_6 was ascertained using model based method.

Chapter 8: Summary and Conclusions

The conclusions drawn from the present investigations are summarized in Chapter 8. (1) The chemical potential of oxygen in (U, Pu) mixed oxide containing 46 mol.% plutonium oxide has been measured for the first time. These experiments indicated that increase in oxygen potential increases O/M ratio of this mixed oxide. However, MOX with Pu content 46% could not be reduced below an O/M of 1.985 in the present study even after prolonged equilibration (240 h) in an atmosphere having oxygen potential -550 kJ mol^{-1}. The resistance to reduction in O/M observed in the present study is probably due to segregation of one of the fcc phases (with an O/M close to 2.000) which inhibits further reduction. (2) The standard Gibbs energy of formation of $Cr_2TeO_6(s)$, $Fe_2TeO_6(s)$ and $Ni_3TeO_6(s)$ was determined by employing thermogravimetry (TG) based transpiration technique. Enthalpy of formation of these compounds at 298 K has been determined using ‘third-law analysis’. (3) The phase fields in Cr-Te-O system have been established by equilibration studies and standard Gibbs energy of formation of $Cr_2TeO_6(s)$, $Cr_2Te_3O_9(s)$ and $Cr_2Te_4O_{11}(s)$ have been measured using EMF technique. Δ_fG^o of $Cr_2Te_3O_9(s)$ and $Cr_2Te_4O_{11}(s)$ are reported for the first time in this study. (4) The enthalpy increments of $Cr_2TeO_6(s)$, $Fe_2TeO_6(s)$, $Ni_3TeO_6(s)$, $Ni_2Te_3O_8(s)$ and $NiTe_2O_5(s)$ had been measured for the first time. From enthalpy increment values other thermodynamic properties were derived. (5) Kinetics of formation of La_2TeO_6 has been carried out for the first time in the present study. The effective activation energy for the formation of La_2TeO_6 varied from 335 to 790 kJ mol^{-1} during the progress of this reaction. The mechanism of formation of La_2TeO_6 has been ascertained using model based method.

References

1. Grover R, Chandra S. Scenario for growth of electricity in India. Energy Policy 2006; 34: 2834-2847
2. International Atomic Energy Agency, IAEA report on Climate change and nuclear power, Vienna, 2015
3. Chidambaram R, Ganguly C. Plutonium and thorium in the Indian nuclear programme. Current Science. 1996; 70: 21-35
4. Vasudeva Rao P R, Anthonysamy S, Krishnaiah M V, Chandramouli V. Oxygen potential and thermal conductivity of (U, Pu) mixed oxides. J Nucl Mater. 2006; 348: 329-334
5. Kato M. Oxygen Potentials and Defect Chemistry in Nonstoichiometric $(U,Pu)O_2$, Stoichiometry and Materials Science - When Numbers Matter, Dr. Alessio Innocenti (Ed.), ISBN: 978-953-51-0512-1, 2012, InTech.
6. Suresh Kumar K V, Babu A, Anandapadmanaban B, Srinivasan G. Twenty five years of operating experience with the Fast Breeder Test Reactor. Energy Procedia. 2011; 7: 323–332.
7. Khanna A S. Fuel-cladding chemical interaction on mixed oxide liquid metal fast breeder reactors – A review. Reactor Research Centre. 1982; RRC-53.
8. Chattopadhyay G, Juneja J M. A thermodynamic database for tellurium bearing systems relevant to nuclear technology. J Nucl Mater. 1993; 202: 10-28.
9. Vyazovkin S, Burnham A K, Criado J M, Maqueda L A P, Popescu C, Sbirrazzuoli N. ICTAC Kinetics Committee recommendations for performing kinetic computations on thermal analysis data. Thermochim Acta. 2011; 52: 1-19.

LIST OF FIGURES

LIST OF TABLES

ABBREVIATIONS

ABBREVIATION	**FULL NAME**
AHWR	Advanced heavy water reactor
BWR	Boiling water reactor
CSZ	Calcia stabilized zirconia
DTA	Differential thermal analysis
DSC	Differential scanning calorimetry
EDXRF	Energy dispersive x-ray fluorescence
EMF	Electromotive force
FBR	Fast breeder reactor
FBTR	Fast breeder test reactor
FCCI	Fuel clad chemical interaction
IGC	Intragranular corrosion
JCPDF	Joint committee on powder diffraction standards
KEML	Knudsen effusion mass loss
KEMS	Knudsen effusion mass spectrometry
LWR	Light water reactor
LEDB	Lower electrolytic domain boundary
NAA	Neutron activation analysis
PFBR	Prototype fast breeder reactor
PHWR	Pressurised heavy water reactor
SEM	Secondary electron microscopy
SS	Stainless steel
TGA	Thermogravimetric analysis
UEDB	Upper electrolytic domain boundary
XRD	X-ray diffraction

Chapter 1

INTRODUCTION

1

1.1 Nuclear Power Programme in India

In the developing country like India, nuclear energy plays an important role in meeting energy demand. Currently electric power generation is mainly due to non-renewable sources like burning of fossil fuels which constitute 87.55% of the total installed capacity [1]. Renewable power plants e.g. hydro, solar, wind, nuclear constitute remaining 12.45%. The global warming/greenhouse effect which is mainly due to burning of fossil fuels can be minimized using these renewable energy sources. Nuclear energy is considered to be clean energy because operation of nuclear reactor involves negligible greenhouse gases [2]. Also the energy density of nuclear fuels is million times higher than fossil fuels which reduces fuel requirement for nuclear reactor tremendously [3-5]. For example, to operate 1000 MWe power plant coal requirement is 2,60,000 tonnes per annum whereas uranium (natural) annual requirement for thermal reactors is 200 tonnes and for fast reactors it is only 1.3 tonnes of uranium (fissile equivalent). Presently nuclear energy contribution in India is only about 3% to the total electricity generation and it has been planned to increase it to 25% by the year 2050. At present there are twenty one nuclear reactors operational in India which produce 5780 MWe energy.

India has limited uranium (~52,000 tons) and vast thorium (~3,19,000 tons) resources. India envisages three stage nuclear power programme using its naturally occurring uranium and vast thorium resources [6,7]. In the first stage, power is derived from the uranium resources using thermal reactors e.g. boiling water reactor (BWR), light water reactor (LWR), pressurized heavy water reactor (PHWR). In thermal reactors, fission is caused by thermalized (slow) neutrons (0.025eV) [8]. PHWRs employ natural uranium oxide as fuel whereas BWRs and LWRs employ enriched uranium oxide as fuel.

Natural uranium available in the earth crust contains 0.7 at.% ^{235}U (fissile isotope[#]) and 99.3 at.% ^{238}U (fertile isotope*) [9]. In stage 1, apart from generation of power from thermal reactors, through neutron capture by fertile isotope ^{238}U, another fissile isotope ^{239}Pu is produced as by-product.

$$^{238}\mathrm{U} + {}^{1}\mathrm{n} \rightarrow {}^{239}\mathrm{U} \rightarrow \beta^{-} + {}^{239}\mathrm{Np} \rightarrow \beta^{-} + {}^{239}\mathrm{Pu}$$

The uranium utilization in stage 1 is only 0.4%. Uranium can be effectively utilised (~ 60-70%) in stage 2 i.e. in a fast reactor / fast breeder reactor (FBR) [10,11]. In a fast reactor, the fissile isotope i.e. ^{239}Pu undergoes fission by absorption of fast i.e. high energy neutron (energy 1-2 MeV). Fast reactors are fuelled with U and Pu mixed oxide/carbide/nitride or metallic alloys and use thorium as the blanket material. The main aim of this stage is to multiply i.e. breed plutonium and utilise the energy potential of uranium to the maximum. In this stage fertile isotope ^{232}Th is converted to fissile isotope ^{233}U by the following neutron capture reaction.

$$^{232}\mathrm{Th} + {}^{1}\mathrm{n} \rightarrow {}^{233}\mathrm{Th} \rightarrow \beta^{-} + {}^{233}\mathrm{Pa} \rightarrow \beta^{-} + {}^{233}\mathrm{U}$$

^{233}U produced in stage 2 will be used as fuel for stage 3 reactors. ^{232}Th will be used as blanket and hence these reactors can produce electricity as well as breed ^{233}U from ^{232}Th. The main advantage of using ^{233}U is that it has breeding potential even in thermal region [12-15]. India has vast resources of thorium; hence through this indigenous approach of coupling limited uranium reserves with vast thorium reserves our long term energy needs can be fulfilled.

[#] Heavy nuclides such as U^{235}, Pu^{239}, U^{233} undergo nuclear fission by capturing thermalized neutrons (energy 0.025eV). These nuclides are called fissile nuclides or fissile isotopes.

[*] Heavy nuclides such as U^{238}, Th^{232} can be converted to fissile nuclides (Pu^{239}, U^{233} respectively) by neutron capture and subsequent beta decays. These nuclides are referred as fertile nuclides or fertile isotopes.

1.2 FBR Programme in India

At present India is in its stage 2 of nuclear power programme. Fast reactor programme was initiated in 1975 in India and Fast Breeder Test Reactor (FBTR) was commissioned in 1985 which uses uranium and plutonium mixed carbide as the fuel [16]. The experience gained from the construction, commissioning and operation of FBTR as well as worldwide FBR operational experience has provided the necessary confidence to launch a Prototype FBR (PFBR) of 500 MWe capacity [17]. There is proposal to construct more FBRs in future with uranium and plutonium mixed oxide or uranium plutonium metallic alloy as fuel. The FBRs have the following major advantages [18-20]

1. FBRs have the breeding potential i.e. they produce more fissile material than they consume over a period of time. FBRs are also crucial for converting ^{232}Th to ^{233}U for the third stage Indian nuclear programme.
2. In thermal reactors maximum burn up achievable is 1-3 at.% whereas in FBRs burn up can reach up to 10-20 at.% which minimises the fuel fabrication and reprocessing costs.
3. Uranium utilisation can be increased with the conversion of uranium to plutonium.
4. Fast reactors can be used as plutonium and minor actinide burners; they can also be employed for transmuting other long lived radionuclides which reduces radio toxicity burden.

1.3 Nuclear Fuels

The forms of fuel employed in nuclear reactors can be oxide, carbide, nitride, metal/alloy etc. It is in the form of pellets for oxide, carbide, nitride and in the form of rod for metallic fuel. The fuel employed in nuclear reactors is encapsulated in a thin cladding tube. The fuel should have the following properties for successful operation of a reactor [21, 22].

1. The fuel should have excellent chemical compatibility with both cladding material and coolant.
2. The fuel should have high melting point and there should be no phase transformations in the operating temperature range because it will lead to dimensional, density or other physical changes which are undesirable.
3. It should have high thermal conductivity so that high power density and high specific power can be attained without much temperature drop in the fuel pin.
4. It should have high fissile atom density and hence higher breeding potential.
5. Fabrication and reprocessing of fuel should be easy.
6. The fuel should retain its physical and mechanical stability during its life time in the reactor.
7. It should be radiation resistant.

No single compound satisfies all the above requirements. Metallic fuel has the advantages of high thermal conductivity, high fissile atom density, high breeding ratio but low melting point, phase transformations in the operating temperature range of reactor, highly chemical reactivity with air and water, hence difficult to fabricate and reprocess, limit their applicability in nuclear reactor. In ceramics, carbides and nitrides have the advantages of high breeding ratio, high thermal conductivity, high melting point but difficult to fabricate and reprocess. Oxides have high melting point, reasonably good compatibility with cladding material and coolant, considerable resistance to radiation damage. They are easy to fabricate and reprocess. There is well proven worldwide operational experience on oxides. The disadvantage of oxide fuel is low thermal conductivity and breeding ratio. Due to numerous advantages of oxide as fuel material UO_2 is employed as the fuel in thermal reactors. The mixed oxides of uranium and plutonium are being used as fuels for fast reactors. The mixed oxides of uranium and thorium are being developed as fuels for thermal breeder reactors.

The use of any material as fuel in a nuclear reactor calls for very accurate measurement of its physicochemical properties viz., heat capacity, thermal conductivity, thermal expansion, free energy, entropy, enthalpy, vaporisation behaviour and their variation with temperature [23]. Among these, oxygen potential, which is a measure of the driving force for numerous reactions that take place inside a fuel pin during irradiation, is a very important thermochemical property for oxide fuels. Oxygen potential controls vapour pressure inside the fuel pin and redistribution of oxygen and actinides. Thermal conductivity of the fuel is a strong function of oxygen to metal ratio (O/M) which depends upon the oxygen potential. It controls the chemical state of fission products, their interaction with the fuel and the clad material (FCCI). In case of any breach interaction between fuel and coolant is also controlled by oxygen potential. FCCI i.e. chemical compatibility between fuel and cladding material is one of the important factors which decide the life time of the fuel pin during irradiation. The thermochemical property which decides the extent of FCCI is oxygen potential [24, 25]. Uranium plutonium mixed oxide containing up to 30 mol.% plutonia is considered as the conventional fuel for fast reactors. Many measurements of oxygen potential as a function of temperature and composition have been carried out by variety of methods [26-34]. Oxygen potential data of uranium plutonium mixed oxide containing up to 30 mol.% are available in the literature. In the FBTR, India eight fuel subassemblies containing $(U,Pu)O_2$ having Pu/(U+Pu) = 0.45 are being irradiated. The irradiation testing of this high-plutonia content fuel in FBTR needs an understanding of the physicochemical properties of the fuel. Hence, in the present study, oxygen potential of $(U_{0.54}\,Pu_{0.46})O_{2-x}$ has been measured.

Before irradiation the virgin fuel is a solid solution of urania and plutonia with well-defined chemical composition. With increase in burn up, oxygen potential increases as lower valent elements are produced to more extent as compared to elements of tetra or higher valences. Fission products can be classified into four categories depending upon their chemical states (1) fission gases and other volatile fission products (2) fission products forming metallic precipitates (3) fission products forming oxide precipitates (4) fission products dissolved as oxides in the fuel matrix [35]. Among these fission products, reactivity of various volatile fission products is of particular importance in the prediction of high-temperature fuel rod behaviour. A complete understanding (thermodynamically as well as kinetically) of FCCI under reactor operation conditions is therefore, necessary. There are economic incentives involved in selecting thickness of clad tube (lesser thickness leads to more efficient heat transfer) [36]. But clad thickness has to be optimum taking into consideration FCCI. Among the volatile fission products, Tellurium (Te) is highly reactive and hence its interaction needs to be studied for complete understanding of clad corrosion. Because of its volatile nature it is found in fuel clad gap. Depending upon oxygen potential and tellurium potential prevailing inside the fuel pin, formation of various compounds in M-Te-O (M is constituent of clad i.e., SS316) can take place which leads to intragranular corrosion (IGC) of clad [35-40]. IGC leads to embrittlement of clad. Hence, thermochemical data of the compounds formed in the systems M-Te-O (M = Fe, Cr, Ni) are essential. The thermodynamic properties such as enthalpy and heat capacity are required for reactor safety calculations. For the performance analysis of fuel-clad assembly (fuel pin) under normal and off normal conditions of operation a set of thermophysical and thermochemical properties of complete fuel matrix is fed into various computer programmes [41]. These computer programs use these data to determine the phases which coexist under a given set of experimental conditions (at various temperatures and pressures). Hence, in the present study, thermochemical stability of some of the ternary tellurates and tellurites has been determined.

Since thermodynamic data are applicable to equilibrium conditions, conditions inside the fuel pin viz., varying temperature, continuous generation of fission products etc. represent non-equilibrium state. Under these conditions, along with thermodynamic stability, kinetics of formation of these compounds plays a vital role. Hence, in the present study, kinetics of formation of a typical ternary compound is also carried out.

1.4 Objective of the thesis

(1) Determination of the oxygen potential of $(U_{0.54}Pu_{0.46})O_{2-x}$ using gas equilibration coupled with EMF technique

(2) Measurement of thermochemical data of ternary compounds in M-Te-O (M=Fe, Cr, Ni) system employing various experimental methods

(3) Study of kinetics of formation of a typical ternary compound using model-free isoconversional method

In the first part of the ‘Introduction’ of this thesis, the theoretical aspects related to the measurement of oxygen potential are presented. In the second part of this chapter, the theoretical aspects related to techniques used for the measurement of thermophysical and thermochemical properties used in the present study are presented. In the third part, theoretical aspects related to the use of thermogravimetry as a tool for performing kinetic analysis are outlined.

Part I

1.5 Oxygen Potential

Oxygen potential is defined as the partial molar free energy of oxygen in the oxide. Relative oxygen potential is defined as difference between the oxygen potential of a given substance and the oxygen potential in its standard state. Superscript ^{o} represents standard state.

$$\Delta\mu_{O_2} = \mu_{O_2} - \mu_{o_2}^{o} = R\,T \ln a_{o_2} \qquad (1.1)$$

where a_{o_2} is the thermodynamic activity of oxygen. Activity of a species *i* is defined as

$$a_i = \frac{p_i}{p_i^o} \qquad (1.2)$$

where p_i is the partial pressure of species i in the given substance and p_i^o is the partial pressure of i in its standard state. Standard state of oxygen is pure oxygen gas at 1 bar pressure. Since p_i^o = 1, eqn. (1.1) can be rewritten as

$$\Delta\mu_{O_2} = \mu_{O_2} - \mu_{o_2}^{o} = R\,T \ln a_{o_2} = R\,T \ln p_{o_2} \qquad (1.3)$$

1.6 Techniques for the measurement of thermodynamic activity

There are various experimental methods for determining thermodynamic activity. The vapour pressure methods include static, dynamic, effusion and equilibration methods. Galvanic cell technique is also used for the measurement of thermodynamic activity. In the present study gas equilibration – EMF technique has been employed for the measurement of oxygen potential.

1.6.1 Oxygen potential measurement by gas equilibration technique

In this technique thermodynamic activity of oxygen is measured by establishing equilibrium between a gas phase and a solid phase. Oxygen potential of the gas phase which is in thermodynamic equilibrium with the solid phase is subsequently measured. Since the solid and the gas phase are in equilibrium, the oxygen activity in the gas phase is equal to the oxygen activity in the solid phase. In gas equilibration method there are two modes of operation. In the first mode of operation, a small volume of gas phase is brought into equilibrium with the condensed phase. The composition of gas is analysed after attaining equilibrium. In the second mode of operation, gas mixture of fixed composition is passed over the condensed phase. The gas mixtures which are generally used for oxygen potential measurements are (a) H_2-H_2O (b) CO-CO_2 (c) H_2-CO_2.

In the present study H_2-H_2O gas mixture has been used for fixing the oxygen potential. A gas mixture of fixed composition is passed over the oxide substance whose oxygen potential needs to be determined. The equilibrium partial pressure of oxygen in the gas phase is determined by the galvanic cell technique. The change in composition of the condensed phase is monitored by thermogravimetric technique.

In these gas mixtures viz. H_2-H_2O, CO-CO_2 and H_2-CO_2 equilibrium oxygen partial pressure at elevated temperatures is many orders of magnitude lower than the partial pressure of the constituent gases in the gas mixture (H_2, H_2O, CO, CO_2). Hence equilibrium ratios pH_2/pH_2O and pCO_2/pCO are practically same as their initial ratios $(pH_2/pH_2O)_i$ and $(pCO_2/pCO)_i$.

The relation between equilibrium oxygen partial pressure and partial pressure of constituents in gas mixtures CO-CO_2, H_2-H_2O and H_2-CO_2 can be obtained as explained below:

1.6.1.1 Oxygen potential of CO-CO_2 gas mixture

The following equilibrium reaction establishes the oxygen potential in CO-CO_2 gas mixture

$$CO(g) + \frac{1}{2} O_2(g) = CO_2(g) \qquad (1.4)$$

The equilibrium oxygen potential of this gas mixture can be expressed as:

$$R\,T \ln p_{o_2} = 2 \times \left(\Delta_f G^o_{CO_2} - \Delta_f G^o_{CO} + R\,T \ln \frac{p_{CO_2}}{p_{CO}} \right) \qquad (1.5)$$

Hence, by varying partial pressures of CO and/or CO_2, oxygen potential of CO-CO_2 gas mixture can be varied. Standard Gibb’s energy of formation of CO_2(g), CO(g) can be obtained from reference [42].

CO gas can be generated in-situ by passing CO_2 gas over a redox couple maintained at a fixed temperature. By varying temperature of redox couple partial pressures of CO and CO_2 can be varied in the gas mixture and hence oxygen potential.

1.6.1.2 Oxygen potential of H_2-H_2O gas mixture

In H_2-H_2O gas mixture the following equilibrium reaction establishes the oxygen potential

$$2H_2(g) + O_2(g) = 2H_2O(g) \qquad (1.6)$$

The equilibrium oxygen potential of this gas mixture can be expressed as:

$$R\,T \ln p_{o_2} = 2 \times \left(\Delta_f G^o_{H_2O} + R\,T \ln \frac{p_{H_2O}}{p_{H_2}} \right) \qquad (1.7)$$

Hence, by varying the partial pressures of H_2 and/or H_2O, oxygen potential of H_2-H_2O gas mixture can be varied. Standard Gibb's energy of formation of H_2O (g) can be taken from reference [42].

1.6.1.3 Oxygen potential of H_2-CO gas mixture

The 'water-gas' equilibrium can be represented as:

$$H_2(g) + CO_2(g) = H_2O(g) + CO(g) \tag{1.8}$$

Equilibrium constant K for this reaction (1.8) can be expressed as

$$K = (pCO \times pH_2O) / (pH_2 \times pCO_2) \tag{1.9}$$

Since $pCO = pH_2O$

$$K = (pCO \times pCO) / (pH_2 \times pCO_2) \tag{1.10}$$

$$pH_2 = (1/K) \times (1/ pCO_2) \times (pCO \times pCO) \tag{1.11}$$

Since $(pCO_2)_i = pCO_2 + pCO$ and $(pH_2)_i = pH_2O + pH_2$

where $(pCO_2)_i$ and $(pH_2)_i$ are partial pressure of $CO_2(g)$ and $H_2(g)$ in initial mixture

$$(pCO_2)_i / (pH_2)_i = (pCO_2 + pCO) / (pCO + (1/K) \times (1/ pCO_2) \times (pCO \times pCO)) \tag{1.12}$$

Upon simplification equation (1.12)

$$(pCO_2)_i / (pH_2)_i = K \times pCO_2 \times (pCO_2 + pCO) / (pCO \times (K \times pCO_2 + pCO)) \tag{1.13}$$

Dividing each term at right hand side of equation (1.13) by K× pCO

$$(pCO_2)_i / (pH_2)_i = (pCO_2/ pCO) \times [(1+ (pCO_2 / pCO)) \times ((pCO_2 / pCO)) + (1/K))] \tag{1.14}$$

The standard Gibbs energies of formation of compounds CO_2 (g), CO (g) and H_2O (g) are obtained from Ref. [42] and using these values K can be computed. In order to compute required oxygen potential at a given temperature, corresponding ratio of pCO_2 / pCO can be calculated from equation (1.5). Since K and the partial pressure ratio pCO_2 / pCO, for the required oxygen potential are known, the ratio $(pCO_2)_i$ / $(pH_2)_i$ which has to be taken initially can be computed using equation (1.14).

Part II

1.7 Vapour Pressure Measurement

There are several techniques of measuring the vapour pressure of substances. These techniques can be divided into four groups – static, dynamic, effusion and equilibration methods [43-46]. In the static method the substance whose vapour pressure has to be determined is heated in an evacuated chamber until equilibrium is reached between the condensed and the gas phase. Once equilibrium is established, actual measurement of vapour pressure can carried out (i) using different gauges e.g. spiral, sickle and membrane (Bourdon) gauges and (ii) using atomic absorption spectrophotometry. Boiling point method and transpiration method come in the category of dynamic methods. In the boiling point method external pressure is fixed using a manostat and temperature is increased till boiling is observed. At the boiling point, saturated vapour pressure of substance becomes equal to external pressure. In the transpiration method, a carrier gas which is passed over the sample heated at the desired temperature, sweeps away the sample vapours along with it. Under the conditions where the carrier gas gets saturated with the sample vapours, vapour pressure can be calculated. The entire group of methods where vapour pressure is calculated using rate of evaporation come under the category of effusion methods. Langmuir, Knudsen effusion mass loss (KEML) and Knudsen effusion mass spectroscopy (KEMS) constitute effusion methods. In these methods experiments are carried out under high dynamic vacuum in molecular flow region and the material that is transported away from the sample is measured. Isopiestic method (Isothermal as well as non-isothermal) and equilibration with gas mixture (H_2/CH_4 to measure carbon activity, H_2/H_2O to measure oxygen activity, H_2/H_2S to measure sulphur activity etc.) constitute equilibration methods. Out of these techniques, transpiration technique has been employed in the present work for vapour pressure measurements.

1.7.1 Transpiration Technique

In conventional transpiration technique, the carrier gas which can be inert or reactive is passed over the sample kept at a constant temperature in uniform heating zone of the furnace. This vapour-laden gas is passed through condenser kept downstream from the sample and hence, sample vapours get condensed in the collector. Vapour pressure of the sample is determined from weight-loss of the sample or weight-gain of the condenser. The condensate in the collector can also be subjected to chemical or radiochemical analysis to determine the number of moles of the vapour which is required for deriving the vapour pressure. The essential features of the transpiration apparatus are shown in Fig. 1.1. The carrier gas introduced at A, flows past the sample in an isothermal region B and the constrictions at C and D minimize diffusion and heat loss. The vapours get condensed in the collector E and the carrier gas exits at outlet G [45].

Transpiration method is one of the oldest and versatile ways of vapour pressure measurement which is used to study heterogeneous equilibria involving gases (solid-gas and liquid-gas equilibria). Some of the valuable reviews regarding application of this technique for vapour pressure measurement can be found in literature [44, 45, 47].

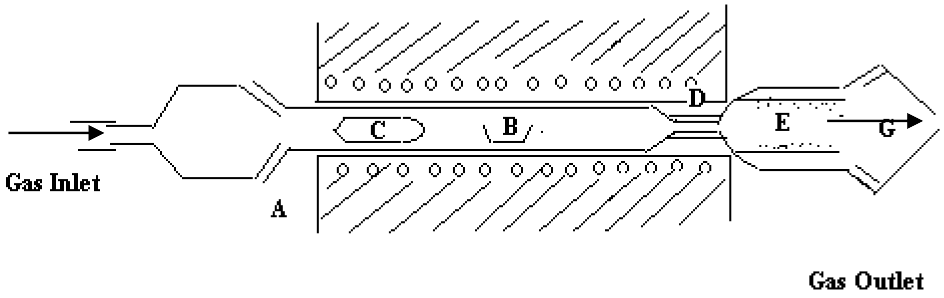

Fig. 1.1 Transpiration Apparatus

The equilibrium vapour pressure in the transpiration experiment is calculated from the number of moles of the vapour carried away and number of moles of carrier gas swept over the sample using the Dalton's law of partial pressures.

$$P_v = [n_v / (n_v + n_c)]\, P \qquad (1.15)$$

where P_v = equilibrium vapour pressure of sample

n_c = number of moles of the carrier gas swept over the sample

n_v = number of moles of the sample vapour transported by n_c moles of carrier gas

P= total pressure in the system

The equation (1.15) is valid under the following conditions-

I. The vapour is transported only by carrier gas. There is practically no contribution due to self – diffusion of vapour under temperature gradient.

II. The equilibrium between vapour and condensed phase is established.

III. The vapour behaves ideally (At high temperature and low pressure conditions, the vapour can be considered ideal).

Since $n_v << n_c$, hence ($n_v + n_c \sim n_c$) the equation (1.15) can be written as

$$P_v = [n_v / n_c].\ P \tag{1.16}$$

$$P_v = (w/M) \times (RT_c/V_c) \tag{1.17}$$

where w is the mass of the vapour, M is the molecular weight, R is universal gas constant, T_c is the temperature at which carrier gas is collected and V_c is the volume of carrier gas which transports w grams of sample vapour.

When the apparent vapour pressure (P_v) is plotted against flow rate of carrier gas curve similar to Fig. 1.2 is obtained.

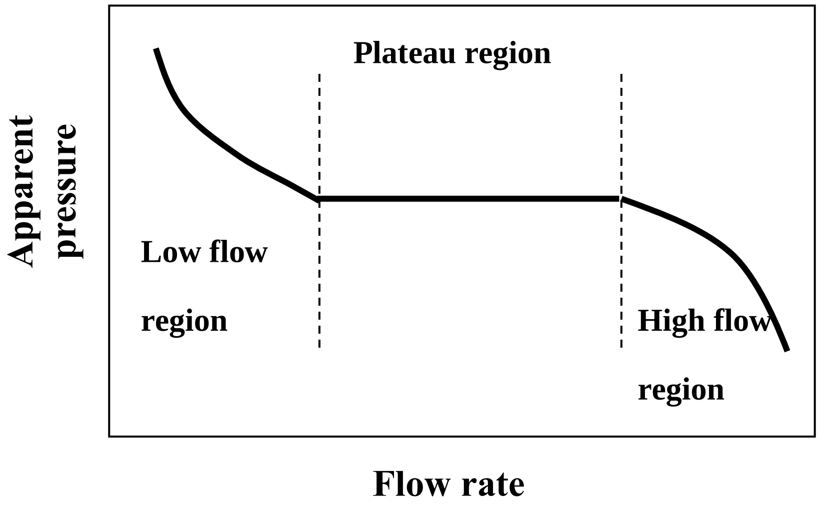

Fig. 1.2 Plot of apparent pressure vs flow rate

If the flow rate is very low (Region I) then vapour transports not only with carrier gas but also due to significant self-diffusion and hence, the fraction $[n_v / (n_v + n_c)]$ becomes large. At high flow rates, due to unsaturation of the carrier gas with the sample vapours the fraction $[n_v / (n_v + n_c)]$ becomes small. In the middle region, which is termed as plateau region, carrier gas gets saturated with sample vapours and hence, vapour pressure is independent of flow rate. In this region apparent vapour pressure becomes equal to equilibrium vapour pressure of the sample. Hence, the carrier gas flow has to be chosen so as to lie in the plateau region for the determination of vapour pressure. The range of flow rate for plateau region depends on the transpiration apparatus and the system under investigation.

The prerequisite for obtaining vapour pressure using transpiration technique is aprior knowledge of vapour phase composition. This can be obtained from mass spectrometric studies. By transpiration method vapour pressures up to 10^{-7} bar can be measured. The sensitivity of this technique can further be increased by employing radiotracers.

1.8 Solid State EMF technique

Galvanic cell measurement is a very attractive technique for thermodynamic study. The reason being (i) in this technique the measured EMF (electromotive force) of the electrochemical cell can be directly expressed in terms of the desired thermodynamic property (activity of a component, ΔG^o of the reaction) of the system. This is a direct technique for the measurement of Gibbs energy of substances. This method has unique potential of yielding accurate and precise data (±0.5 kJ mol^{-1}) at elevated temperatures [48]. The basic physico-chemical principle of this method is also simple.

A galvanic cell is typically represented as eqn. (1.18)

$$\text{Pt, } X_2\,(a_{X2}^{I})\ \big|\ \text{electrolyte } (X^{y-})\ \big|\ X_2\,(a_{X2}^{II}), \text{ Pt} \qquad (1.18)$$

This is a typical example of a concentration cell. Here Pt is platinum electrical lead, a_{X2}^{I} and a_{X2}^{II} are the activities of the neutral form of the conducting species (X^{y-}) at the electrodes (anode and cathode). The solid electrolyte (X^- ion conductor) has ionic transport number (t_{ion}) greater than 0.99 [49-52]. t_{ion} is the ionic transport number i.e. fraction of total current carried by ion.

$$t_{ion} = \frac{\sigma_{ion}}{\sigma_T} \tag{1.19}$$

where σ_{ion} and σ_T are ionic and total electrical conductivity respectively. σ_T is the sum of electrical conductivity due to electrons, holes and ions. In the case of molten and aqueous salt electrolytes, the electronic current carriers can be safely neglected but not in the case of solids. Point defects are always present in solid electrolytes at all temperatures above 0 K. Due to rather high mobility of electronic charge carriers (electrons and holes) compared to ion mobility, solid electrolytes are found only among those materials in which electronic defects are minority defects e.g. oxides and halides and not carbides, nitrides or borides. Aliovalent impurities also introduce excess defects whose concentration is fixed primarily by composition and often independent of temperature [49]. In a solid electrolyte electronic conductivity is undesirable and electrical conduction should be mainly due to ions (i.e. $t_{ion} > 0.99$). As the concentration of point defects (and hence, electronic conductivity) depends on the chemical activity of components, ionic solids can be used as electrolytes over a range of chemical activity of the neutral form of the conducting species and temperature. Thus electrolytic conduction domain (where $t_{ion} > 0.99$) is an important factor limiting the application of solid electrolytes in solid state electrochemical cells. The domain of the solid electrolyte in the σ-T-Px_2 space (Patterson diagram) where the ionic conductivity is at least 100 times higher than electron or hole conductivity is called electrolytic conduction domain and respective boundaries are termed as lower electrolytic domain boundary (LEDB) and upper electrolytic domain boundary (UEDB). Hence, proper electrolyte and reference electrode are selected so that the chemical potentials at electrode/electrolyte interfaces are maintained within the ionic conduction domain of the solid electrolyte.

The half-cell reactions of a galvanic cell (1.18) can be written as

At Cathode: $\frac{1}{2} X_2 + e^- \rightarrow X^-$ (1.20)

At Anode: $X^- \rightarrow \frac{1}{2} X_2 + e^-$ (1.21)

The EMF of this galvanic cell is thermodynamically well defined, provided thermodynamic equilibrium exists at each electrode (i.e. reversible electrodes) and is related to the difference in the activity of neutral form of conducting species (X_2) by the following relation:

$$E = \frac{RT}{nF} \int_{a_{X2}^{I}}^{a_{X2}^{II}} t_{ion} dln a_{X2} \qquad (1.22)$$

where E is the open cell EMF of the galvanic cell, n is the number of moles of electrons involved in the electrochemical reaction, F is the Faraday constant i.e. amount of charge carried by 1 mole of electrons (96485 C mol^{-1}) and R is the universal gas constant (8.314 J mol^{-1} K^{-1}). When t_{ion} of conducting species is unity and independent of its activity (t_{ion} is actually a complex function of temperature and activity), eqn. (1.22) can be rewritten as

$$E = \frac{RT}{nF} \ln \left(\frac{a_{X2}^{II}}{a_{X2}^{I}}\right) \qquad (1.23)$$

If the solid electrolyte is perfect X^- ion conductor then electrons should move through external circuit from one electrode to other electrode (anode to cathode) whereas ions should move through the electrolyte.

The change in Gibbs energy of the electrochemical cell reaction can be related to the measured EMF value between two terminals of the isothermal galvanic cell by means of Nernst's equation,

$$\Delta G^o = -n F E^o \qquad (1.24)$$

High impedance electrometers (impedance > 10^{10} Ω) are used for EMF measurements. The total current through external circuit should be zero. Under these conditions resultant voltage measured across the galvanic cell is termed ‘open circuit voltage’.

Solid electrolyte galvanic cell technique, though seemingly simple, is associated with many experimental difficulties. Selection of proper electrolyte, reference electrodes, well defined phase relationships in the experimental system, cell environment are some of the constraints which have to be taken care of, for obtaining meaningful data. A number of tests should be performed (mentioned below) to ensure proper functioning of solid state electrochemical cell. (i) Cell reversibility should be checked by passing small amount of current in either direction. (ii) EMF must be reproducible on thermal cycling, (iii) It should be independent of small variations in flow rate of gas. (iv) At a fixed temperature, open circuit EMF between identical electrodes (i.e. electrodes of equal chemical potential) should be zero.

1.9 Calorimetric Methods

‘Calorimetry’ is defined as the measurement of energy in the form of heat. In calorimetry, thermal energy changes associated with the change in state of a system are measured. This change in state may be change in temperature, phase transition, change in pressure or volume, chemical composition or any other property of the system which is accompanied by thermal energy change [44, 53, 54]. Several types of calorimeters are used in experimental thermodynamics. A calorimeter, in general, has (i) a reaction vessel known as calorimeter proper in which thermal processes occur and (ii) a shield which is kept at constant or varying temperature. The following equation relates the heat change measured in the calorimeter to the temperature change.

$$\delta Q = L\,\delta t = W\,\delta T_c + K\,(T_c - T_s)\,\delta t \qquad (1.25)$$

where δQ = quantity of heat evolved or absorbed in the calorimeter

L = rate of heat absorption or evolution

δt = duration of heat pulse

W = water equivalent of the calorimeter

δT_c = change in temperature of calorimeter

K = thermal exchange constant

T_c = temperature of calorimeter

T_s = temperature of shield

Although calorimeters are classified into different groups based on various considerations, the most important classification (Wittig classification) [54, 55] is based upon the parameters mentioned in equation (1.25).

1.9.1 Isothermal Calorimeters

An isothermal calorimeter is one in which $T_c = T_s$ and is constant during measurements. These calorimeters use a phase change to maintain constancy of temperature. Bunsen ice calorimeter is the best example of a truly isothermal calorimeter. The reaction container is surrounded by a mixture of ice and water whose proportions are maintained constant. Any thermal energy change due to reaction causes melting of ice or freezing of water. From the change in volume associated with the phase transformation, quantity of heat involved in the process is calculated. Organic liquids like diphenyl ether have also been used in isothermal calorimeters in place of water [56]. Liquid-vapour phase change is employed here to maintain constancy of temperature.

1.9.2 Adiabatic Calorimeters

Adiabatic calorimeter is one in which $T_c = T_s$ but varying. Hence there is no heat transfer between the calorimeter and the shield [57]. The temperature of the shield is adjusted to be equal to that of reaction vessel (proper) at all times, by appropriate thermal control. Electrical energy is supplied to raise the temperature of the calorimeter by a few degrees. From the quantity of electrical energy supplied to raise the temperature of the calorimeter, heat capacity of the sample is calculated. Adiabatic calorimetry is the most accurate method for the determination of heat capacity. In adiabatic calorimeter, the reaction vessel is surrounded by many radiation shields and differential thermocouples are used to measure the difference between the temperature of the vessel and the shield and the output of the thermocouples control the heater circuits to maintain adiabatic conditions. Adiabatic calorimetry is used over a wide range of temperatures; from 4 K to 1700 K.

1.9.3 Isoperibol Calorimeters

The name ‘isoperibol’ means isothermal surroundings. An isoperibol calorimeter is one where T_s is constant and T_c is varying. Varying temperature difference between calorimeter and shield makes it difficult to control the heat leak. The heat exchange between the calorimeter and the surrounding or shield is minimized by packing the inter-space with highly insulating material. The high temperature drop calorimeter used in this study is also an isoperibol calorimeter. Drop calorimeter is an example of isoperibol calorimeter. In the most common version of this technique, sample which is thermally equilibrated at temperature T, is rapidly dropped into a calorimeter at lower temperature

T_0 and the enthalpy increment $H_T - H_{T_0}$ is measured. The enthalpy of sample is determined from the temperature rise of the calorimeter. A typical calorimeter signal (Fig. 3) indicates the increase in temperature of the calorimeter as a function of time. The area under ΔT (t) vs time curve is calculated. This area is proportional to the total quantity of heat involved in the process. The proportionality constant is obtained by dropping standards (whose heat content is known precisely) e.g. α – alumina. Once proportionality constant is known, quantity of heat absorbed or released by an unknown sample is obtained from the measured area under ΔT (t) vs time curve. This method is suitable for samples which do not undergo any phase transformation from temperature T to T_0. When the sample is dropped from high temperature to low temperature, it may not attain the true equilibrium state and may be present in metastable state. The samples which undergo phase transformations in the temperature range of measurements; inverse drop calorimetric technique is used. In this technique, the sample is maintained at low temperature T_0 and dropped in the calorimeter proper which is maintained at a high temperature T.

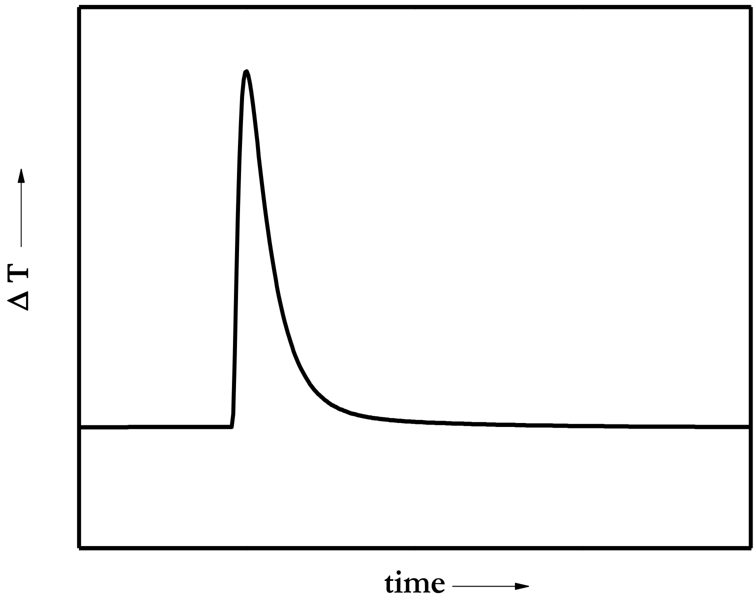

Fig. 1.3 Typical calorimetric signal

1.9.4 Heat Flow Calorimeters

In heat flow calorimeters, the temperature difference between the calorimeter and surroundings (T_c-T_s) is maintained at a non-zero constant value. The thermal exchange between the calorimeter and surroundings is used directly to evaluate the absorption or evolution of thermal energy in the sample. This type of calorimeter is also called as conduction calorimeter. Tian-Calvet calorimeters [58] used for high temperature studies belong to this type. Twin calvet type calorimeter consists of two symmetrically mounted cells contained in the calorimetric block [59]. The temperature difference between each cell and calorimetric block is monitored by thermopiles. The calorimeter is calibrated with sample of known heat capacity.

1.9.5 Differential Scanning Calorimeters

Diffential scanning calorimetry is employed for the measurement of heat capacity and enthalpy of transformation. This calorimeter contains sample and reference cells. The sample and the reference are maintained at the same temperature during the heating programme by supplying electrical energy to the sample or reference cell (Power compensated DSC). This extra input of electrical energy which is supplied to maintain the same temperature is measured and related to the heat capacity of the sample. In heat flux DSC, temperature difference between reference and sample cell is measured and related to the enthalpy difference between the sample and the reference.

Part III

1.10 Thermogravimetry as a tool for kinetic analysis

Thermoanalytical techniques e.g. thermogravimetric analysis (TGA), differential thermal analysis (DTA), differential scanning calorimetry (DSC) are extensively used to study kinetics of a thermally stimulated chemical reaction. The rate of any chemical reaction can be parameterized in terms of three major variables i.e. temperature, extent of reaction and pressure. Reaction rate can be described by the following relation:

$$\frac{d\alpha}{dt} = k(T).f(\alpha).g(P) \tag{1.26}$$

where α is the conversion fraction, k(T) is rate constant, f(α) is the conversion function dependent on mechanism of the reaction, g(P) is a function which shows reaction rate dependence on pressure [60].

Pressure dependence on reaction rate g(P), is generally ignored in most of the kinetic methods used in the area of thermal analysis. Many of the solid state reactions which involve gaseous product (formation and decomposition) e.g. $A_{solid} + B_{gas} \rightarrow C_{solid}$ or $A_{solid} \rightarrow B_{gas} + C_{solid}$ strongly depend upon pressure. In these reactions, $g(P)$ is taken constant by supplying large excess of gaseous reactant or by removing efficiently gaseous product. In these cases reaction rate (eqn. (1.26) can be rewritten as

$$\frac{d\alpha}{dt} = k(T).f(\alpha) \tag{1.27}$$

The extent of reaction, α is determined experimentally as a fraction of the overall change in physical property that accompanies the reaction. For a gravimetric measurement α is defined by

$$\alpha = \frac{m_o - m_t}{m_{o-} m_\infty} \tag{1.28}$$

where m_o is weight of the sample at the beginning, m_t is weight at time t, m_∞ is the final weight. Therefore, the value of α can vary from 0 to 1 as reaction proceeds to completion.

The temperature dependence of the rate constant k is typically parameterized through the Arrhenius equation:

$$k(T) = Aexp(\frac{-E_\alpha}{RT}) \tag{1.29}$$

where A is the pre exponential factor (frequency factor) [60, 61], E_α is the activation energy and R is the universal gas constant. Effective activation energy (experimentally determined kinetic parameter) strongly depends upon the temperature, extent of conversion and can take negative values [62-64].

The temperature is controlled by a proportional–integral–derivative (PID) temperature controller. The temperature program can be isothermal i.e., T = constant, or non-isothermal, T= T(t). In most of the common non-isothermal methods temperature varies linearly with time

$$\frac{dT}{dt} = \beta = constant \tag{1.30}$$

where β is the heating rate.

1.10.1 Isothermal vs Non-isothermal methods

Kinetic parameters (reaction model, pre-exponential factor, effective activation energy) can be obtained from isothermal experiments. Eqn. (1.27) can be rewritten as

$$\frac{d\alpha}{f(\alpha)} = k(T)dt \tag{1.31}$$

Rate constant can be obtained upon integrating eqn. (1.31)

$$g(\alpha) = \int_0^\alpha \frac{d\alpha}{f(\alpha)} = \int_0^t k(T)dt = kt \tag{1.32}$$

Wide variety of reaction models g(α) have been reported in literature [65]. The possible mechanism is chosen based on the best linear fit of various g(α) functions with highest correlation coefficient and low standard deviation. From the plot of g(α) vs time (eqn. (1.32)) rate constant k(T) can be obtained at various temperatures. Using Arrhenius equation (eqn. (1.29)), E_α and A are evaluated. The biggest disadvantage of isothermal experiments is limited temperature range. At lower temperatures it becomes very difficult to reach complete conversion over a reasonable time period. At high temperatures, time elapses before sample attains the required temperature and during this time i.e., before isothermal regime sets in, significant extent of reaction takes place especially when process follows decelerating kinetics (i.e., rate is maximum when α is zero).

Non-isothermal experiments involve heating the sample at constant rate ($\beta = constant$). The non-isothermal rate equation can be represented as

$$\frac{d\alpha}{dT} = \frac{1}{\beta}.k(T).f(\alpha) \tag{1.33}$$

Integrating eqn. (1.33),

$$g(\alpha) = \int_0^\alpha \frac{d\alpha}{f(\alpha)} = \int_0^T \frac{k(T)}{\beta} dT \tag{1.34}$$

The advantage of non-isothermal methods compared to isothermal methods is that kinetic parameters can be obtained from a single thermo gravimetric curve for the whole temperature range. Hence, these methods require less number of experimental data as compared to isothermal methods. However, under non-isothermal conditions f(α) and k(T) both vary and hence it becomes difficult to recognize reaction model type, especially identification of acceleratory (rate is maximum when α is 1) and sigmoidal models (at initial stage reaction model is acceleratory and at final stage behaviour is decelerating type). Hence, the best way for proper selection of reaction model is the combination of non-isothermal and isothermal experiments.

1.10.2 Differential vs integral methods

Numerous differential and integral methods have been proposed to obtain Arrhenius parameters from equation (1.34). Differential and integral methods are best suitable for analyzing differential (e.g. DSC, DTA) and integral (e.g., TGA) data respectively. Numerical integration and differentiation methods are available to convert differential data to integral data and vice versa but differentiating integral data may tend to magnify noise. Data smoothening can be done at a cost of introducing systematic error in smoothened data. The function used for smoothening should not distort real reaction features. Differential methods are more sensitive in revealing kinetic details of a process but suffer with problem of baseline selection. In integral methods baseline selection is quite straightforward [65].

References

[1] Kumar A, Chatterjee S. Electricity Sector in India – Policy and Regulation, Oxford University Press. 2012.

[2] Orbach R L. The Achilles Heel of Nuclear Energy, Disposal of Spent Fuel, The Energy Institute, The University of Texas at Austin, 2009.

[3] Grover R, Chandra S (2006) Scenario for growth of electricity in India. Energy Policy. 2006; 34(17): 2834-47.

[4] Ramachandran A, Gururaja J. Perspectives on Energy in India. Annual Review of Energy.1977; 2: 365-86.

[5] Ramanna R. Inevitability of nuclear energy. Curr Sci. 1997; 73 (4): 319-26.

[6] Ganguly C. Development of plutonium-based advanced LMFBR fuels and thoria based PHWR fuels in India, IAEA-TECDOC-352, 1985; pp 107-27.

[7] Schapira J P, Singhal R K. Radiological Impact at the Extraction Stage of the Thorium Fuel Cycle. Nucl Technol. 1999; 128: 25-34.

[8] Grover R, Green growth and role of nuclear power: A perspective from India. Energy Strategy Rev. 2013; 1: 255-60.

[9] Weigel F, Uranium: In the chemistry of the actinide elements, Vol. 1, Second Edn., Kats J J, Seaborg G T, Morss L R (Eds.). Chapman and Hall Ltd, London, Great Britain, 1986, 169-442.

[10] Waltar A E, Reynolds A B. Fast breeder reactors. Pergamon Press. ISBN: 9780080259833, 1981.

[11] Cochran T B, Feiveson H A, Patterson W, Pshakin G, Ramana M V, Schneider M, Suzuki T, von Hippel F (2010) Fast breeder reactor programs: history and status. International Panel on Fissile Materials.

[12] Chetal S C, Balasubramaniyan V, Chellapandi P, Mohanakrishnan P, Puthiyavinayagam P, Pillai C P, Raghupathy S, Shanmugham T K, Pillai C S. The design of the prototype fast breeder reactor. Nucl Eng Des. 2006; 236(7): 852-60.

[13] Ganguly C, Hegde P V, Jain G C, Basak U, Mehrotra R S, Majumdar S, Roy P R Development and Fabrication of 70% PuC—30% UC Fuel for the Fast Breeder Test Reactor in India. Nucl Technol. 1986; 72(1): 59-69.

[14] Anantharaman K, Shivakumar V, Saha D (2008) Utilisation of thorium in reactors. J Nucl Mater. 2008; 383(1): 119-21.

[15] Sinha R, Kakodkar A. Design and development of the AHWR—the Indian thorium fuelled innovative nuclear reactor. Nucl Eng Des. 2006; 236(7): 683-700.

[16] Kumar K V S, Babu A, Anandapadmanaban B, Srinivasan G. Twenty five years of operating experience with the fast breeder test reactor. Energy Procedia. 2011; 7: 323-32.

[17] Chetal S C, Chellapandi P, Puthiyavinayagam P, Raghupathy S, Balasubramaniyan V, Selvaraj P, Mohanakrishnan P, Raj B (2011) Current status of fast reactors and future plans in India. Energy Procedia. 2011; 7: 64-73.

[18] Srinivasan G, Kumar K V S, Rajendran B, Ramalingam P V. The fast breeder test reactor-design and operating experiences. Nucl Eng Des. 2006; 236(7): 796-811.

[19] Raj B, Kamath H S, Natarajan R, Rao P R V. A perspective on fast reactor fuel cycle in India. Progress in Nuclear Energy. 2005; 47(1): 369-379.

[20] Sinha R, Kakodkar A. The road map for a future Indian nuclear energy system. No. IAEA-CN-108. 2003.

[21] Olander D R, Fundamental Aspects of Nuclear Reactor Fuel Elements, U.S. Department of Energy, 1976.

[22] Matzke Hj. Science of Advanced LMFBR fuels, North-Holland Publishers, Amsterdam, 1986.

[23] Anthonysamy S, “Studies on the preparation and some solid state properties of the solid solutions of urania and thoria” Ph.D. Thesis, University of Madras (2000).

[24] Vasudeva Rao P R, Anthonysamy S, Krishnaiah M V, Chandramouli V. Oxygen potential and thermal conductivity of (U, Pu) mixed oxides. J Nucl Mater. 2006; 348: 329-34.

[25] Kato M. Oxygen Potentials and Defect Chemistry in Nonstoichiometric $(U,Pu)O_2$, Stoichiometry and Materials Science – When Numbers Matter, Dr. Alessio Innocenti (Ed.), ISBN: 978-953-51-0512-1, InTech, 2012.

[26] Kato M, Tamura T, Konashi K, Aono S. Potentials of Plutonium and Uranium Mixed Oxide, J Nucl Mater. 2005; 344: 235-39.

[27] Kato M, Tamura T, Konashi K. Oxygen potentials of Mixed Oxide Fuels for Fast Reactors, J Nucl Mater. 2009; 385: 419-23.

[28] Kato M, Takeuchi K, Uchida T, Sunaoshi T, Konashi K. Oxygen potential of $(U_{0.88}Pu_{0.12})O_{2\pm x}$ and $(U_{0.7}Pu_{0.3})O_{2\pm x}$ at high temperatures of 1673-1873K, J Nucl Mater. 2011; 414: 120-25.

[29] Markin T L, McIver E J. Thermodynamic and phase studies for plutonium and uranium –plutonium oxides with application to compatibility calculations, 3rd International Conference on Plutonium, 1965; 845-57.

[30] Woodley R E. Equilibrium Oxygen Potential-Composition Relations in $U_{0.75}Pu_{0.25}O_{2-x}$, J. Am. Ceram. Soc. 1973; 56: 116-19.

[31] Woodley R E, Adamson M G. The oxygen potential of near- and non-stoichiometric urania-25 mol% plutonia solid solutions: A comparison of thermogravimetric and galvanic cell measurements. J Nucl Mater. 1979; 82: 65-75.

[32] Woodley R E. Oxygen potentials of plutonia and urania-plutonia solid solutions. J Nucl Mater. 1981; 96: 5-14.

[33] Sorenson O T. Thermodynamic Studies at Higher Temperatures of the Phase Relationships of Substoichiometric Plutonium and Uranium/Plutonium Oxides, Plutonium 1975 and Other Actinides, North-Holland, Amsterdam, 1976; 123.

[34] Edwards J, Wood R N, Chilton G R. Oxygen potentials of uranium-plutonium oxides in the near stoichiometric region. J Nucl Mater. 1985; 130: 505-12.

[35] Kleykamp H. Chemical States of the Fission Products in Oxide Fuels. J Nucl Mater. 1985; 131: 221-46.

[36] Khanna A S. Fuel-Cladding chemical interaction in mixed oxide liquid metal fast breeder reactors – A Review. Reactor Research Centre (RRC-53), 1982.

[37] Adamson M G, Aitken E A, Lindemer T B. Chemical thermodynamics of Cs and Te fission product interactions in irradiated LMFBR mixed-oxide fuel pins. J Nucl Mater. 1985; 130: 375-92.

[38] Chattopadhyay G, Juneja J M. A thermodynamic database for tellurium bearing systems relevant to nuclear technology. J Nucl Mater. 1993; 202: 10-28.

[39] Cordfunke E H P, Konings R J M. Chemical Interaction in Water Cooled Nuclear Fuel: A Thermochemical Approach. J Nucl Mater. 1988; 152: 301-09.

[40] Fee D C, Johnson C E. Fuel-Cladding chemical interaction in uranium-plutonium oxide fast reactor. J Nucl Mater. 1981; 96: 80-104.

[41] Manideepa Ali, “Thermochemical studies on some alloys and refractory oxides of importance in nuclear technology” Ph.D. Thesis, University of Mumbai (2003).

[42] Chase M W, Davies C A, Dourey J R, Frury D J, McDonald, Syverud A N. JANAF Thermochemical Tables, 3rd Ed., J Phys Chem Ref Data. 1985.

[43] Ipser H, Vapor pressure methods: A source of experimental thermodynamic data. Berichte der Bunsengesellschaft für physikalische Chemie. 1998; 102(9): 1217–24.

[44] Kubaschewski O, Alcock C B, Spencer P J. “Materials Thermochemistry” Volume 6, Pergamon Press, New York. 1993.

[45] Margrave J L. “The Characterization of High Temperature Vapours” Wiley, New York. 1967.

[46] Wahlbeck P G. Comparison and interrelations for four methods of measurement of equilibrium vapor pressures at high temperatures. High Temp Sci. 1986; 21: 189- 232.

[47] Richardson F D, Alcock C B. “Physicochemical Measurements at High Temperatures” Ed. Bockris J O’M, Academic Press, New York, 1959.

[48] Sreedharan O M, “Some Thermodynamic Studies on High Temperature Materials” Ph.D. Thesis, University of Bombay (1975).

[49] Subbarao E C. “Solid Electrolytes and their Applications” Plenum Press, New York, 1980.

[50] Tom Mathews, “Phase equilibria and thermodynamic studies on selected ceramic oxide systems” Ph.D. Thesis, Department of Metallurgy, Indian Institute of Science, Bangalore (1993).

[51] Ipser H, Mikula A, Katayama I. Overview: the EMF method as a source of experimental thermodynamic data. Calphad. 2010; 34: 271-78.

[52] Moser Z, Fitzner K. The use of experimental thermodynamic data in the phase equilibria verification. Thermochim Acta. 1999; 332: 1-19.

[53] Rapp R A. “Physicochemical Measurements in Metals Research” Vol. IV, Part I, Interscience Publishers, New York (1970).

[54] Wittig F E. Calorimetric method at higher temperatures. Pure & Appl Chem. 1961; 2: 183-204.

[55] Wittig F E. Metal Chemistry, NPL Symp. No. 9, 1958, HMSO, 1959, paper 1A.

[56] Farukawa G T, Ginnings D C, McCoskey R E, Nelson R A. Calorimetric properties of diphenyl ether from 0° to 570°K. J Res NBS. 1951; 46: 195-206.

[57] Westrum E F. Advances in High Temperature Chemistry. Vol. 1, Ed. Eyring L. Academic Press, New York, 1967.

[58] Rossini F D. Experimental Thermochemistry, Vol. I, Interscience Publishers, New York, 1956.

[59] Kleppa O J. A new twin high-temperature reaction calorimeter. The heats of mixing in liquid sodium-potassium nitrates. J Phys Chem. 1960; 64; 1937-40.

[60] Vyazovkin S, Burnham A K, Criado J M , Pérez-Maqueda L A, Popescu C, Sbirrazzuoli N. ICTAC Kinetics Committee recommendations for performing kinetic computations on thermal analysis data. Thermochim Acta. 2011; 521; 1-19.

[61] Khawam A, Flanagan D R. Solid-State Kinetic Models: Basics and Mathematical Fundamental. J Phys Chem B. 2006; 110; 17315-28.

[62] Atkins P, De Paula J. Physical Chemistry (9th ed.), W.H. Freeman, New York 2010.

[63] Vyazovkin S. Kinetic concepts of thermally stimulated reactions in solids: a view from a historical perspective. Int Rev Phys Chem. 2000; 19: 45–60.

[64] Vyazovkin S. On the phenomenon of variable activation energy for condensed phase reactions. New J Chem. 2000; 24: 913–917.

[65] Brown M E, Dollimore D, Galwey A K. Comprehensive Chemical Kinetics, Vol. 22, Elsevier, Amsterdam 1988.

Chapter 2

EXPERIMENTAL

2

This chapter describes the chemicals, materials, instruments used for carrying out various experiments and the experimental procedures employed in the present work. The sample preparation for various measurements carried out in this study is also described. The analytical methods used for the determination of various metal ions are also discussed in this chapter.

2.1 Chemicals

Acids - Acids such as nitric and sulphuric acids (AR grade) were obtained from M/s. Merck, India. These were used as such without any further purification.

BASF catalyst - Active Cu impregnated $MgSiO_3$ pellets (popularly known as BASF catalyst) were supplied by M/s. BASF India Ltd., Mumbai, India.

Calcia stabilized zirconia (CSZ) tube - One end closed calcia stabilised zirconia (CSZ) solid electrolyte tubes having a flat bottom was supplied by M/s. Nikkato Corporation, Japan.

Chromium (III) oxide - Analytical Reagent grade Cr_2O_3 powder of purity better than 99.9% was procured from M/s. Aldrich Chemicals, USA.

Ferric (III) oxide - Analytical Reagent grade Fe_2O_3 powder of purity better than 99.9% was procured from M/s. Aldrich Chemicals, USA.

Gases - High-purity oxygen, argon, hydrogen, helium gases were obtained from M/s. Indian Oxygen Limited, Chennai, India.

Indium - Indium ingot of 99.99% purity was obtained from M/s Nuclear Fuel Complex, India.

Indium oxide powder – Spec pure In_2O_3 powder was obtained from M/s Johnson Mathey Chemical Limited, England.

Lanthanum (III) hydroxide - Analytical Reagent grade $La(OH)_3$ powder of purity better than 99.9% was procured from M/s. Aldrich Chemicals, USA.

MOX $(U_{0.54}Pu_{0.46})O_2$ pellets - The MOX $(U_{0.54}Pu_{0.46})O_2$ pellets were obtained from Bhabha Atomic Research Centre, Mumbai, India.

Magnesium perchlorate - Analytical Reagent grade $Mg(ClO_4)_2$ powder of purity better than 99.9% was procured from M/s. Alfa Aesar, USA.

Nickel (II) oxide - Analytical Reagent grade NiO powder of purity better than 99.9% was procured from M/s. Aldrich Chemicals, USA.

Platinum paste - Platinum paste was supplied by M/s Eltecks Corporation, India.

Tellurium (IV) oxide - Analytical Reagent grade TeO_2 powder of purity better than 99.9% was procured from M/s. Aldrich Chemicals, USA.

Titanium Sponge - Titanium sponge of purity better than 99.9% was procured from M/s. Alfa Aesar, USA.

Torrseal - Torrseal was supplied by M/s. Varian, USA.

Tungsten wire - Tungsten wire (99.95% pure, 1 mm diameter) was supplied by M/s. Leico Industries Inc., USA.

Zirconium Sponge - Nuclear grade zirconium sponge was obtained from Nuclear Fuel Complex, India.

2.2 Instrument/Facility

2.2.1 Electronic single pan balance

A calibrated electronic balance (SHIMADZU make) with a sensitivity of ± 0.01 mg was used for weighing various chemicals.

2.2.2 High impedance electrometer

A high impedance electrometer (input impedance >10^{14} Ω, M/s Keithley, U.S.A, model-6514) was used for the measurement of cell EMF.

2.2.3 Mass Flow controller

Mass flow controllers were supplied by M/s. Smart Trak 2, Sierra Instruments Inc., France.

2.2.4 Refrigeration unit

Refrigeration unit having temperature range -40 to +100°C was supplied by M/s. Julabo GmbH, Germany.

2.2.5 Energy Dispersive X-ray Fluorescence (EDXRF) Spectrometer

A Jordan Valley EX-3600 EDXRF spectrometer, equipped with a Rh source, filters (Ti, Fe, Cu, Rh, W) and a Si(Li) detector, with 12.5µm thick Be window, was used for XRF measurements. The x-ray generator is 50 Watt, 50 kV oil cooled end window, front anode X-ray tube. The instrument is equipped with 10-position sample chamber for measuring samples sequentially. Sample can be handled in solid, powder or liquid form. Analog to digital converter (ADC) and multi-channel analyser (MCA) were coupled to a Pentium IV PC. The system software nEXT is used for spectral acquisition and the analysis runs under Windows NT 4.0 operating system. Si (Li) semiconductor detector has a resolution of 150 eV at 5.9 keV (Mn K_{α}) and is capable of acquiring a spectrum containing many lines from various elements simultaneously in the 1-40keV region. The system is sensitive to elements from Sodium to Uranium.

Principle of Energy Dispersive X-ray Fluorescence (EDXRF) Technique

X-ray fluorescence [1] technique is a non-destructive technique for the analysis of chemical elements. In this technique, x-rays are used to excite atoms in the sample (solid or liquid). The excited atoms emit x-rays with energy characteristic of each element in the sample. By knowing the intensity and energy of the characteristic X-rays, the sample can be analysed for its elemental composition. XRF can determine elements with varying concentration ranging from ppm (parts per million) to % level. Using standards, XRF can accurately quantify the elemental composition.

2.2.6 Neutron Activation Analysis (NAA)

For neutron activation analysis, samples were irradiated at 20 kW for a period of 1h at a neutron flux of 6.5×10^{11} neutrons cm^{-2} s^{-1} in pneumatic fast transfer system (PFTS) position of Kalpakkam Mini reactor (KAMINI). Gamma lines from excited sample were counted using HPGe detector.

Principle of Neutron Activation Analysis (NAA)

Neutron activation analysis (NAA) is also a non-destructive technique for the quantitative determination of elements in a vast amount of materials. It allows the precise identification and quantification of the elements. It is a nuclear process in which event used is (n, gamma) reaction. NAA relies on excitation by neutrons so that the treated sample emits gamma-rays [2]. Formation of compound nucleus takes place when a neutron interacts with the target nucleus via a non-elastic collision. The excitation energy of the compound nucleus is due to the binding energy of the neutron with the nucleus. The compound nucleus almost instantaneously de-excites into a more stable configuration through emission of one or more characteristic prompt gamma rays.

2.2.7Transpiration apparatus

A simultaneous Thermogravimetry (TG) and Differential Thermal Analyser (DTA) instrument was employed as the transpiration set-up for vapour pressure measurements. The principle of this technique is given below:

Principle of Thermogravimetry (TG) and Differential Thermal Analysis (DTA) techniques

Thermo gravimetric analysis (TGA) is a technique, which monitors changes in the mass of a sample as a function of temperature whereas DTA can be used to get the information on the associated thermal effects [3, 4]. In DTA, the sample under study and an inert reference are made to undergo identical heating/cooling cycles, while recording the temperature difference between the sample and the reference [5]. In the event of any thermal effect, the temperature difference between the sample and the reference results in the appearance of endothermic or exothermic peaks. The area under a DTA peak can be correlated to the enthalpy change in the process for the sample by proper calibration.

Both vertical and horizontal thermal analysis systems (TG-DTA) were employed as transpiration set-up for vapour pressure measurements. Details of these instruments are given below:

2.2.7.1 Vertical thermal analysis system

A vertical thermal analysis system (model SETSYS Evolution 16/18 M/s. Setaram, France) was used as a transpiration set-up for the vapour pressure measurements. A schematic of this TG-DTA assembly is given in Fig. 2.1. This equipment has a mass sensitivity of 0.1 μg. A correction factor is generated for apparent mass change as a function of time at different isothermal temperatures under different flow rates in the blank runs carried out with empty sample and reference pans under carrier gas atmosphere. Platinum crucible (capacity–100 μl) was used as the sample container in all the experiments. The accuracy of temperature measurement in this study was established by measuring the melting points of pure metals viz., gold, palladium, and aluminium and was found to be ±1K. The calibration was found to conform to ITS-90 scale [6]. The temperature was measured using Pt-Rh6% / Pt-Rh30% thermocouples (3 numbers) which are in very close contact with the sample holder [Fig. 2.2]. The flow rate of the carrier gas was controlled and measured using a mass flow controller.

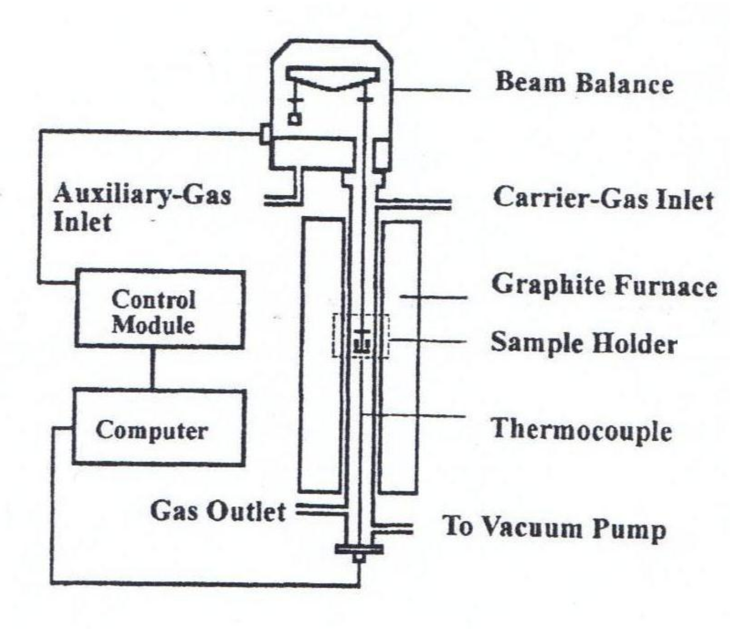

Fig. 2.1 TG-DTA assembly

Fig. 2.2 Sample holder

This instrument was also used for study of formation kinetics of La_2TeO_6. High purity oxygen was used as the reactive carrier gas in all the kinetic experiments. The flow rate of oxygen was maintained at 1.188 $dm^3\ h^{-1}$. Platinum crucible (capacity–100 μl) was used as the sample container in all the experiments. A program with three heating rate segments was used for this study. In the first segment the sample was heated from 298 to 1023 K at a heating rate of 10 K min^{-1}. In the second segment the sample was held isothermally at 1023 K for 5 min. and in the third segment the sample was heated from 1023 to 1203 K at different heating rates viz., 2, 3, 5, 10, 15 K min^{-1}. Isothermal experiments were carried out by heating the sample at pre-determined temperatures viz. 1025 and 1045 K for 45 min.

2.2.7.2 Horizontal thermal analysis system

A horizontal thermo gravimetric analyser (TGA / SDTA 851^e) supplied by M/s. Mettler Toledo, Switzerland was used as a transpiration set-up. It was calibrated for the measurement of vapour pressure by using TeO_2 (s) and $CdCl_2$ (s) as standards [7]. The horizontal design of the thermal analyser helped minimize the errors in measurement of weight caused by thermal diffusion. The location of the sample pan in the uniform temperature zone of the furnace minimized the errors due to buoyancy and thermal expansion of the beam (Fig. 2.3). This equipment has a weight sensitivity of 0.1 μg and a temperature sensitivity of 0.01K. A platinum crucible of 40 μl capacity was used as the sample container. The temperature was measured by using a ‘S’ type thermocouple (Pt-10% Rh vs Pt) which was in firm contact with the sample holder on which the Pt sample container was placed. The measurement of temperature was calibrated by measuring the melting points of pure metals viz., In, Al and Au. The calibration was found to conform to ITS-90 scale [6]. Oxygen was used as the carrier gas, the flow of which was controlled by using a mass flow controller. Each time a fresh sample was loaded to avoid errors due to sintering and surface depletion.

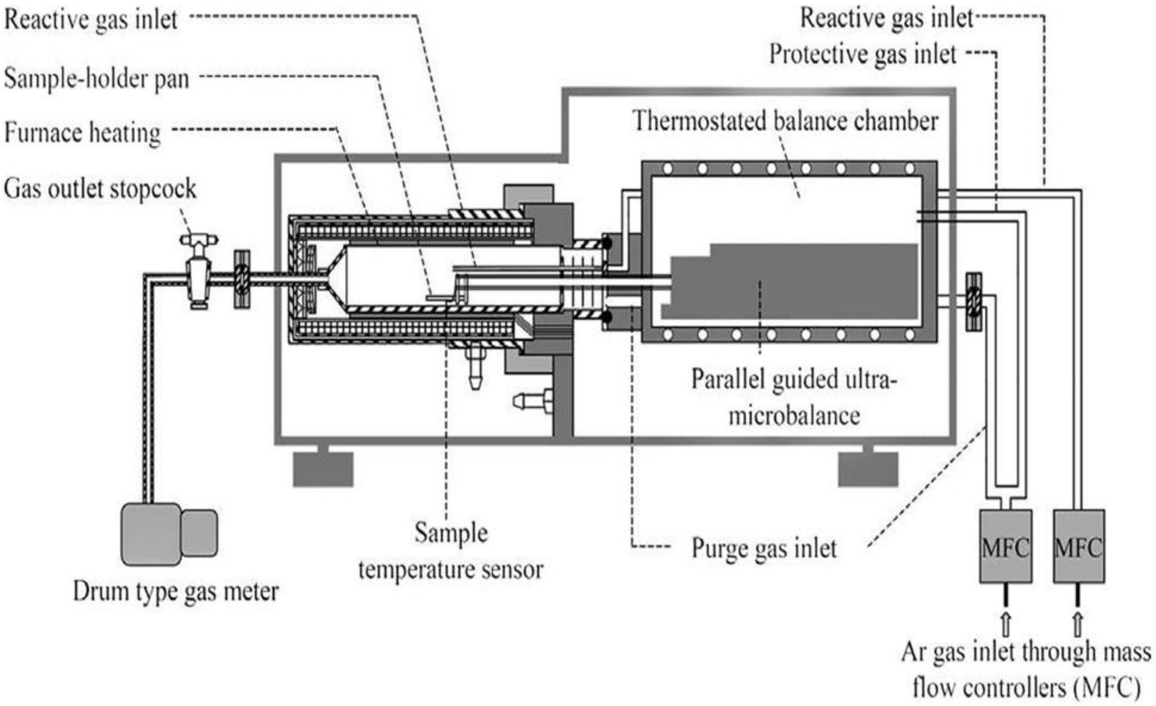

Fig. 2.3 Schematic of horizontal thermal analysis system used in this study

2.2.8 Calorimeter

Isoperibol type calorimeters were employed in the present study for the measurement of enthalpy increments. Both drop and inverse drop calorimeters were used for these measurements. Details of both are given below:

2.2.8.1 High temperature drop calorimeter

This calorimeter essentially consists of a nichrome wire wound furnace, with provision for heating and holding the sample at the experimental temperatures, and calorimeter proper [7].

The temperature of the furnace is measured using a Type K thermocouple and controlled using a proportional–integral–derivative (PID) temperature controller. The temperature of the furnace was controlled within ± 1K. The temperature of the sample was measured using Type K thermocouple placed near the sample. The calorimeter proper is a brass ‘receiving crucible’ maintained at 298 K maintained at 298 K (error ± 1K) using chilled water. The method of measurement of enthalpy increments has been described in the subsequent chapter. A photograph of the drop calorimeter used in the present study is shown in Fig. 2.4.

Fig. 2.4 Photograph of the home-built calorimeter

2.2.8.2 High temperature inverse drop calorimeter

A “Multi-Detector” high temperature calorimeter (MHTC-96) with a drop detector supplied by M/s. SETARAM, France was employed for enthalpy increment measurements. The tubular calorimetric drop detector consisted of a thermopile having 28 thermocouples in which a sample crucible and an empty reference crucible were positioned one above the other. The constituent thermocouples of this thermopile detector were positioned at different levels surrounding the outer surface of the crucibles so that an integrated heat exchange between the two crucibles was obtained as the output signal [8]. In the present study, a drop detector, made up of Pt – 30 % Rh / Pt – 6 % Rh thermocouples was employed. The detector placed in a gas-tight alumina tube was kept in the resistively heated graphite furnace. A photograph of MHTC-96 is shown in Fig. 2.5. A schematic of the calorimetric detector is shown in Fig. 2.6 and its enlarged view is shown in Fig. 2.7.

Fig. 2.5 Multi-detector High Temperature Calorimeter

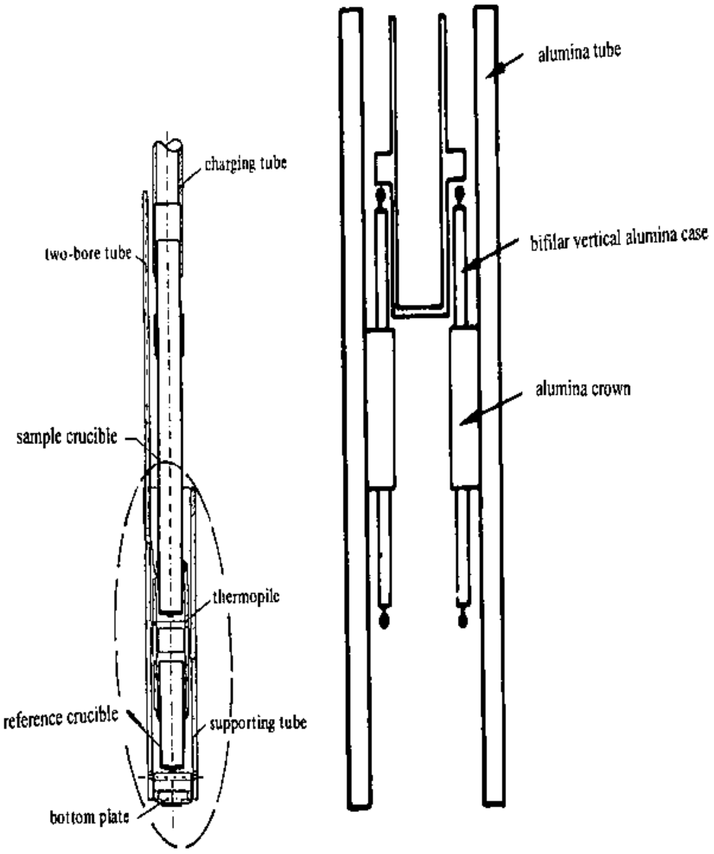

Fig. 2.6 Schematic of calorimetric detector with sample and reference crucibles

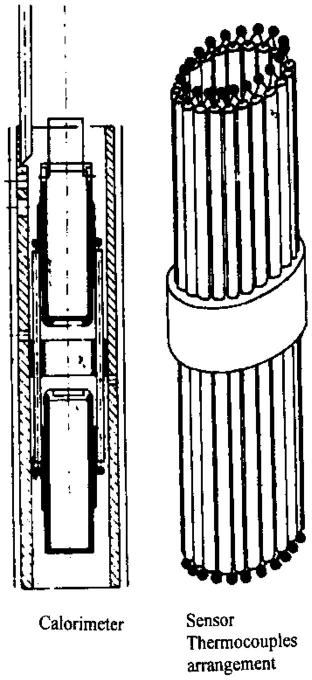

Fig. 2.7 Schematic diagram of the calorimetric detector

2.2.9 Scanning Electron Microscopy (SEM)

For microstructural and morphological studies scanning electron microscopy (SEM) (Philips XL30, The Netherlands) was used.

Principle of Scanning Electron Microscopy (SEM)

Surface features of powders and pellets can be studied by scanning electron microscope [9-11]. In a scanning electron microscope, an accelerated electron beam is focused and scanned over the specimen surface. Wavelength of the electron beam can be controlled by varying the velocity of electrons with the applied voltage. Interaction of electron beam with matter causes various physical phenomena such as absorption, reflection, backscatter and diffraction. In addition to the above said physical phenomenon, it also causes the emission of low energy secondary electrons and X – rays. In SEM, the effects of both due to the secondary emission and backscattered electrons are measured and surface feature in nanometer scale can be constructed. EDAX is one of the salient features of SEM and can be used to determine the elemental composition of the surface of the samples. When electrons from incident beam interact with atoms on the surface, secondary electrons from inner shells of the atoms are ejected out. Electrons from outer shells will drop into the vacant levels of the inner shells and this result in the emission of X – rays characteristic of the atom. Hence, by measuring the energy of these characteristic X – rays, information about the elemental composition of the sample surface can be obtained.

2.2.10 X-ray Diffraction (XRD)

Powder X-ray diffraction is an important standard tool for identification and characterization of minerals and other crystalline materials. By this technique information about the particle size, crystal structure and lattice parameters can be determined. It is used for quantitative analysis as well as qualitative identification of crystalline phases. In the present study, XRD studies were carried out by using an X-ray diffractometer (XPERT MPD system obtained from M/s. Philips, The Netherlands), employing Cu K_{α} radiation and Ni filter. The operating conditions were 30 kV and 20 mA in the angular range 10-80º in 2θ.

Principle of X-ray Diffraction (XRD)

X-ray diffraction is one of the most important characterization tools used in solid state chemistry and materials science [4, 12, 13]. It helps to derive the crystal structure and lattice parameters of a crystalline solid. Diffraction of a characteristic X-ray beam from the planes of crystalline solid takes place when the wavelength of the X-ray beam (in Å scale) is equal to the inter planner spacing of the solids. Characteristic X-rays are produced when the energetic electrons strike the target, made of a pure metal such as copper, molybdenum or chromium; it removes the inner (K) shell electrons. When this happens, other electrons from higher level shells drop into the vacant K-shell and in doing so emit a photon (X-ray) whose wavelength (energy) is characteristic of the metal target material. In order to remove the inner shell electron, the incoming electron must have energy greater than the difference in energy between the inner (K) shell electron and a free electron in the conduction band of the target metal. The X-ray radiation most commonly used is that emitted by copper, whose characteristic wavelength for the Kα radiation is 1.54184Å. Other metal targets commonly used in X-ray generating tubes include Cr (Kα-2.29 Å), Fe (Kα-1.94 Å), Co (Kα-1.79 Å), and Mo (Kα-0.71 Å).

X-ray diffraction by crystal is a scattering process where X-rays are scattered by the electrons of atoms/ions without change in wavelength. Only when certain geometrical conditions are satisfied, a diffracted beam is produced by such scattering, popularly known as Bragg’s law:

$$n\lambda = 2d \sin \theta \tag{2.1}$$

where λ is wavelength of the X-ray used, d is the inter planar spacing of the analyte and θ is angle of incidence of the X-rays and n is the order of reflection.

X-ray diffraction technique requires an X-ray source, sample under investigation and a detector. X-ray diffraction methods employ single crystals as well as powder samples. The main use of single crystal method is to determine the space group and crystal structure while the powder diffraction technique is widely used for phase identifications and crystallite size determinations. The diffraction pattern of an unknown mixture is usually compared with a powder diffraction file (PDF) collected and maintained by Joint Committee of Powder Diffraction Standards (JCPDS).From the powder diffraction patterns, various other useful information like effects of stress and strain on crystallites, thermal expansion of lattice, solid solution formation, phase transitions etc. can also be derived. High temperature XRD is useful to detect the phase changes occurring at elevated temperatures.

A schematic of a powder X-ray diffractometer is shown in Fig. 2.8.In case of powder diffraction technique, a monochromatic beam of X-rays strikes a finely powdered sample, where the crystallites present themselves in random orientation. When the angle of incidence of X-rays is at the Bragg's angle θ of a crystalline phase of the sample, there would be some crystallites with the appropriate lattice planes oriented for diffraction to occur. The diffracted beam is detected using a movable detector which is set to scan over a range of 2θvalues at a constant angular velocity. Generally, a 2θ range of 10 to 90 degrees is sufficient to cover the most useful part of the powder pattern with an interval of 0.02° with a counting time of 10 s at each interval.

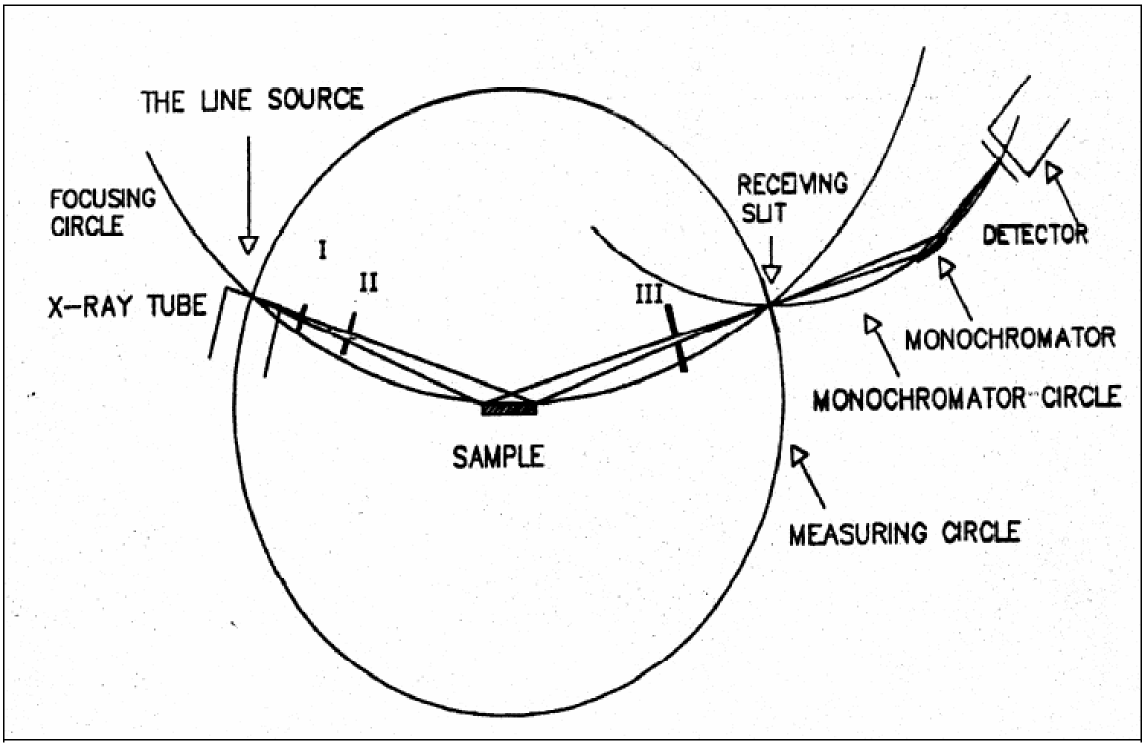

Fig. 2.8: Schematic of powder X-ray diffractometer

2.2.11 Experimental Assembly for oxygen potential measurement

A schematic of the experimental assembly used for oxygen potential measurement is shown in Fig. 2.9. This assembly essentially consists of three parts, (i) gas mixing set up (ii) equilibration chamber and (iii) an oxygen probe.

(i) Gas mixing set up - In the gas mixing set up either pure H_2 or H_2 pre-mixed with Argon (i.e. Ar-4% H_2 or Ar-8% H_2) were passed through a refrigerated pure water column maintained at a constant temperature using a proportional integral derivative (PID) temperature controller. The temperature of the refrigeration unit was maintained within ±1K.

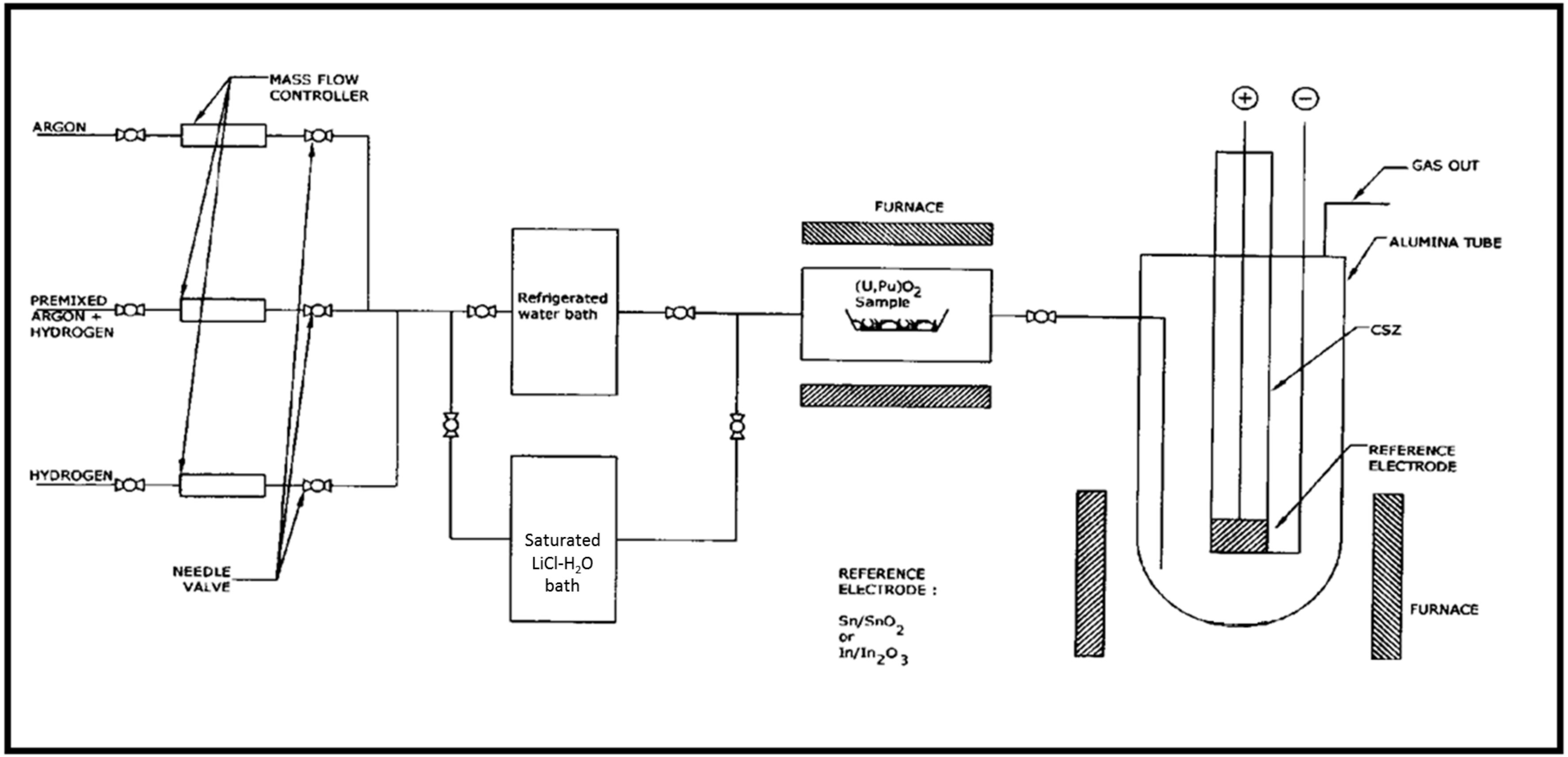

Fig. 2.9 Schematic of experimental assembly used for oxygen potential measurement

The flow rates of the gases were adjusted using mass flow controllers (MFC). The gas mixtures having low oxygen partial pressures were obtained by passing H_2 gas through a water bath saturated with lithium chloride.

H_2-CO_2 and CO-CO_2 gas mixtures can be employed for the measurements at higher oxygen potentials. In H_2-CO_2 gas mixture partial pressures of H_2 and CO_2 can be adjusted by varying the flow rates of these gases by using MFC. In CO-CO_2 gas mixture, CO_2 gas is passed through a tower containing Cu-Cu_2O redox couple at a constant temperature. The oxygen potential of the resultant gas mixture ($CO+CO_2$) can be varied by changing the temperature of the Cu-Cu_2O redox couple.

(ii) Equilibration Chamber – The equilibration chamber was placed in a resistance wire-wound, horizontal tubular furnace. The temperature of the furnace was controlled within ±2 K using a PID temperature controller. An alumina tube was used as the work-tube. The sample was contained in a recrystallized alumina boat and placed in the uniform zone of the furnace. The gaseous mixture of known H_2O/H_2 ratio (fixed oxygen potential) was passed over the MOX sample pellets for equilibration.

(iii) Oxygen probe – An oxygen probe was used to measure the oxygen potential of the gas mixture exiting the equilibration chamber. Calcia stabilized zirconia (CSZ) having a composition of ZrO_2-11 mol% CaO was employed as the solid electrolyte in the oxygen probe. The CSZ tube had the dimensions of 13 mm OD, 9 mm ID and 250 mm long. The upper and lower electrolytic domain boundaries of this solid electrolyte are shown in Fig. 2.10. Platinum paste was coated on the outer end of the CSZ tube (about 10 mm height)and fired at 1273 K for 4 h in air in order to get a porous platinum film whose continuity on the surface was checked by resistance measurements. After platinization, a Pt lead spot welded with Pt mesh fixed with the Pt paste was taken from the outer end of the CSZ tube. In and In_2O_3 mixture (in the weight ratio of 10:1), prepared by mixing was used as the reference electrode. A mixture of Sn and SnO_2 can also be used as reference electrode. In the present study, In-In_2O_3 mixture was loaded into the CSZ tube up to about 10 mm length. The reference electrode was sealed inside the CSZ tube under high-pure argon cover. After sealing the electrode was equilibrated at 723 K for 1 h. A tungsten wire was used as the inner lead. An alumina insulator was inserted over the tungsten lead. The inner chamber was sealed using Torrseal. A calibrated 'S type' (Pt-10% Rh vs Pt) thermocouple was used for the temperature measurements. The oxygen probe was housed inside an alumina tube. The EMF across the solid electrolyte (between tungsten and Pt leads) was measured using a high impedance millivolt meter. The probe was housed in a separate furnace kept at the optimum temperature, i.e., 873 K. Sample can also be placed just below the probe if temperature at which oxygen potential of the sample has to be measured is the same as that of oxygen probe. A schematic of oxygen probe is shown in Fig. 2.11.

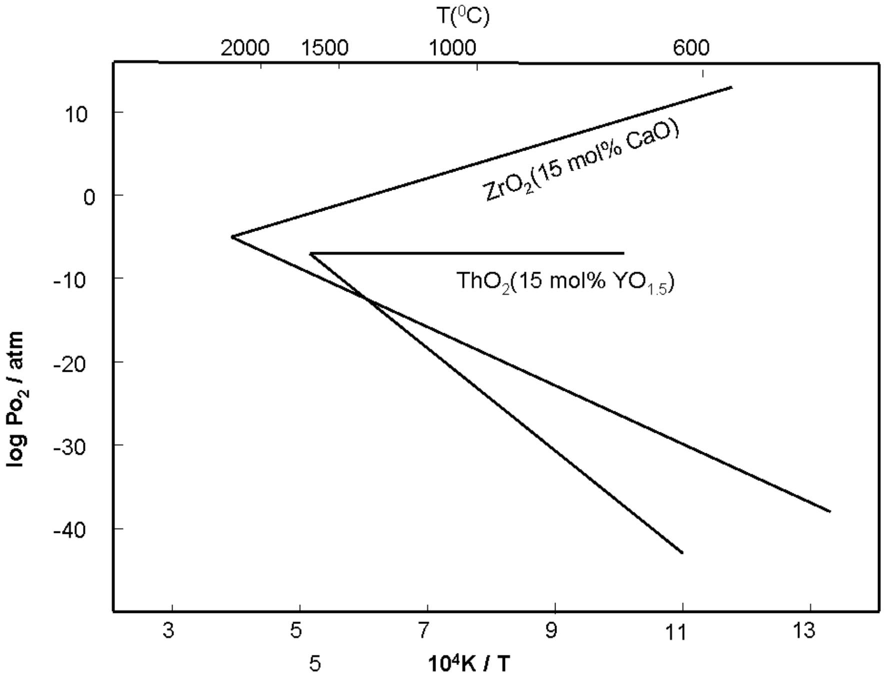

Fig. 2.10 Electrolytic domain boundary of calcia stabilized zirconia and yttria doped thoria

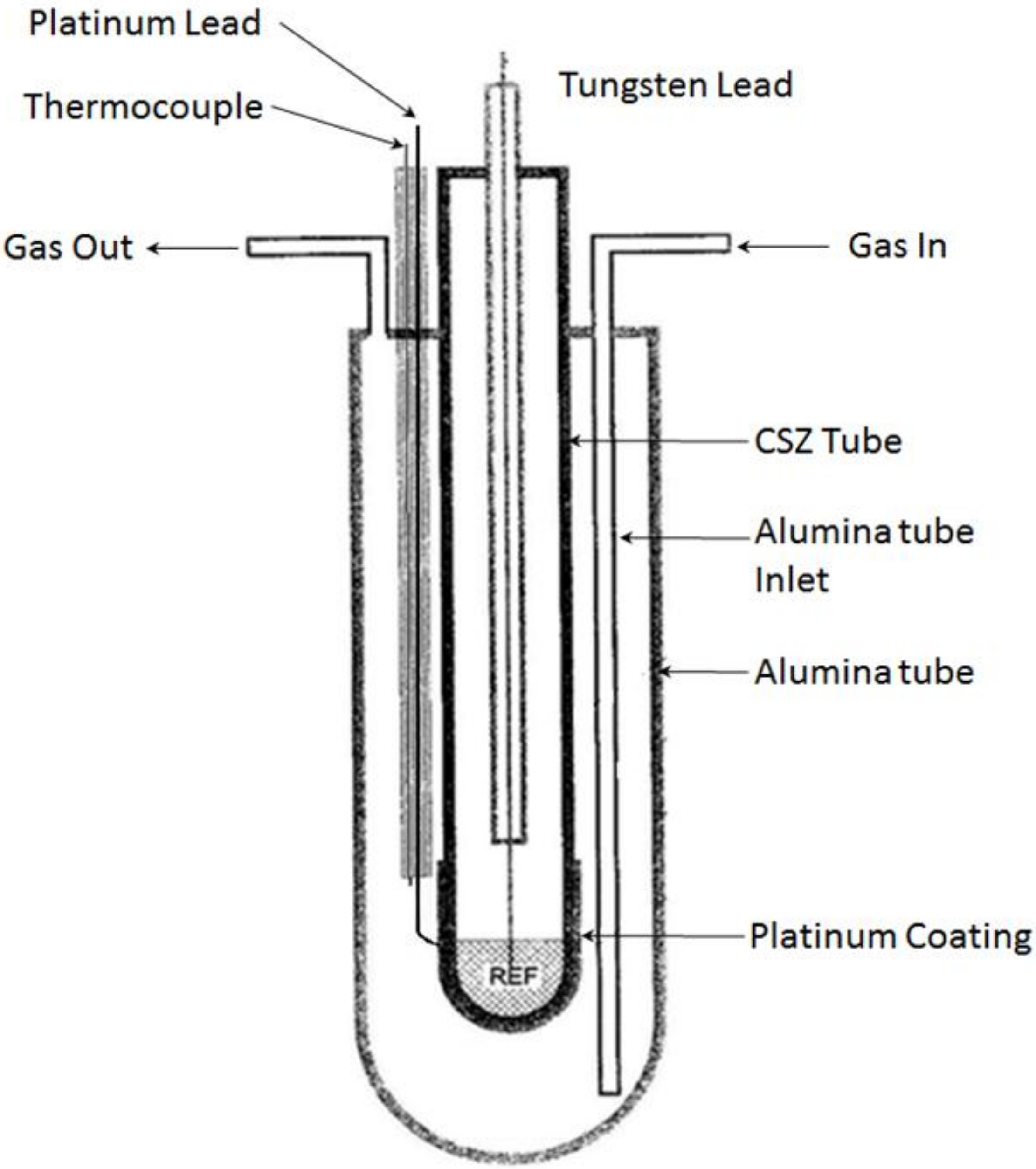

Fig. 2.11 A Schematic diagram of oxygen probe

2.2.11.1 Method of measurement

In a typical equilibration experiment the H_2-H_2O gas mixture of known oxygen potential (RT $\ln p_{o_2}$) was passed over the MOX pellets kept in an alumina boat in the uniform heating zone of resistance wire wound furnace (equilibration chamber). The oxygen potential of the gas exiting the equilibration chamber was continuously determined using an oxygen probe. The temperature of the furnace was controlled with in ± 2 K by using a PID controller. The MOX pellets were equilibrated to an oxygen potential of -350 kJ mol^{-1} at 1273 K. These samples were assumed to have attained a reference state of O/M = 2.000, because mixed oxide sample when equilibrated to oxygen potential of -330 and -360 kJ mol^{-1} at 1273 K did not change the weight of sample. After attaining the reference state of O/M = 2.000 weight of sample was taken using calibrated electronic balance with a sensitivity of ± 0.01 mg. The samples were then equilibrated to various oxygen potentials in the range of -560 kJ mol^{-1} to -300 kJ mol^{-1} at temperatures 1073 K, 1273 K and 1473 K. The time of equilibration varied from 10 h to 72 h depending on the temperature and final O/M value. After completion of equilibration sample pellets were weighed again. The O/M values of the equilibrated samples were calculated from the weight change with respect to the reference state using the following equation

$$O/M = 2 - x = 2 - \left[\frac{\Delta w}{W} \cdot \frac{M}{16}\right] \qquad (2.2)$$

where, W = sample weight at O/M = 2.000

M = molecular weight of $(U_{0.54}Pu_{0.46})O_{2.000}$

Δw = weight change relative to the stoichiometric sample weight

The oxygen potential of the gas at the outlet of equilibration chamber was monitored using an oxygen probe consisting of a CSZ solid electrolyte and In/In_2O_3 reference electrode.

The overall cell reaction can be written as,

$O_2 + 4e^- \rightarrow 2O^{2-}$ (2.3)

Hence, number of electrons participating in the cell reaction, n, is 4. The other electrode is the sample gas mixture. When the oxygen activity in one electrode is known, oxygen activity in the other electrode can be calculated from the measured EMF value, E between the two electrodes. The measured EMF is related to difference in oxygen activity of two electrodes by

$4FE = RT \ln p_{o_2} - RT \ln p'_{O_2}$ (2.4)

Where $RT \ln p'_{O_2}$ = oxygen potential of the sample

$RT \ln p_{o_2}$ = oxygen potential of the reference electrode

F = Faraday Constant

Oxygen potential of the reference electrode is obtained from the Gibbs energy data of In_2O_3 [14].

$RT\ ln p_{o_2} = \left(\frac{2}{3}\right) * \ \Delta_f G^o(In_2O_3)$ (2.5)

Hence, from the values of the E, the oxygen potential of the gas phase (and hence the oxygen potential of the MOX sample) was determined using equation (2.6).

$RT \ln p'_{O_2} = \left(\frac{2}{3}\right) * \ \Delta_f G^o(In_2O_3) - 4FE$ (2.6)

After the equilibration - as observed in the constancy of the value of EMF for at least 6 h - the sample was cooled rapidly to 873 K, thereafter, the equilibration gas mixture was replaced with ultra-high pure helium. The sample at room temperature was weighed and this weight was taken as the weight corresponding to the weight of the MOX pellets with an O/M = 2.000. Thereafter, the samples were equilibrated at the given oxygen potential at the desired temperature. When the equilibrium was achieved, the sample was cooled and weighed.

2.2.12 Experimental Assembly for EMF measurement

The experimental assembly used in the present study consists of an inert gas (helium) purification train, a furnace, an EMF cell assembly and a measuring instrument. Purified helium was used in all the experiments. Helium gas was purified by passing it through a purification train consisting of columns of regenerated LINDE 4A molecular sieves and active Cu impregnated in $MgSiO_3$ pellets (supplied by M/s. BASF India Ltd.) maintained at the ambient temperature followed by column containing metallic copper turnings held at 773 K, titanium sponge held at 1173 K and calcium metal shots held at 773 K. The gas exiting from the outlet of the EMF cell was again passed over another column containing calcium metal shots maintained at 773 K before letting it out to ambient air. Calcia stabilized zirconia (15CSZ) tube was used as the solid electrolyte and air, Pt was used as reference electrode for the EMF measurements. The CSZ tube has the dimensions: OD 12.7 mm, ID 9.5 mm and length 410 mm and has very high density (> 99 % theoretical density) to minimize open porosity or interconnected porosity. This tube isolates the test electrode from the reference electrode. For calcia stabilized zirconia solid electrolyte, operating partial pressure range (p_{O2}) extends from 10^{-18} bar (LEDB) to 10^5 bar (UEDB) [15]. K type thermocouple which was located in vicinity of galvanic cell which in turn was positioned in uniform heating zone of the furnace was used for temperature measurement. Air ($p_{O2} = 0.21$ atm) was used as reference electrode. To ensure good electrical contact annealed Pt lead wire (spot welded with Pt foil) was stuck with solid electrolyte tube using an adherent platinum paste in the inner compartment. Pt lead was encased in a single bore alumina tube. Pt foil was kept in good contact with CSZ tube using quartz tube. K type thermocouple was calibrated with already calibrated S type thermocouple. S type thermocouple was calibrated by measuring the melting points of Sn, Zn and Ag as per ITS-90 [6].

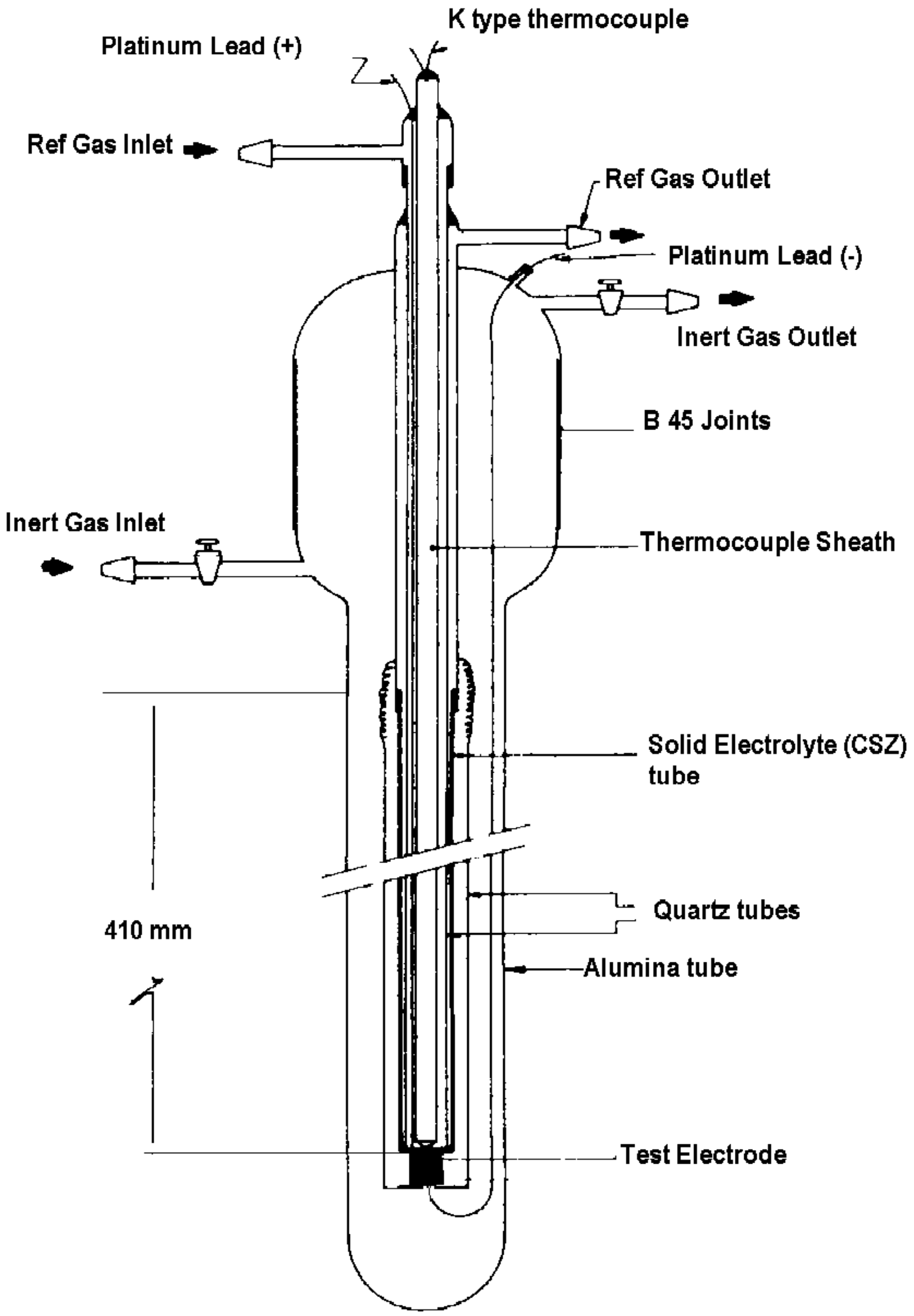

Fig. 2.12 Schematic of EMF assembly used in this study

The hot junction of K type thermocouple was positioned just above the CSZ tube in inner compartment. Similarly the test electrode was kept in good physical contact with CSZ tube using spring loaded quartz tube. Annealed Pt wire spot welded with Pt disc was routed through a fine hole in quartz tube from bottom electrode. Care was taken to ensure that reference electrode, CSZ tube flat end and test electrode were in uniform heating zone of furnace (Pt-10% rhodium alloy wire non-inductively wound on recrystallized alumina tube) so that no temperature gradient exists in the cell. A schematic of EMF assembly used in the present study is shown in Fig. 2.12.

2.3 Sample preparation for various measurements carried out in this study

2.3.1 Preparation of ternary compounds using solid state synthesis

The ternary oxides, used for determining thermodynamic properties were prepared by solid state reaction among the constituent oxides. This method is most widely used for the preparation of polycrystalline solids [16]. In this process, compacted pellets of a homogeneous mixture of constituent oxides (taken in the required mole ratio) are heated at a particular temperature for prolonged duration. The reaction involves three processes viz., transport of the reactants to the interface, reaction at the interface, transfer of the products away from the interface. Product formation is governed by thermodynamic and kinetic factors. Thermodynamic parameters show the feasibility of the reaction by taking into account the changes in Gibbs energy of the formation of the product from constituent reactants whereas kinetic factor determines the rate of the reaction. Because of sluggish nature of such solid state reactions, it is required to heat the reactants at high temperature. In normal solid state reactions, the reactants are mixed together manually or mechanically and hence the overall reaction rate depends upon the particle size of the reactants, the degree of homogenization achieved on mixing and the intimate contact between the grains. Intermittent grinding and pelletization is further carried out in order to break the diffusion barrier and to make intimate contact between the reactants. Detailed information regarding preparation of ternary oxides used in present work is given below.

2.3.1.1 Preparation of MOX $(U_{0.54}Pu_{0.46})O_2$

The MOX $(U_{0.54}Pu_{0.46})O_2$ pellets were made by conventional powder metallurgy route by mixing appropriate quantities of the two oxides (UO_2 and PuO_2) in a dry attrition mill, compacting and sintering the compacts at 1923 K for 4 h in N_2+7% H_2 atmosphere. The oxygen to metal ratio of the MOX pellets was fixed at 2.000 by equilibrating the compacts with H_2-H_2O gas mixture having an oxygen potential of -400 kJ mol^{-1} at 1273K.

2.3.1.2 Preparation of Cr_2TeO_6, $Cr_2Te_3O_9$ and $Cr_2Te_4O_{11}$

For the preparation of Cr_2TeO_6, component oxides Cr_2O_3 and TeO_2 were mixed in equimolar ratio and cold compacted into cylindrical pellets of 10 mm diameter and 2–3 mm thickness. These green compacts were subsequently heated in air at 873 K for 24 h, at 973 K for 12 h and then at 1073 K for 4 h. The pellets were withdrawn intermittently during the heat treatment from the furnace, powdered, re-compacted and then heat treated again. $Cr_2Te_3O_9$ and $Cr_2Te_4O_{11}$ were synthesized by heating compacts of mixtures of Cr_2O_3 and TeO_2 taken in mole ratio 1:3 and 1:4 respectively in vacuum sealed quartz ampoules at 873 K for 20 days.

2.3.1.3 Preparation of Fe_2TeO_6

The ternary oxide, Fe_2TeO_6 (s), was prepared by a solid state reaction between Fe_2O_3(s) and TeO_2(s) (equimolar mixture). The green compacts of this mixture were subsequently heated in air at 873 K for 12 h, at 973 K for 12 h and then at 1023 K for 4 h. This procedure was repeated twice to ensure that the reaction proceeds to completion.

2.3.1.4 Preparation of Ni_3TeO_6, $Ni_2Te_3O_8$ and $NiTe_2O_5$

The ternary oxides Ni_3TeO_6, $Ni_2Te_3O_8$ and $NiTe_2O_5$ were prepared by conventional solid state reaction between stoichiometric mixture of NiO and TeO_2. The green compacts (NiO: TeO_2 = 3:1) were subsequently heated in air at 873 K for 24 h and then at 1073 K for 24 h for the preparation of Ni_3TeO_6. The green compacts (NiO:TeO_2 = 1:2 and 2:3 respectively for the preparation of Ni Te_2O_5 and $Ni_2Te_3O_8$) were heated in ultra-high purity argon at 873 K for 12 h and then at 1053 K for 4 h for the preparation of $NiTe_2O_5$ and further at 1073 K for 2 h for the preparation of $Ni_2Te_3O_8$.

2.3.1.5 Sample Preparation for study of formation kinetics of La_2TeO_6

A homogeneous equimolar mixture of $La(OH)_3$ and TeO_2 was used as the sample in all the experiments carried out in this study. The samples were prepared and stored inside a glove box filled with high-purity argon in order to minimize absorption of moisture by $La(OH)_3$. This would, in turn, minimize the uncertainty in the initial weight of the sample. Approximately 20 mg of the sample was used in all the experiments. The variation in the quantity of the samples used in TG measurements was within ±40 μg. A fresh sample was used for each experiment. La_2TeO_6 was formed by a solid state reaction upon heating a homogeneous mixture of $La(OH)_3$ and TeO_2 (2:1 mole ratio) in a flowing stream of oxygen during the experiment.

2.3.2 Phase equilibration studies

Phase equilibration study is a static method of determining the attainment of the equilibrium state where the temperature of the sample is held constant until equilibrium is attained. Upon achievement of equilibrium, the specimen is quenched to ambient conditions which are achieved by rapid cooling in a bath of water or in liquid nitrogen. Its success depends upon the preservation of the phase assemblage present at equilibrium upon cooling to room temperature. The quenched specimens are characterized by XRD. This method has the virtue of experimental simplicity and straightforward interpretation.

Phase equilibration studies on Cr-Te-O system were carried out by this technique in order to establish ternary phase diagram and to obtain Gibbs energy of formation of ternary oxides in this system by EMF technique.

In Cr-Te-O system, three compounds i.e., Cr_2TeO_6, $Cr_2Te_3O_9$, $Cr_2Te_4O_{11}$ are reported in literature [17-19]. In order to explore the possibility of existence of any other ternary compound in the pseudo binary Cr_2O_3–TeO_2 system, compacts of Cr_2O_3 and TeO_2 corresponding to the molar ratios of 1:1, 1:2 and 1:5 were equilibrated at 923 K for 720 h in vacuum sealed quartz ampoules with one intermediate grinding and recompaction. The samples after equilibration were analyzed by XRD. In order to explore the possibility of the existence of ternary compounds other than Cr_2TeO_6in the pseudo binary of Cr_2O_3–TeO_3 system, compacts of Cr_2O_3 and TeO_2 in the molar ratio 1:2, 1:3 were heated at 873 K for 24 h, at 973 K for 24 h and then at 1173 K for 12 h.

For establishing different phase fields in Cr-Te-O system, the following mixtures of pure metals, oxides and the ternary compounds in weight ratio 1:1:1 with different overall compositions, were prepared by thorough grinding of the component phases and compacting them into pellets.

(1) Cr_2O_3(s), Te(s), Cr_2TeO_6(s)

(2) $Cr_2Te_3O_9$(s), Te(s), Cr_2TeO_6(s)

(3) $Cr_2Te_4O_{11}$(s),TeO_2(s),Cr_2TeO_6(s)

(4) $Cr_2Te_4O_{11}$(s), Te(s), $Cr_2Te_3O_9$(s)

(5) $Cr_2Te_4O_{11}$(s), $Cr_2Te_3O_9$(s), Cr_2TeO_6(s)

These compacts were taken in alumina crucibles and encapsulated in evacuated quartz ampoules. Each sample was first equilibrated at 923 K for a total period of 240 h after which it was quenched in liquid nitrogen. The products were thoroughly ground and characterised by XRD. They were recompacted and sealed under vacuum in quartz ampoules followed by equilibration at 923 K for another spell of 240 h.

2.4 Sample Characterization

2.4.1 Determination of Uranium and Plutonium

2.4.1.1 Wet Chemical Characterization Technique

In the present study U and Pu were estimated by different analytical procedures depending on the aliquot. Uranium in macro quantities was estimated by potentiometry using Davies & Gray method [20]. In this method an aliquot containing 3-5 mg/mL of uranium was analysed by redox procedure using mercury-mercurous sulphate as reference electrode and platinum as indicator electrode for end point detection. Plutonium in macro quantities was analysed by potentiometry using Drummond & Grant method [20] which involves the analysis of samples containing 3-5 mg/mL of plutonium. In both the methods, metal ions can be analysed to a precision of ± 0.5 % RSD.

2.4.1.2 XRD studies of MOX pellets

XRD of MOX $(U_{0.54}Pu_{0.46})O_2$ pellets was recorded in a specially designed aluminium holder (Fig. 2.13). Aluminium of the sample holder also served as an internal standard. The sample holder had a groove of 6 mm depth into which a cylindrical MOX pellet was placed vertically and in flush with the top of the opening. Para film® was used to cover the pellet and keep it in place. The shift in peak position of the sample due to possible height disposition (misalignment) was corrected using Al peak position. Corrected peak position values were used in calculating the lattice parameter of this solid solution. High angle reflections were used for the purpose of lattice parameter calculations. The plutonium composition was obtained by interpolating the lattice parameter value on a Vegard’s law plot [21-23].

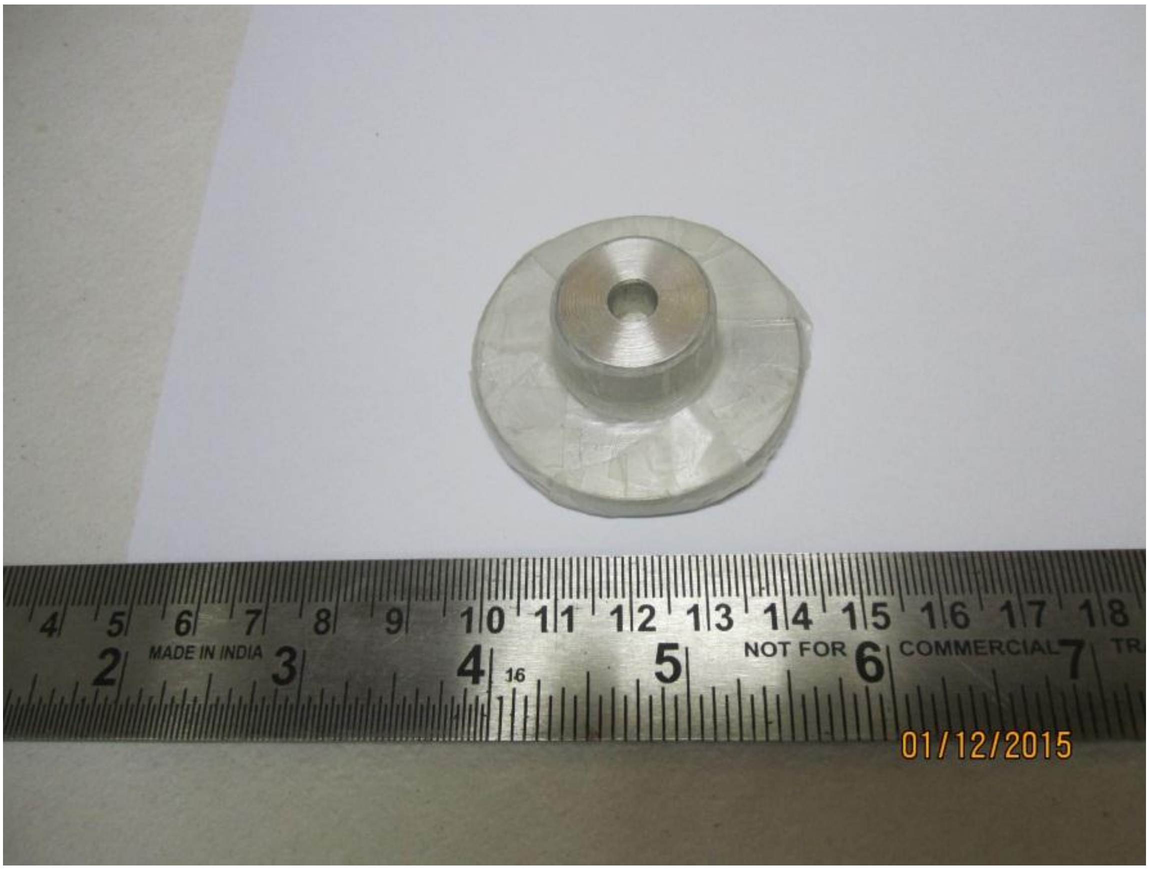

Fig. 2.13Aluminium sample holder for XRD

2.4.2 Phase identification

Phase identification of the compounds formed in the present study viz. Cr_2TeO_6, $Cr_2Te_3O_9$, $Cr_2Te_4O_{11}$, Fe_2TeO_6, Ni_3TeO_6, $Ni_2Te_3O_8$, $NiTe_2O_5$, La_2TeO_6 etc. was carried out from the XRD patterns of the respective samples. The 2θ values and intensities obtained are compared with that of the standard Joint Committee for Powder Diffraction Standards (JCPDS) files. In the present study, crystalline phase identification using XRD patterns was aided by the ICDD-PDF-2 database.

2.4.3 Determination of La and Te content

2.4.3.1 EDXRF studies

X-ray fluorescence studies were carried out to determine La and Te content of the products obtained after isothermal experiments carried out to study the kinetics of formation of lanthanum tellurate. The samples were excited using Rh K_α radiation (primary target) operated at 48 kV with a current of 1041 μA for a period of 300 s. Analyses were carried out using K_α lines of both Te (27.47 keV, 27.2 keV) and La (33.46 keV, 33.037 keV). La and Te contents in the samples were obtained using a calibration plot. For calibration plot, a number of standards containing Te and La were prepared by dissolving TeO_2 and $La(OH)_3$ in dilute H_2SO_4.

2.4.3.2 NAA studies

The sample, obtained after isothermal experiments to study the kinetics of formation of La_2TeO_6,were irradiated at a neutron flux of 6.5×10^{11} neutrons cm^{-2} s^{-1} for a period of 1h. The gamma lines corresponding to ^{131m}Te (150 keV) and ^{140}La (487 and 1596 keV) were used for the determination of La and Te content in the sample.

2.4.4 Electron microscopic analysis

The morphology of the product (powder) formed after formation reaction i.e. La_2TeO_6 was studied by using scanning electron microscopy (SEM). The sample was coated with Au-Pd to make it electrically conducting. The chemical composition of the sample was obtained by using energy-dispersive X-ray spectroscopy (EDS) facility attached with this instrument.

References

[1] Robinson J W. Undergraduate Instrumental analysis, 4th Ed., Marcel Dekker Inc, 1987, p371.

[2] Hamidatou L, Slamene H, Akhal T, Zouranen B. Concepts, Instrumentation and Techniques of Neutron Activation Analysis, Imaging and Radio analytical Techniques in Interdisciplinary Research – Fundamentals and Cutting Edge Applications, FaycalKharfi (Ed.), InTech, 2013, DOI: 10.5772/53686.

[3] Blažek A. Thermal Analysis, VNR Publishing Co., London, 1972, p19.

[4] West A R. Solid State Chemistry and its Applications, John Wiley & Sons, Singapore 2008.

[5] Speyer R F. Thermal Analysis of materials, Marcel Dekker Inc., New York, 1994, p35.

[6] Preston-Thomas H. The International Temperature Scale of 1990 (ITS-90). Metrologia 1990; 27(1): 3-10.

[7] Krishnaiah M V. Ph. D. Thesis, University of Madras, 1999.

[8] Babu R, Kandan R, Jena H, Kutty K V G, Nagarajan K. J Alloys Compd. 2010; 506: 565-68.

[9] Newbury D E, Joy D C, Echlen P, Fiori C E, Golestein J I. Advanced Scanning Electron Microscopy and X-ray Microanalysis, Plenum Press, New York (1986).

[10] Exner H E, Mills K, J. R. Davis J R, Dieterich D A (Eds) Metallography and Microstructure, ASM Handbook Vol. 9, International Soc. ASM., Materials Park, USA (1998).

[11] Kane P F, Larrabee G B. Characterization of Solid Surface, Plenum Press, New York, London, 1978, 107.

[12] Cullity B D. Elements of X-ray Diffraction, Addison–Wesley Publishing Co., Reading, Massachusetts, 1956.

[13] Whiston C. X-ray Methods, Analytical Chemistry by Open Learning, John Wiley & Sons, 1987.

[14] Knacke O, Kubaschewski O, Hesselmann K. Thermochemical Properties of Inorganic Substances. 2nd ed. Germany: Springer-Verlag (1991).

[15] Subba Rao E C. Solid Electrolyte and their Applications, Plenum Press, New York, 1980.

[16] Sahu S K, “Some Phase Equilibria and Thermochemical Studies on the Ternary Pb-Cr-O and Pb-Fe-O Systems” Ph.D. Thesis, University of Madras (2011).

[17] Kunnmann W, La Placa S, Corliss L M, Hastings J M, Banks E. Magnetic Structures of the ordered trirutiles Cr_2WO_6, Cr_2TeO_6 and Fe_2TeO_6. J Phys Chem Solids. 1968; 29: 1359-64.

[18] Bowden F L, Heveldt P F, Watson D J, Howell J A S, Wyeth P, Berry F J, Evans J, Clack D W, Davis R, McAuliffe C A, Johns D M. Inorganic Chemistry of the Transition Elements; RSC Publishing: Cambridge, U.K., 1978; Vol. 6.

[19] Meunier G, Frit B, Galy J. $Cr_2Te_4O_{11}$: une structure a anions complexes $(Cr_2O_{10})^{14-}$. ActaCryst. 1976; B32: 175-80.

[20] Gopinath N (2008) Chemical characterization of nuclear fuels. Tomar B S (Ed) IANCAS, 156-168.

[21] Truphémus T, Belin R C, Richaud J C, Reynaud M, Martinez M A, Félines I, Arredondo A, Miard A, Dubois T, Adenot F, Rogez J. Structural studies of the phase separation in the UO_2-PuO_2-Pu_2O_3 ternary system. J Nucl Mater. 2012; 432: 378-87.

[22] Kato M, Konashi K. Lattice parameters of (U, Pu, Am, Np)O_{2-x}. J Nucl Mater. 2009; 385: 117-121.

[23] Grandjean S, Arab-Chapelet B, Robisson A C, Abraham F, Martin P, Dancausse J P, Herlet N, Léorier C. Structure of mixed U(IV)–An(III) precursors synthesized by co-conversion methods (where An = Pu, Am or Cm). J Nucl Mater. 2009; 385: 204-207.

Chapter 3

Measurement of oxygen potential of urania-plutonia solid solution $(U_{0.54}Pu_{0.46})O_{2-x}$

3

3.1 Introduction

Several investigators have measured the chemical potential of oxygen in Pu bearing MOX fuels [1-15]. The composition over which the investigations have been made and the temperature range of validity of the data are given in Table 3.1. It can be seen from the table that there are no experimental data on the oxygen potential of plutonium bearing MOX with Pu/Pu+U > 0.4. In this study the chemical potential of oxygen in unirradiated MOX pellets having Pu/(U+Pu) = 0.46 has been measured using gas equilibration coupled with EMF measurement technique. The measurements were made over the temperature range 1073 to 1473 K and O/M = 1.98 to 2.00. This will help in understanding of the many physicochemical properties of the fuel as well as to understand U-Pu-O system completely.

Table 3.1 The details of composition, temperature range and technique of $(U_{1-y}Pu_y)O_{2\pm x}$ for which oxygen potential data are available in literature

Value of y in $(U_{1-y}Pu_y)O_{2\pm x}$	O/M ratio (2±x)	Temperature range (K)	Technique	Reference
0.21 and 0.28	1.97 to 2.00	1073 to 1473	Gas equilibration / EMF	Vasudeva Rao et al. [1]
0.3	1.98 to 2.00	1273 to 1623	TG-DTA	Kato et al. [2]
0.2	1.99 to 2.00	1473 to 1623	TG-DTA	Kato et al. [3]
0.12	1.9881 to 2.0408	1673 to 1873	TG-DTA	Kato et al. [4]
0.3	1.9637 to 2.0288	1773 to 1873	TG-DTA	Kato et al. [4]

0.11 and 0.30	1.87 to 2.08	1023 to 1373	Thermogravimetry	Markin and McIver [5]
0.25	1.9 to 2.00	1223 to 1673	Thermogravimetry	Woodley [6]
0.1 and 0.4	1.9 to 2.0	1273 to 1473	Thermogravimetry and EMF	Woodley [7]
0.25	1.94 to 2.028	1073 to 1273	Thermogravimetry and EMF	Woodley and Adamson [8]
0.1 and 0.2	1.99 to 1.999	1273 to 1723	Thermogravimetry	Sorenson [9]
0.23 and 0.15	1.9984 to 2.00	1523 to 1823	Thermogravimetry	Edwards et al. [10]
0.23	1.995 to 2.02	1523 to 1823	Thermogravimetry	Chilton et al. [11]
0.31	1.995 to 2.05	1815		
0.15 and 0.31	Hyperstoichiometry	1518, 1623 and 1823	Transpiration	Chilton and Kirkham [12]
0.2	1.92 to 1.98	2150 to 2550	Transpiration	Tetenbaum [13]
0.2	1.92 to 1.98	1273 to 1973	Gas equilibration and chemical analyses	Javed [14,15]

3.2 Oxygen potential of $(U_{0.54}Pu_{0.46})O_{2-x}$ solid solution

3.2.1 Gas mixtures for equilibration

Table 3.2 shows the range of oxygen potentials of the gas mixtures employed in the present study. In order to carry out measurements at very low oxygen potentials (less than -470 kJ mol^{-1}) at temperatures 1073 to 1473 K, H_2-H_2O gas mixtures were obtained by passing pure H_2 gas through a saturated LiCl – H_2O bath maintained at different temperatures. The water vapour pressure of the resultant gas mixture is given by Nevzat A. Gokcen [16] as,

$$\ln pH_2O/\text{ mm Hg} = -6212.96/T + 21.784 \text{ where T is in K} \qquad (3.1)$$

The saturated water vapour pressure over pure liquid water column is given by equation (3.2)

$$\ln pH_2O/\text{ mm Hg} = -5132/T + 20.386 \text{ where T is in K} \qquad (3.2)$$

The Gibbs energy of formation of water is given in Ref. [17] as,

$$\Delta_f G^o_{H_2O} = -246.44+0.0548T \qquad (3.3)$$

Table 3.3 shows the oxygen potential of H_2-H_2O gas mixture obtained by passing H_2 gas through a column containing saturated LiCl - H_2O bath.

Table 3.2 The gas mixtures employed in the present study for the oxygen potential measurements

Oxygen Potential (kJ/mol.)	Gas mixtures employed
-550 to -470	H_2 gas passed through a column containing saturated LiCl – H_2O bath at 253 – 298 K
-465 to -400	H_2 gas passed through a water column maintained at 273 - 333 K
-400 to -350	Argon-8% H_2 passed through a water column maintained at 278 - 300 K
-360 to -325	Argon-4% H_2 passed through a water column maintained at 295 - 310 K

Table 3.3 Oxygen potential of the gas mixture H_2-H_2O obtained by passing H_2 gas through a column containing saturated LiCl - H_2O bath

Temp. / K	pH_2O/ mm Hg	pH_2O/pH_2	$\Delta\mu_{O2}$ / kJ mol^{-1}		
			1073 K	1273 K	1473 K
253	0.062	8.22E-5	-543.1	-552.5	-561.8
268	0.247	3.25E-4	-518.6	-523.4	-528.2
278	0.568	7.49E-4	-503.7	-505.7	-507.7
298	2.548	3.36E-3	-476.9	-473.9	-470.9

In order to carry out measurements at oxygen potentials varying from -465 to -325 kJ mol^{-1} at temperatures 1073 to 1473 K, the required ratio of H_2-H_2O gas mixture was obtained by passing either pure hydrogen or argon-hydrogen gas mixtures through a refrigerated water bath maintained at 278 to 323 K. Table 3.4 shows the oxygen potentials of gas mixtures obtained by passing H_2 or pre-mixed Ar-H_2 gas mixture through a water column maintained at various temperatures.

Table 3.4 Oxygen potentials of H_2-H_2O gas mixtures

T/K of water column	pH_2O /mm Hg	Pure H_2 bubbled through water column				Argon – 8 % H_2 bubbled through water column				Argon – 4% H_2 bubbled through water column			
		pH_2O/pH_2	$\Delta\bar{G}_{O_2}$/ kJ mol.$^{-1}$			pH_2O/pH_2	$\Delta\bar{G}_{O_2}$/ kJ mol.$^{-1}$			pH_2O/pH_2	$\Delta\bar{G}_{O_2}$/ kJ mol.$^{-1}$		
			1073 K	1273 K	1473 K		1073 K	1273 K	1473 K		1073 K	1273 K	1473 K
278	6.86	0.0091	-459.1	-452.8	-446.5	0.1138	-414.0	-399.4	-384.7	0.2277	-401.7	-384.7	-367.7
298	23.68	0.0322	-436.6	-426.1	-415.6	0.4020	-391.5	-372.7	-353.8	0.8039	-379.2	-358.0	-336.8
313	54.05	0.0766	-421.1	-407.8	-394.4	0.9570	-376.1	-354.3	-332.5	1.9139	-363.7	-339.6	-315.5
323	89.79	0.1340	-411.1	-395.9	-380.7	1.6746	-366.1	-342.4	-318.8	3.3493	-353.7	-327.8	-301.8

3.2.2 Errors in measurement

The experimental quantities measured in the present study are i) EMF of the oxygen probe E, ii) equilibration temperature T and iii) the weight change associated with change in oxygen potential. From the values of E, the oxygen potential of the gas phase exiting from the equilibration chamber was determined by using equation (2.6).

Taking differentials of Eq. (2.6),

$$d\left(\Delta\mu_{O_2}\right)_{sample} \leq \left(\frac{2}{3}\right) * \left[d\Delta_f G^o(In_2O_3)\right]_T + \left(\frac{2}{3}\right) * \left[\frac{d\Delta_f G^o(In_2O_3)}{dT}\right] dT + 4F(\Delta E)_T + 4F\left(\frac{dE}{dT}\right) dT \qquad (3.4)$$

The first two terms on the right hand side of Eq. (3.6) denote systematic errors, while other two terms denote random errors. The uncertainty in the measurement of EMF is ± 1% (based on repeated measurements using standard mixtures). The uncertainty in temperature measurement is ± 2 K for each individual point. At the temperatures of measurement these uncertainties lead to an overall error of ± 2 kJ mol^{-1}. The accuracy in measurement of weight is ~10 μg. From the accuracy and precision of the weight measurements, the cumulative error in weight measurements is ± 100 μg. This corresponds to a maximum error of ± 0.001 in O/M.

3.3 Sample Characterization

3.3.1 Phase Characterization

XRD of MOX pellets was recorded in a specially designed aluminium holder. Typical XRD pattern of the U, Pu mixed oxide pellet with Pu/(U+Pu) ~ 0.46 is shown in Fig. 3.1. The aluminum peaks are not shown because the intensity of the peaks corresponding to the aluminum sample holder were very high and masked the pattern for the MOX samples. A pattern of the (U, Pu) mixed oxide with Pu/(U+Pu) = 0.21 is also shown for the purpose of comparison. Both the patterns show that the MOX pellets are single phasic and homogenous. Studies in the literature [18-21] report that stoichiometric MOX containing Pu even in excess of 15 mole percent are single phasic. This means the MOX samples used in this study were stoichiometric to start with and the lattice parameter calculated is influenced by only uranium and plutonium content. The lattice parameter of the sample (5.439 A°) corresponded to a plutonium composition of 42.5 ± 2 % of (U+Pu).

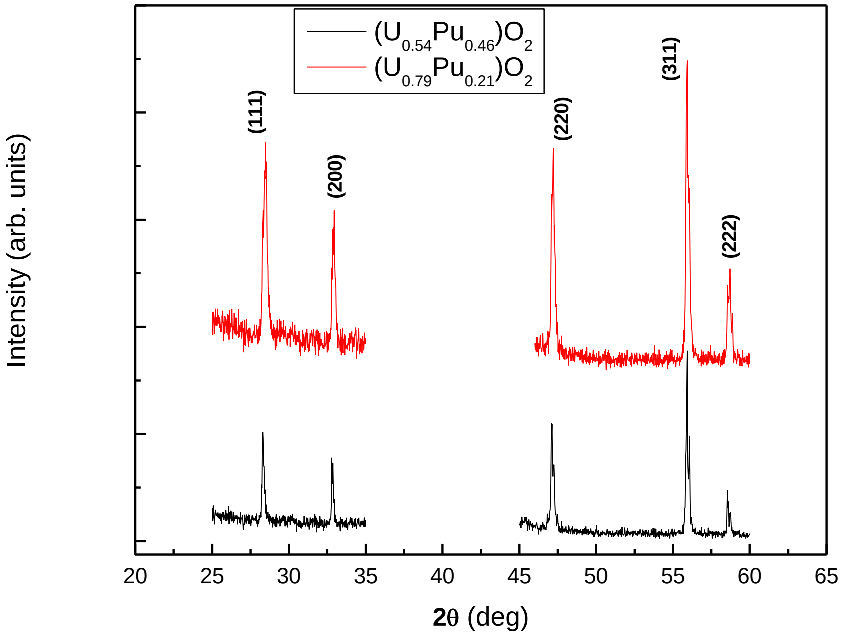

Fig. 3.1 Typical XRD patterns of $(U_{0.54}Pu_{0.46})O_2$ and $(U_{0.79}Pu_{0.21})O_2$ (peaks corresponding to the aluminum sample holder not shown for clarity)

3.3.2 Analysis of uranium and plutonium

Uranium and plutonium composition in MOX pellet was obtained using Davies & Gray method and Drummond & Grant method respectively. The composition was found to be 46 ± 0.3 % for plutonium and 54 ± 0.5 % uranium in the MOX based upon wet chemical technique using above mentioned methods. This value is higher than that determined using XRD technique. Relying on the more accurate chemical method the final composition for MOX was taken to be $(U_{0.54}Pu_{0.46})O_{2-x}$.

3.4 Oxygen Potential of MOX sample

The values of the oxygen potential of $(U_{0.54}Pu_{0.46})O_{2-x}$ obtained in present study at different O/M values and at temperatures 1073 K, 1273 K and 1473 K are given in Table 3.5. These values are plotted as a function of O/M in Fig. 3.2. A comparison between oxygen potential values obtained in present study for Pu/(U+Pu) = 0.46 and that of from Woodley et al. [7] for Pu/(U+Pu) = 0.4 is also plotted in Fig. 3.3.

Table 3.5 The values of the oxygen potential obtained in this study

1073 K		1273 K		1473 K	
O/M	$\Delta\overline{G_{O_2}}$ (kJ mol^{-1})	O/M	$\Delta\overline{G_{O_2}}$ (kJ mol^{-1})	O/M	$\Delta\overline{G_{O_2}}$ (kJ mol^{-1})
2.0	-365.9	2.0	-332.1	1.999	-325.5
2.0	-382.3	2.0	-342.1	1.998	-345.1
2.0	-388.2	2.0	-359.0	1.997	-373.0
1.999	-458.4	1.999	-389.1	1.993	-404.0
1.998	-465.9	1.996	-430.1	1.987	-441.0
1.993	-496.3	1.995	-434.3		
1.992	-502.0	1.989	-475.2		
1.990	-512.6				

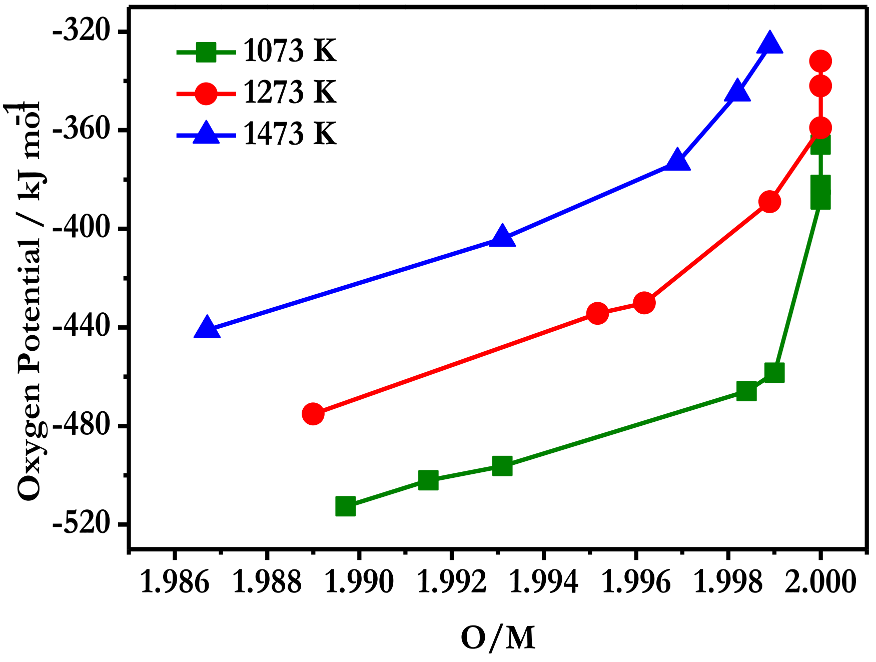

Fig. 3.2 Oxygen potential of $(U_{0.54}Pu_{0.46})O_{2-x}$ as a function of O/M at temperatures 1073 K, 1273 K and 1473 K

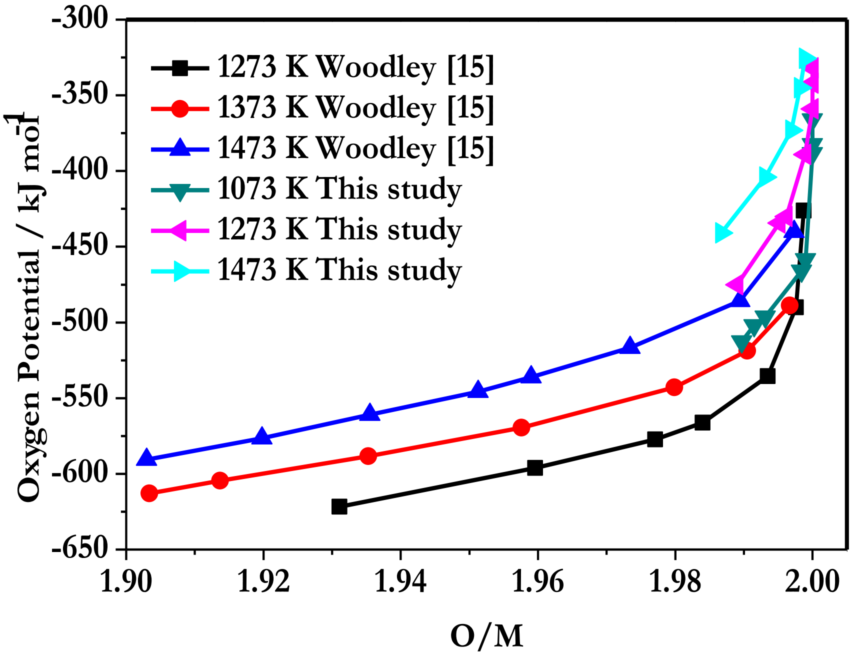

Fig. 3.3 A comparison of oxygen potential values obtained in present study [Pu/(U+Pu) = 0.46] and Ref. [15] [Pu/(U+Pu) = 0.4]

It is observed that the oxygen potential obtained in this study at a given O/M for a given temperature is higher by about 75 kJ (e.g. at an O/M of 1.99 and at 1473 K). This is as expected as the oxygen potential increases with increase in plutonium content. In addition, the minimum O/M that could be obtained in this study was only 1.985 as compared to 1.905 obtained by Woodley [7]. Hence, the experiment was repeated with new set of pellets from a different lot. Still the reduction could not be carried out below an O/M of 1.985. Experiments were also carried out to equilibrate the pellets at 1473 K for 240 h in atmosphere having an oxygen potential of -550 kJ/mol to rule out the possibility of very slow reduction kinetics. This also did not yield reduction in O/M. Another experiment was tried with oxidation of the pellets to the hyper stoichiometric values and reduction thereafter to the required O/M. While the pellets were readily oxidized, subsequent reduction below an O/M = 1.985 did not occur. MOX containing Pu in excess of 15 mol.% was found to segregate into two phases in the hypo region of the oxygen composition (reduction carried out by equilibrating in a stream of hydrogen gas of known oxygen potential at temperatures between 1673 to 2273 K, annealed at 473 K and cooled to room temperature) [18]. Other studies [19-21] report that for plutonium contents above 20% of total metal, at room temperature the mixed oxides are polyphasic and the UO_2-PuO_2-Pu_2O_3 sub-system exhibits a miscibility gap. For 20%<Pu%<45% the miscibility gap is composed of two hypostoichiometric phases – one a fcc phase with a slightly higher oxygen containing phase (with an O/M close to 2.00) and the other - also fcc- but with lower oxygen containing phase (more reduced). The relative amounts of the two phases depend on the plutonium content and temperature. For Pu/(U+Pu) = 0.46, at 300 K the resulting O/M observed was 1.955 only [22]. The temperature at which the phase separation occurs depends on the O/M for given plutonium content. The resistance to reduction in O/M observed in this study suggests that perhaps one of the fcc phases segregated (with an O/M close to 2.00) inhibits further reduction.

Further, Truphemus et al. [20, 21] report that on processing a sintered pellet under reducing conditions, the phase separation induces micro cracks. This indicates that formation of micro cracks would expose fresh surface and thereby facilitate the completion of the reduction. In the present study, neither micro-cracks were visible nor reduction below an O/M of 1.985 occurred.

In order to compare the chemical potentials obtained in this study for 46 mol.% Pu with those from literature)., the data obtained were fitted to the equation (3.5).

$$\ln p_{O_2} = n \ln(Pu^{+4}/Pu^{+3}) + \ln K = \Delta\mu_{O_2}/RT \qquad (3.5)$$

where $Pu^{+4}/Pu^{+3} = ((y-2x)/2x)$ where y is Pu content in $(U_{1-y}Pu_y)O_{2\pm x}$ and x is the extent of non-stoichiometry. Plots of $\ln p_{O_2}$ as a function of $\ln(Pu^{+4}/ Pu^{+3})$ for 1273 K and 1473 K are shown in Figs. 3.4 and 3.5. The values of oxygen potential for MOX containing Pu/(U+Pu) = 0.46 as a function of O/M, at 1073, 1273 and 1473 K, were calculated using Thermo-Calc software and the data set given in Ref. [23]. This was compared with the data obtained in the present study (Fig. 3.6). The experimental data shows similar trend as the calculated data. At 1473 K, it is seen that the experimental data agrees with the calculated data within experimental uncertainties, however, the experimental data shows a larger deviation from the calculated data at lower temperatures.

The data obtained in this work shows similar increasing trend as reported by earlier studies. Considering that the data of oxygen potential for different compositions were taken from entirely different work the data agrees well. The data shown in Figs. 3.4 and 3.5 match better with that reported by Vasudeva Rao et al. [1] for 0.28 mol. % plutonium bearing MOX.

Partial molar enthalpy can be calculated from the oxygen potential data by using

$$\Delta\overline{G_{O_2}} = \Delta\overline{H_{O_2}} - T\Delta\overline{S_{O_2}} \tag{3.6}$$

In Fig. 3.7 $\Delta\overline{G_{O_2}}$ obtained in this study is plotted as a function of temperature for various O/M ratios between 1.990 to 1.999. The oxygen potential increases with O/M obviously. The partial molar enthalpy is obtained from the y-intercept and the partial molar entropy is the slope and the values obtained thus are -752.36 kJ mol^{-1} and 0.25 kJ mol^{-1} K^{-1} respectively. The values gradually increase with increasing O/M and near stoichiometry a small jump (30 kJ mol^{-1}) is observed. Kato et al. [3] reported a value of ~ -900 kJ mol^{-1} for the partial molar enthalpy at an O/M near stoichiometry for a plutonium composition of 20%. For MOX containing 30 mol.% plutonium the enthalpy increases to ~ -750 kJ mol^{-1}. This increasing trend in the value agrees well with that reported in this study.

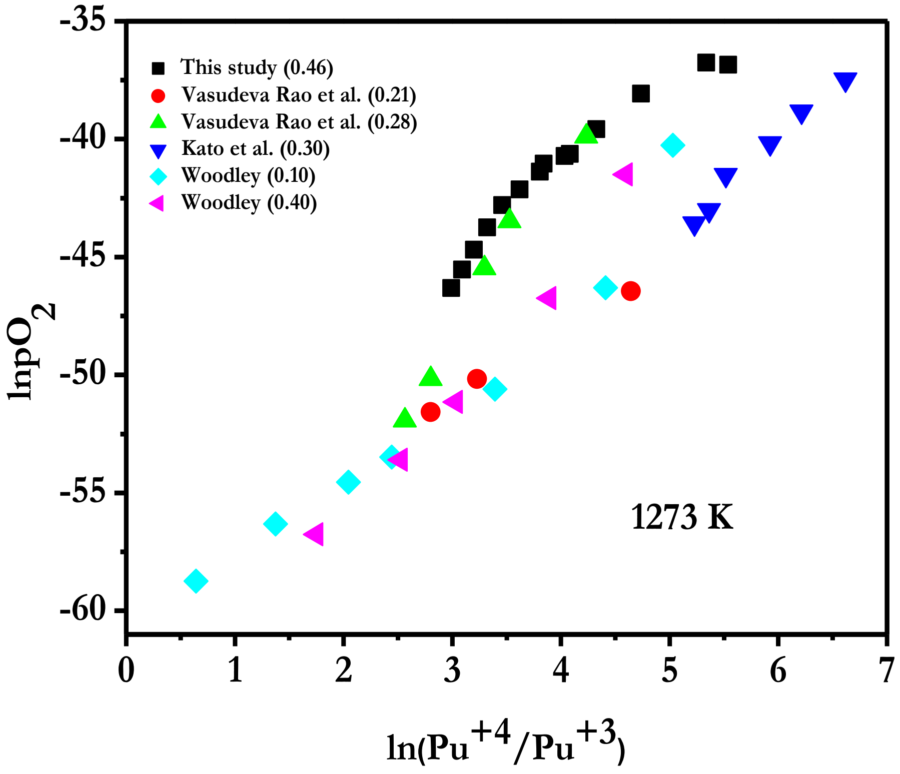

Fig. 3.4 Comparison of oxygen potential values at 1273 K with literature values

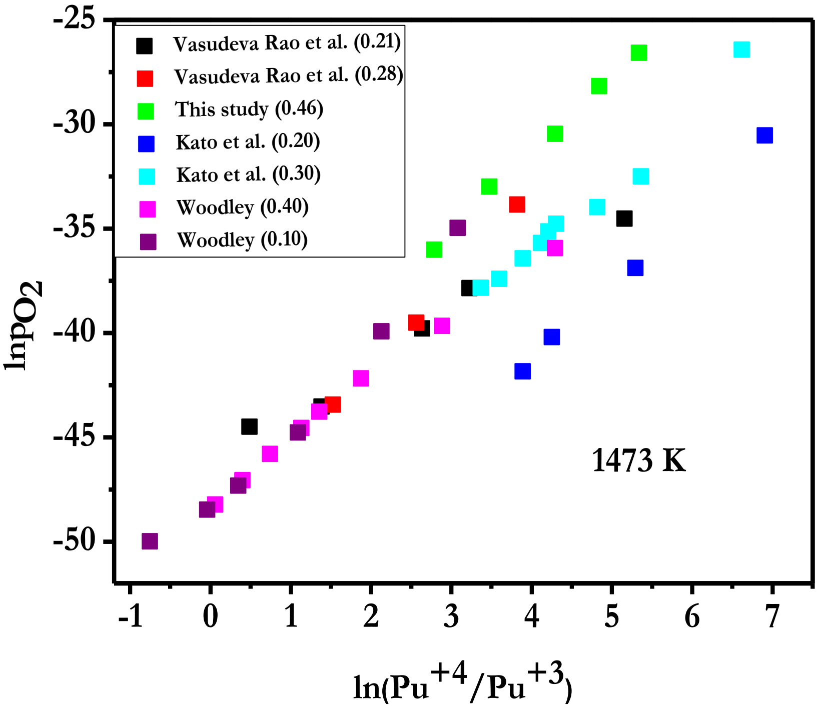

Fig. 3.5 Comparison of oxygen potential data at 1473 K with those reported in literature

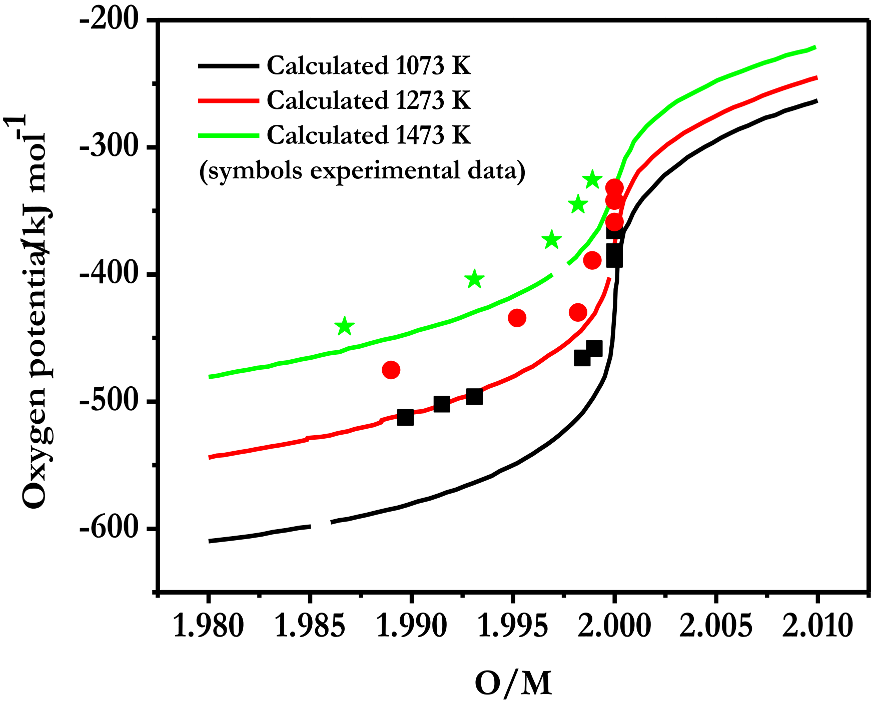

Fig. 3.6 Comparison of the experimental oxygen potential with the calculated data

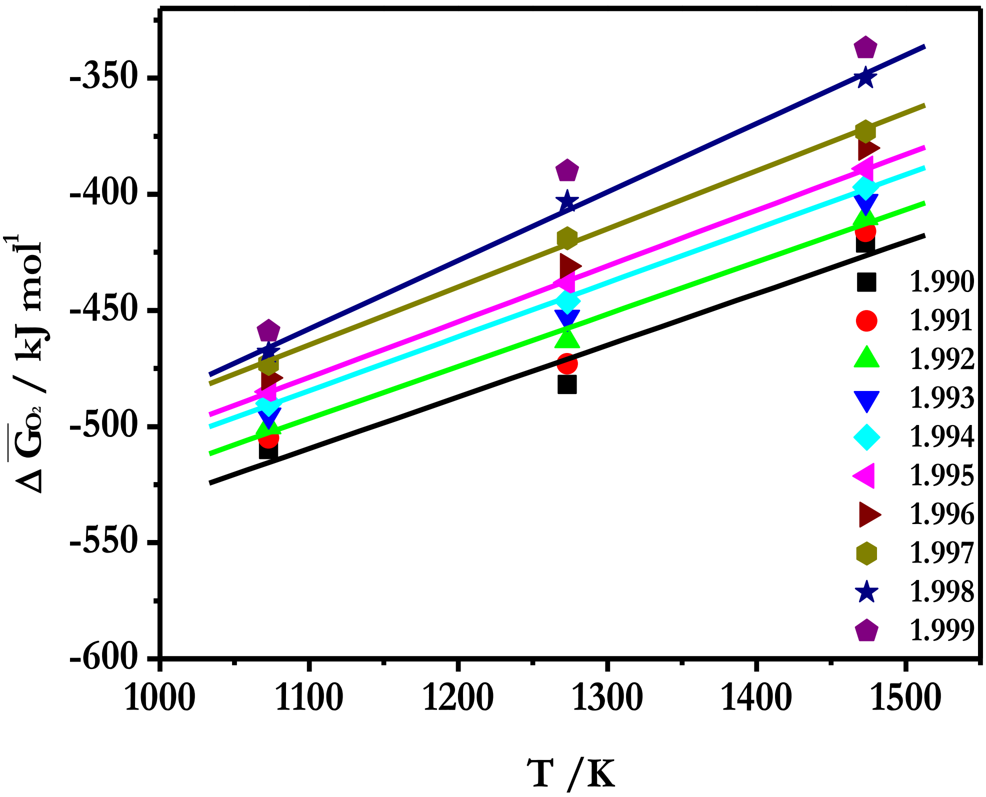

Fig. 3.7 Variation of oxygen potential with temperature and O/M

3.5 Conclusions

The chemical potential of oxygen in MOX containing 46 mol.% plutonium was determined for the first time using a gas equilibration technique. The trend of the data is in agreement with that of Kato et al. and Vasudeva Rao et al. In this study, the (U,Pu) mixed oxide with (U/(U+Pu)) = 0.46 could not be reduced below an O/M of 1.985.

References

[1] Vasudeva Rao P R, Anthonysamy S, Krishnaiah M V, Chandramouli V. Oxygen potential and thermal conductivity of (U, Pu) mixed oxides. J Nucl Mater. 2006 ; 348 : 329-34.

[2] Kato M, Tamura T, Konashi K, Aono S. Oxygen potentials of plutonium and uranium mixed oxide. J Nucl Mater. 2005; 344: 235-39.

[3] Kato M, Tamura T, Konashi K. Oxygen potentials of mixed oxide fuels for fast reactors. J Nucl Mater. 2009; 385: 419-23.

[4] Kato M, Takeuchi K, Uchida T, Sunaoshi T, Konashi K. Oxygen potential of $(U_{0.88}\ Pu_{0.12})O_{2\pm x}$ and $(U_{0.7}Pu_{0.3})O_{2\pm x}$ at high temperatures of 1673–1873 K. J Nucl Mater. 2011; 414: 120-25.

[5] Markin T L, McIver E J. Plutonium 1965. Kay E K, Waldron W B (eds.) Chapman and Hall, London, 1967, p 845-57.

[6] Woodley R E. Equilibrium Oxygen Potential-Composition Relations in $U_{0.75}Pu_{0.25}O_{2-x}$. J Am Ceram Soc. 1973; 56: 116-19.

[7] Woodley R E. Oxygen potentials of plutonia and urania-plutonia solid solutions.

J Nucl Mater. 1981; 96: 5-14.

[8] Woodley R E, Adamson M G. The oxygen potential of near and non-stoichiometric urania-25 mol% plutonia solid solutions: A comparison of thermogravimetric and galvanic cell measurements. J Nucl Mater. 1979; 82: 65-75.

[9] Sorenson O T. Plutonium 1975 and other Actinides, Blank H, Lindner R (eds.) North-Holland, Amsterdam, 1976, p 123-31.

[10] Edwards J, Wood R N, Chilton G R. Oxygen potentials of uranium-plutonium oxides in the near stoichiometric region. J Nucl Mater. 1985; 130: 505-12.

[11] Chilton G R, Edwards J. Intern Symp Thermodyn Nucl Mater. Jülich, IAEA-SM-236/43, 1979; 1: 357-68.

[12] Chilton G R, Kirkham I A. The Determination of Oxygen Potentials of hyperstoichiometric U-Pu dioxides in the temperature Range 1500 – 1800K, Plutonium 1975, North-Holland, Amsterdam, 1976, p 171-180.

[13] Tetenbaum M, Thermodynamics of Nuclear Materials 1974, in; Proc. Symp., IAEA, Vienna, 1974: 2; 305.

[14] Javed N A, Roberts J T A. Thermodynamic and defect-structure studies in mixed-oxide fuels. Report ANL-7901, 1972, p 1-22.

[15] Javed N A. Thermodynamic behavior of (U, Pu) mixed-oxide fuels. J Nucl Mater. 1973; 47: 336-44.

[16] Gokcen N. Vapor Pressure of Water above Saturated Lithium Chloride Solution. J Am Chem Soc. 1951; 73: 3789-90.

[17] Kubaschewski O, Alcock C B, Metallurgical Thermochemistry, fifth ed., Pergamon, 1979.

[18] Sari C, Benedict U, Blank H. A study of the ternary system UO_2-PuO_2-Pu_2O_3. J Nucl Mater. 1970 ; 35 : 267-77.

[19] Vauchy R, Belin R C, Robisson A C, Hodaj F. High temperature X-ray diffraction study of the kinetics of phase separation in hypostoichiometric uranium–plutonium mixed oxides. J Euro Ceram Soc. 2014; 34 : 2543-51.

[20] Truphemus T, Belin R C, Richaud J C, Rogez J. Phase equilibria in the uranium-plutonium-oxygen ternary phase diagram at $(U_{0.55},Pu_{0.45})O_{2-x}$ and $(U_{0.45},Pu_{0.55})O_{2-x}$ Proc Chem. 2012; 7: 521-27.

[21] Truphemus T, Belin R C, Richaud J C, Reynaud M, Martinez M A, Felines I. Structural studies of the phase separation in the UO_2–PuO_2–Pu_2O_3 ternary system. J Nucl Mater. 2013; 432: 378-87.

[22] Belin R C, Strach M, Thibaut T, Gueneau C, Richaud J, Rogez J. In situ high temperature X-Ray diffraction study of the phase equilibria in the UO_2–PuO_2–Pu_2O_3 system. J Nucl Mater. 2015; 465: 407-17.

[23] Gueneau C, Dupin N, Sundman B, Martial C, Dumas J C, Gosse S, Chatain S, Bruycker F D, Manara D, Konings R J M. Thermodynamic modelling of advanced oxide and carbide nuclear fuels: Description of the U–Pu–O–C systems. J Nucl Mater. 2011; 419: 145-67.

Chapter 4

Thermodynamic stability of Cr_2TeO_6, Fe_2TeO_6, Ni_3TeO_6 by transpiration technique

4

4.1 Introduction

Data on the thermodynamic properties of the compounds that could be formed by the possible interactions between fuel, fission products and the constituents of the clad and coolant are required in evaluating the performance of (U, Pu) mixed oxides as fuels for fast breeder reactors. One of the reactive fission products formed during the burn up of the fuel is tellurium which causes embrittlement in stainless steel [1-4]. In order to predict the integrity of the fuel pins, data on the thermodynamic stability of the compounds of tellurium with clad components such as Fe, Cr, Ni, Ti etc. are required. However thermochemical information on these compounds is rather scant [5-9]. Hence an experimental programme has been pursued in order to generate thermochemical data on the multicomponent oxide systems involving tellurium and one of the elements of the clad material.

In the present study experiments were carried out to measure the vapour pressure of TeO_2 (g) over the phase mixtures (i) Cr_2O_3 (s) + Cr_2TeO_6 (s) (ii) Fe_2O_3 (s) + Fe_2TeO_6 (s) (iii) NiO (s) + Ni_3TeO_6 (s) by the transpiration technique using a thermal analyzer. From the measured vapour pressure of TeO_2 (g), the standard Gibbs energy of formation of Cr_2TeO_6, Fe_2TeO_6 and Ni_3TeO_6 were determined over the temperature range 1183 - 1293 K, 1103 - 1203 K and 1143 - 1272 K respectively.

Krishnan et al. [5] have measured ΔG_f^o (Cr_2TeO_6, s) over the temperature range 1014 - 1100 K by Knudsen cell effusion method. In the present study standard Gibbs energy of formation of Cr_2TeO_6 has been determined using transpiration technique and the results are reported for the first time. There are two reports on standard Gibbs energy of formation of Fe_2TeO_6 which include measurement by Krishnan et al. [5] using Knudsen effusion mass loss technique and Sahu et al. [10] by transpiration technique over the temperature range 979 – 1052 K and 949 – 1053 K respectively. There is a difference of 24.9 kJ mol^{-1} in the values of ΔG_f^o (Fe_2TeO_6, s, 1000 K) calculated from these two reports. The difference of 24.9 kJ mol^{-1} between two measurements is considered to be high as reported by Sahu et al. [10].

There are many reports on standard Gibbs energy of formation of Ni_3TeO_6 [7, 8, 10, 11]. These include measurements by Mallika et al. [11] by EMF technique in the temperature range 624-964 K, Ali et al. [7] by transpiration technique in the temperature range 1122-1202 K, Krishnan et al. [8] by Knudsen Effusion Mass Loss technique in the temperature range 1042-1129 K and Sahu et al. [10] by transpiration technique in the temperature range 942-1059 K. There is large discrepancy in the values of standard Gibb's energy of formation of Ni_3TeO_6. For example, at 1000 K the variation in ΔG_f^o is 68.4 kJ mol^{-1} between the measurements by Mallika et al. [11] and Krishnan et al. [8]. Because of this large discrepancy in the values of ΔG_f^o of Ni_3TeO_6 the present study has been carried out to generate reliable thermochemical data on the multicomponent oxide systems involving tellurium and one of the elements of the clad material.

4.2 Vapour pressure measurement

The vapour pressure of TeO_2 (g) over the phase mixture Cr_2O_3 (s) + Cr_2TeO_6 (s) and NiO (s) + Ni_3TeO_6 (s) has been measured using a vertical thermal analyzer (model SETSYS Evolution 16/18 M/s Setaram, France). For determining the standard Gibbs energy of formation of Fe_2TeO_6 a horizontal thermogravimetric analyzer (TGA / SDTA 851^e) supplied by M/s. Mettler Toledo, Switzerland was used as a transpiration set-up. It was calibrated for the measurement of vapour pressure by using TeO_2 (s) and $CdCl_2$ (s) as standards [12]. Details regarding both the thermal analysers are given in experimental section (Chapter 2). The vertical thermal analyzer (SETSYS Evolution 16/18) was used for the first time for vapour pressure measurement using transpiration technique. It was validated for vapour pressure measurements by measuring the vapour pressure of well-studied standard $CdCl_2$(s) by transpiration technique.

4.2.1 Validation

The apparent vapour pressure of $CdCl_2$ (g) in equilibrium with pure solid $CdCl_2$ (s) was derived from the mass-loss of the sample per unit volume of the carrier gas swept over it using the relation

$$p^{app} = W R T_c / M V_c \tag{4.1}$$

where '*W*' is the mass-loss of the sample, V_c is the total volume of the carrier gas (saturated with the vapour species), T_c is the ambient temperature of the carrier gas (298 K), *R* is the universal gas constant and *M* is the molecular mass of the vapour species. High purity argon (< 2vppm each of oxygen and moisture) was used as the carrier gas. It is assumed that the vapour is comprised of only monomeric $CdCl_2$ (g) over the temperature range 734-823 K [13, 14]. In an isothermal experiment at 793 K, the apparent vapour pressure of $CdCl_2$ (g) in the carrier gas flown over $CdCl_2$(s) was found to remain constant over the flow rate region 1.6 to 2.2 dm^3h^{-1} (Fig. 4.1(a)). This indicates the saturation of the carrier gas with the vapour species in this range of flow rate. The linear variation of mass loss rate (d*m*/d*t*) vs flow rate (d*V*/d*t*) as shown in Fig. 4.1(b) indicates true transpiration. Data on the vapour pressure of $CdCl_2$ obtained in various isothermal experiments carried out in this flow regime are presented in Table 4.1. Solid $CdCl_2$ vapourises into $CdCl_2$ vapour according to the following reaction:

$$CdCl_2\ (s) \rightarrow CdCl_2\ (g) \tag{4.2}$$

The results of the vapour pressure measurements are shown in Fig. 4.2. A linear regression analysis of the experimental data yielded the following equation for the temperature dependence of vapour pressure of $CdCl_2$(s).

$$\log p(\mathrm{Pa})\ (\pm 0.02) = 12.06 - 8616.3\ /\ T\ (\mathrm{K})(734 - 823\ \mathrm{K}) \qquad (4.3)$$

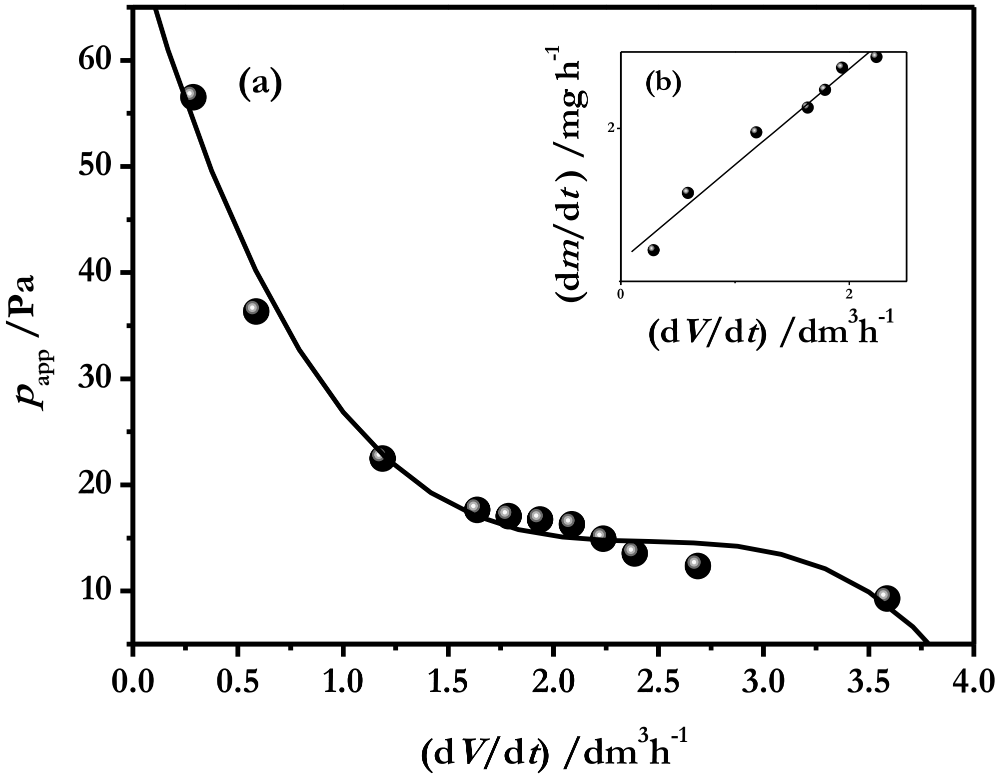

Fig. 4.1 (a) Apparent vapour pressure (p_{app}) (b) Mass loss rate (d*m*/d*t*) of $CdCl_2$ (s) as a function of flow rate (d*V*/d*t*) at 793 K

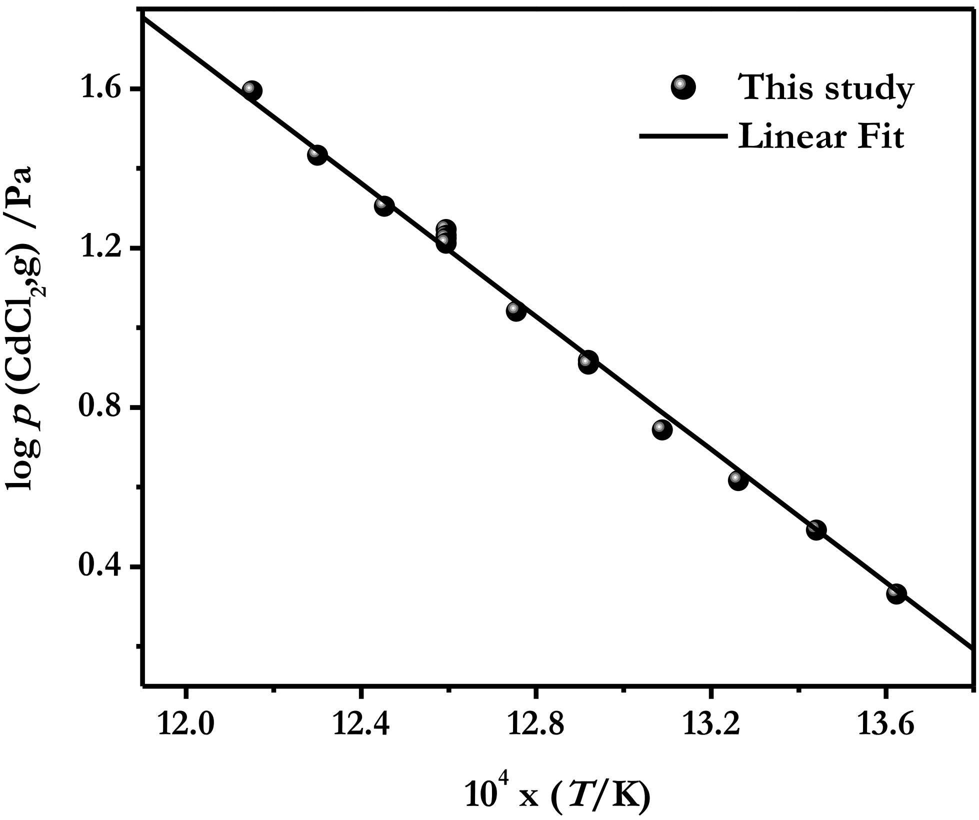

Fig. 4.2 Temperature dependence of equilibrium vapour pressure of $CdCl_2$ (s)

Table 4.1 Data on the vapour pressure of $CdCl_2$

T / **K**	m_{CdCl_2} /**mg**	V_c /**dm^3**	P /**Pa**
734	0.307	1.938	2.143
744	0.41	1.788	3.102
754	0.638	2.088	4.134
764	0.854	2.088	5.534
774	1.184	1.938	8.266
774	1.249	2.088	8.093
784	1.697	2.088	10.996
794	2.135	1.638	17.635
794	2.251	1.788	17.033
794	2.396	1.938	16.727
794	2.513	2.088	16.283
803	2.888	1.938	20.162
813	3.88	1.938	27.087
823	5.194	1.788	39.302

The enthalpy of sublimation of $CdCl_2$(s) obtained from the present study at the mean temperature of measurement (779 K) was found to be 165 ± 3 kJ mol^{-1}. In order to confirm the absence of temperature dependent errors a 'third-law' analysis of the experimental data was carried out. Free energy functions (*fef*) required for the 'third-law' analysis were taken from Ref. [15].

$\Delta H^o_{sub,298K}$ values of $CdCl_2$(s) were calculated using the measured vapour pressure data at different temperatures using the following relation:

$$\Delta H^o_{sub,298K} = \Delta G^o_{vap} - T\,(\Delta fef) \tag{4.4}$$

The temperature dependence of $\Delta H^{o}_{sub,298K}$ is graphically depicted in Fig. 4.3. The mean of these values was found to be 185.1 ± 0.4 kJ mol^{-1} which is in good agreement with the values (169.6 to 189.6 kJ mol^{-1}) reported in the literature [13-22]. Thus, the present study validates the thermal analyzer employed in this study for the measurement of vapour pressures by transpiration technique.

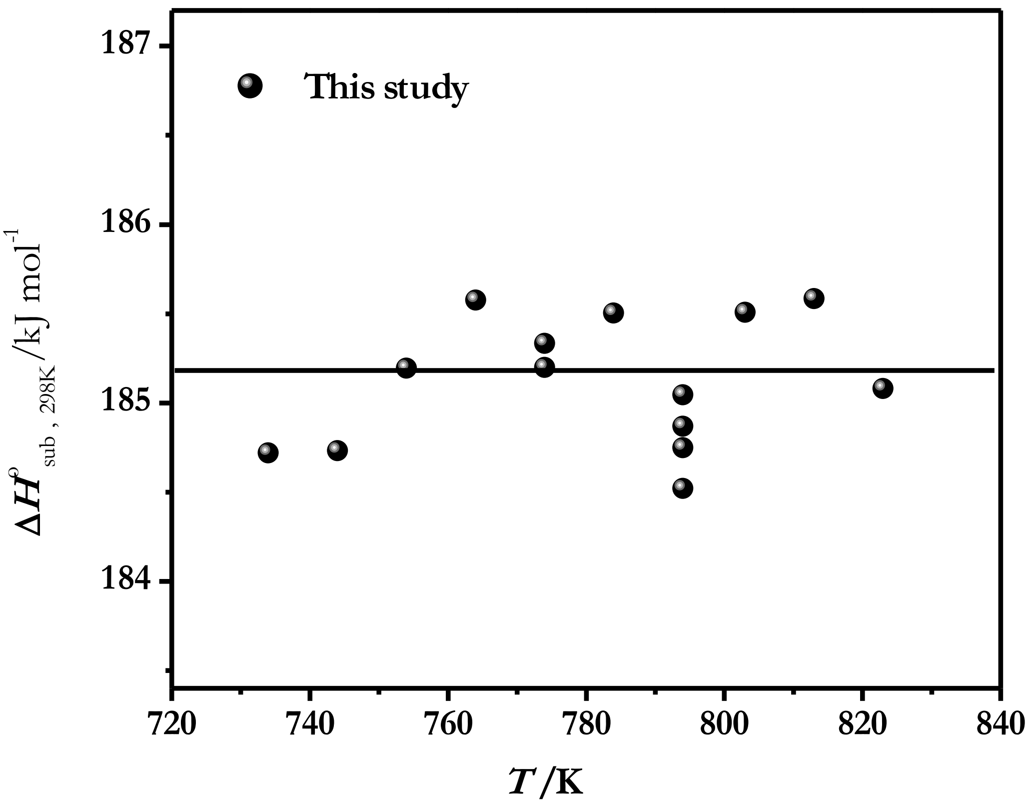

Fig. 4.3 A 'third-law' plot of enthalpy of sublimation of $CdCl_2$ (s)

4.2.2 Vapour pressure measurement of Cr_2TeO_6 (s)

4.2.2.1 Phase Identification

The purity of the compound Cr_2TeO_6 prepared in this study was confirmed by powder XRD technique (Fig. 4.4 (a)). The XRD pattern showed the presence of only Cr_2TeO_6 (JCPDS file no. 15-0696) and the absence of Cr_2O_3 and TeO_2.

4.2.2.2 Non-Isothermal TG of Cr_2TeO_6 (s)

Non-isothermal TG experiments were carried out in order to identify the mass-loss steps and to determine the decomposition temperature of Cr_2TeO_6. The TG curve revealed that the mass-loss occurred at 1173 K which is the inception temperature of decomposition of Cr_2TeO_6 (s). In a typical non-isothermal experiment the mass-loss of Cr_2TeO_6 (heated up to 1400 K) was found to be about 52 % which is in good agreement with the theoretical value of 53.6 %. The TG experiment was interrupted intermittently and the X-ray diffraction patterns of the resultant products were recorded. The results of the XRD studies indicated the presence of Cr_2TeO_6(s) and Cr_2O_3(s) (Fig. 4.4 (b)) thereby indicating the loss of TeO_2 (g). XRD pattern of the residual product after completion of the experiment showed only the presence of Cr_2O_3 (Fig. 4.4 (c)). These observations revealed that the compound volatilized through the following chemical reaction evolving O_2 (g) and TeO_2 (g) as the gaseous products

$$Cr_2TeO_6\,(s) \rightarrow Cr_2O_3\,(s) + TeO_2\,(g) + 1/2\ O_2\,(g) \qquad (4.5)$$

4.2.2.3 Vapour pressure of Cr_2TeO_6 (s)

Cr_2TeO_6 vapourises incongruently in oxygen at 1173 K according to Eq. (4.5). The apparent vapour pressure of TeO_2 (g) in equilibrium with a mixture of Cr_2TeO_6 (s) and Cr_2O_3 (s) was determined using equation (4.1).

The mass-loss of the sample per unit volume of the carrier gas swept over Cr_2TeO_6 was monitored as a function of flow rate at 1233 K. The results are shown in Fig. 4.5(a). The linear relation between $\mathrm{d}m/\mathrm{d}t$ and $\mathrm{d}V/\mathrm{d}t$ is shown in Fig. 4.5(b). The mass-loss was found to remain constant in the range of flow rate between 1.9 and 2.7 $dm^3\ h^{-1}$ indicating thereby saturation of the carrier gas with TeO_2 vapour in this range of flow rates. Hence, in the present study the vapour pressure measurements were carried out at a flow rate of 1.9-2.7 dm^3h^{-1} over the temperature range 1183-1293 K. The vapour species in the temperature range of the present measurements is assumed to be predominantly monomeric TeO_2 (g). The contribution of all other tellurium-bearing specii [TeO, $(TeO)_2$, Te_2] to the total pressure was estimated to be less than 5% from the mass spectrometric studies by Meunow et al [23].

The vapour pressure of TeO_2 (g) over the phase mixture of Cr_2TeO_6 (s) and Cr_2O_3 (s) was calculated at different temperatures from the observed mass-loss of the sample m_{total}. As the mass- loss was due to the volatilization of both TeO_2 (g) and O_2 (g) (Eq. (4.5)), m_{total} values were corrected for the contribution of O_2 (g)

$$m_{TeO_2} = m_{total}\left[\frac{M_{TeO_2}}{M_{TeO_2} + 0.5M_{O_2}}\right] \tag{4.6}$$

where M_{TeO_2} is the molecular mass of TeO_2, M_{O_2} is the molecular mass of O_2, m_{total} is the mass loss due to both TeO_2 as well as O_2 and m_{TeO_2} is the mass loss due to TeO_2 only. The vapour pressures of TeO_2 at various temperatures measured in this study are given in Table 4.2 along with the mass-loss and flow rate of the carrier gas.

The temperature dependence of vapour pressure (Fig. 4.6) could be expressed as

$$\log p(\text{Pa})\ (\pm 0.04) = 18.57 – 21199/\ T\ (\text{K})(1183 – 1293\ \text{K}) \tag{4.7}$$

The standard Gibbs energy change, $\Delta G°$ for the reaction (4.5) could be expressed by the following expression

ΔG_r^o = - $RT\ ln\ K$ where K = equilibrium constant

$$= -RT \ln\left[\frac{a_{Cr_2O_3}\, p_{TeO_2}\, p_{O_2}^{1/2}}{a_{Cr_2TeO_6}}\right] \tag{4.8}$$

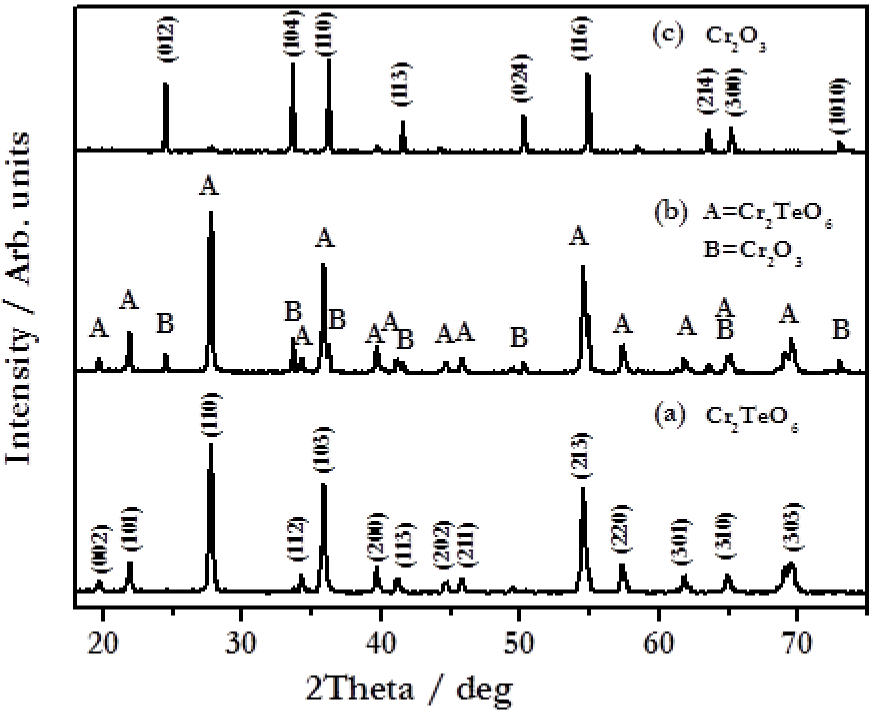

Fig. 4.4 XRD patterns of (a) Cr_2TeO_6 (s) (b) intermediate (c) final product

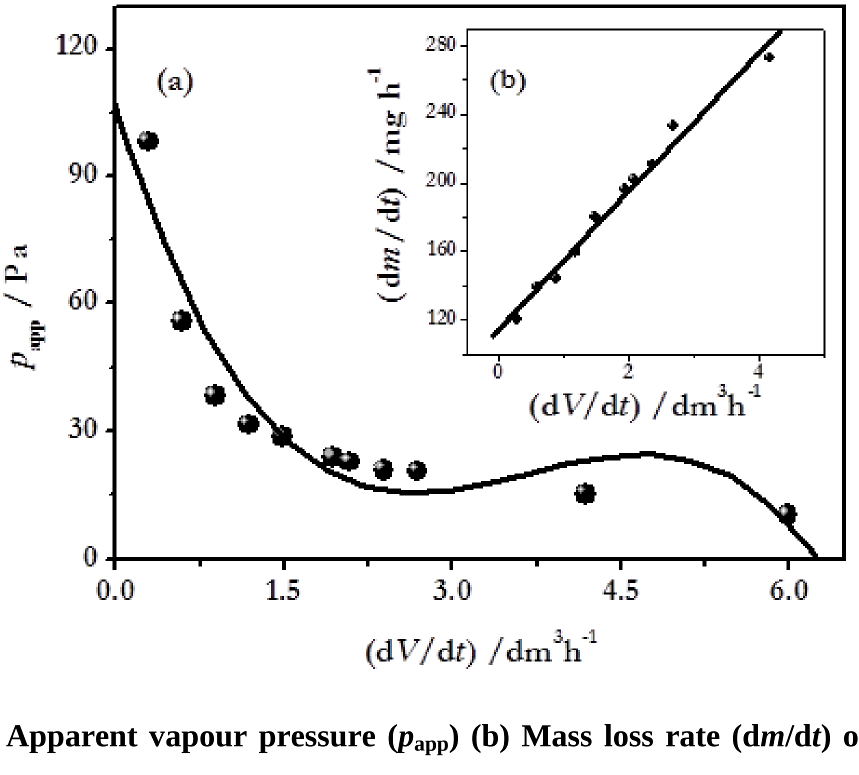

Fig. 4.5 (a) Apparent vapour pressure (p_{app}) (b) Mass loss rate (dm/dt) of TeO_2 (g) over the phase mixture Cr_2O_3 (s) + Cr_2TeO_6 (s) as a function of flow rate (dV/dt) at 1233 K

where a represents thermodynamic activity. $a_{Cr_2O_3}$ and $a_{Cr_2TeO_6}$ are unity and p_{O_2} is one atmosphere, hence,

$$\Delta G_r^o = - RT \ln p_{TeO_2} \tag{4.9}$$

Incorporating Eq. (4.7) in Eq. (4.9),

$$\Delta G_r^o \; (\pm 0.5 \text{ kJ mol}^{-1}) = 405.9 - 0.2597\, T \text{ (K)} \tag{4.10}$$

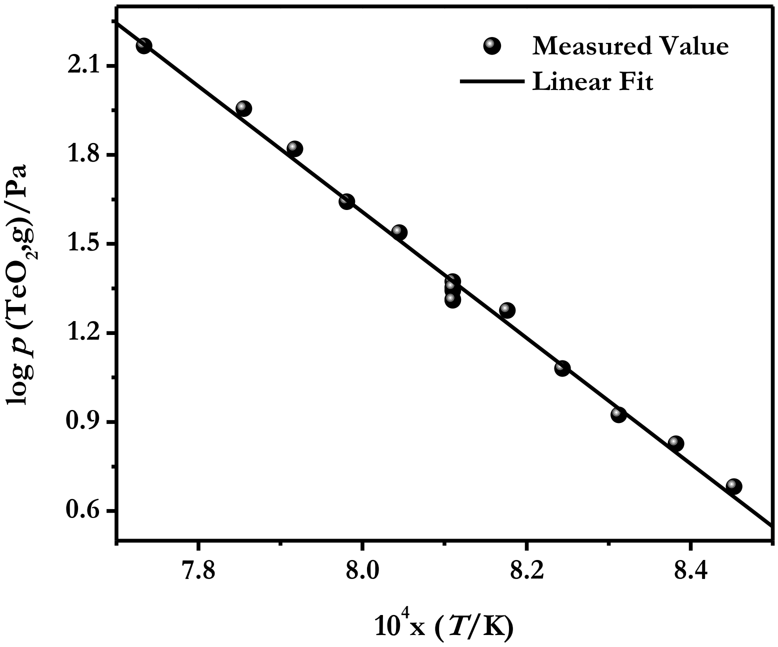

Fig. 4.6 Temperature dependence of equilibrium vapour pressure of TeO_2 (g) over the phase mixture Cr_2O_3 (s) + Cr_2TeO_6 (s)

The standard Gibbs energy of formation of Cr_2TeO_6 could be expressed in terms of the partial pressure of TeO_2 (g) over the phase mixture Cr_2TeO_6 and Cr_2O_3 by the following equation:

$$\Delta G_f^o \; (Cr_2TeO_6, s) = \Delta G_f^o \; (Cr_2O_3, s) + \Delta G_f^o (TeO_2, g) - \Delta G_r^o \tag{4.11}$$

Incorporating the values of ΔG_f^o (Cr_2O_3, s) and ΔG_f^o (TeO_2, g) from the Ref. [20] in Eq. (4.11), ΔG_f^o (Cr_2TeO_6, s) could be derived.

$$\Delta G_f^o \text{ (Cr}_2\text{TeO}_6\text{, s) } (\pm 12 \text{ kJ mol}^{-1}) = -1625.6 + 0.5336\, T \text{ (K)} \qquad (4.12)$$

Since the vapour pressure of TeO_2 was measured at temperatures above its melting point, ΔG_f^o (Cr_2TeO_6, s) was also calculated with liquid TeO_2 as the reference state. In this case, ΔG_f^o (Cr_2TeO_6, s) could be represented as

$$\Delta G_f^o \text{ (Cr}_2\text{TeO}_6\text{, s)} = \Delta G_f^o \text{ (Cr}_2\text{O}_3\text{, s)} + \Delta G_f^o \text{ (TeO}_2\text{, l)} + RT \ln \left(\frac{p_{TeO_2}}{p^o_{TeO_2}}\right) \qquad (4.13)$$

For the calculation of ΔG_f^o (Cr_2TeO_6, s), the temperature dependence of the vapour pressure of TeO_2 (g) ($p^o_{TeO_2}$) over pure liquid TeO_2 was taken from Ref. [24]. By incorporating the values of ΔG_f^o (Cr_2O_3, s) and ΔG_f^o (TeO_2, l) [20], Gibbs energy of formation of Cr_2TeO_6 was derived as follows:

$$\Delta G_f^o \text{ (Cr}_2\text{TeO}_6\text{, s) } (\pm 12.5 \text{ kJ mol}^{-1}) = -1620.5 + 0.5326\, T \text{ (K)} \qquad (4.14)$$

ΔG_f^o (Cr_2TeO_6, s) values obtained from Eq. (4.12) and (4.14) at various temperatures are compared in Table 4.2. The slope and intercept of Eq. (4.12) and (4.14) correspond to the standard molar enthalpy and entropy of formation of Cr_2TeO_6 (s) from the elements at the temperature range of 1183–1293 K. The average second-law enthalpy of formation of Cr_2TeO_6 obtained from the present work was found to be -1622.5 ± 4.1 kJ mol^{-1} at 1238 K, the mean temperature of measurement.

Krishnan et al. [5] have measured ΔG_f^o (Cr_2TeO_6, s) over the temperature range (1014–1100 K) by Knudsen cell effusion method and reported the following equation:

$$\Delta G_f^o \text{ (Cr}_2\text{TeO}_6\text{, s) } (\pm 15 \text{ kJ mol}^{-1}) = -1651.6 + 0.56833\, T \text{ (K)} \qquad (4.15)$$

On extrapolation, the standard Gibbs energy of formation of Cr_2TeO_6 at 1100 K was found to be -1034.6 kJ mol^{-1} (using Eq. 4.14) which is in good agreement with the value (-1028.1 kJ mol^{-1}) obtained by Krishnan et al [5].

Table 4.2 Data on the vapour pressure and standard Gibbs energy of formation of Cr_2TeO_6

T / **K**	m_{TeO_2} **/mg**	V_c **/dm^3**	P **/Pa**		ΔG_f^o **(Cr_2TeO_6,s)/kJ mol^{-1}**	
			$p^{(a)}_{TeO_2}$	$p^{o}_{TeO_2}$	**(b)**	**(c)**
1183	0.738	2.388	4.803	327.539	-993.5	-989.5
1193	0.901	2.088	6.704	396.241	-988.3	-984.3
1203	1.289	2.388	8.387	477.839	-984.1	-980.2
1213	1.615	2.088	12.021	574.464	-978.5	-974.6
1223	2.529	2.088	18.826	688.552	-972.0	-968.1
1233	3.374	2.388	21.956	822.876	-968.4	-964.5
1233	2.942	1.938	23.592	822.876	-967.6	-963.7
1233	3.027	2.088	22.533	822.876	-968.1	-964.2
1233	3.157	2.388	20.542	822.876	-969.1	-965.2
1233	3.526	2.688	20.388	822.876	-969.1	-965.2
1243	4.631	2.088	34.465	980.589	-961.7	-957.8
1253	6.734	2.388	43.822	1165.263	-957.1	-953.2
1263	8.863	2.088	65.961	1380.939	-950.7	-946.9
1273	12.125	2.088	90.246	1632.175	-945.3	-941.4
1293	19.728	2.088	146.832	2262.469	-935.8	-931.9

$p^{(a)}_{TeO_2}$ calculated using Eq.(4.7), $p^{o}_{TeO_2}$ extrapolated values from Ref. [24], (b) ΔG_f^o (Cr_2TeO_6,s) using Eq. (4.12), (c) ΔG_f^o (Cr_2TeO_6,s) using Eq. (4.14)

4.2.3 Vapour pressure measurement of Fe_2TeO_6 (s)

4.2.3.1 Phase Identification

The purity of the compound Fe_2TeO_6 (s) synthesized in this study was ascertained by powder XRD technique (Fig. 4.7(b)). The XRD pattern showed that the sample is Fe_2TeO_6 (s) (PDF-4+ 2013 file no. 04-009-3444 Fig. 4.7(a)) and was devoid of Fe_2O_3 (s) and TeO_2 (s).

4.2.3.2 Non-Isothermal TG of Fe_2TeO_6 (s)

Non-isothermal TG experiments were carried out in order to determine the decomposition temperature of Fe_2TeO_6 (s). The thermogram revealed that the sample started loosing mass at 1070 K which is the inception temperature of decomposition of Fe_2TeO_6 (s). In a typical non-isothermal experiment the mass-loss of Fe_2TeO_6 (s) (heated up to 1573 K at 10 K min^{-1}) was found to be about 47.6 %. It is surmised that heating of sample at high temperature may give mass-loss closer to the theoretical value of 52.4 % calculated from the following chemical reaction (eqn. (4.16)).

$$Fe_2TeO_6\,(s) \rightarrow Fe_2O_3\,(s) + TeO_2\,(g) + 1/2\ O_2\,(g) \qquad (4.16)$$

The thermogravimetry experiment was interrupted intermittently to collect sample for recording the XRD patterns of the intermediates and products. The X-ray diffraction analysis indicated the presence of Fe_2TeO_6(s) and Fe_2O_3(s) (Fig. 4.7(c)), thereby indicating that TeO_2 has been lost by vaporization. XRD pattern pertaining to the residue obtained after heating the sample up to 1573 K showed peaks corresponding to the phase Fe_2O_3 (s) only (Fig. 4.7(d)) (PDF-4+ 2013 file no. 00-033-0664 Fig. 4.7(e)). It is possible that Fe_2TeO_6 present in the residue is less than the detection limit of XRD as XRD pattern of residue did not show the presence of Fe_2TeO_6. In view of the above it is reasonable to conclude that this ternary oxide volatilizes incongruently through chemical reaction (eqn. (4.16)) involving O_2 (g) as one of the gaseous products.

4.2.3.3 Vapour pressure of Fe_2TeO_6

The mass-loss of the samples (Fe_2TeO_6 (s)) per unit volume of the carrier gas (pure oxygen) swept over it was monitored as a function of flow rate at 1123 K. A plot of p^{app} against the flow rate of carrier gas at 1123 K for Fe_2TeO_6 (s) is shown in Fig. 4.8. The existence of a plateau over the flow rates 12.3 – 14.2 $dm^3\ h^{-1}$ shows that the vapourisation rate was adequate to saturate the carrier gas for any flow rate within this range. Equilibrium vapour pressure was found to remain constant in the range of flow rates between 12.3 and 14.2 $dm^3\ h^{-1}$. The vapour pressure measurements at various temperatures (1103-1203 K) were carried out by employing flow rates that pertained to these plateau regions. A program with three heating rate segments was used e.g. for an isothermal experiment at 1103 K. In the first segment sample was heated from room temperature to 1083 K at a heating rate of 25 K min^{-1}. In the second segment sample was heated from 1083 K to 1103 K at 10 K min^{-1}. In the last segment, sample was heated isothermally at 1103 K for 1 h. Similar heating program was used for all isothermal experiments.

The vapour pressures of TeO_2 (g) over the phase mixtures of Fe_2TeO_6 (s) and Fe_2O_3 (s) was calculated at different temperatures from the values of the mass-loss of the sample m_{total} per unit volume of O_2 (g) at a pressure of one atmosphere. The values of the vapour pressure of TeO_2 at various temperatures measured in this study are given in Table 4.3 along with the corresponding mass-loss and flow rate of the carrier gas.

The temperature dependence of the measured values of the vapour pressure as plotted in Fig. 4.9 could be represented by the following least-squares expression eqn. (4.17)

$$\log (p\ (TeO_2, g) / \text{atm} \pm 0.03) = 12.52 - 19836 / T \quad (1103 - 1203\ K) \qquad (4.17)$$

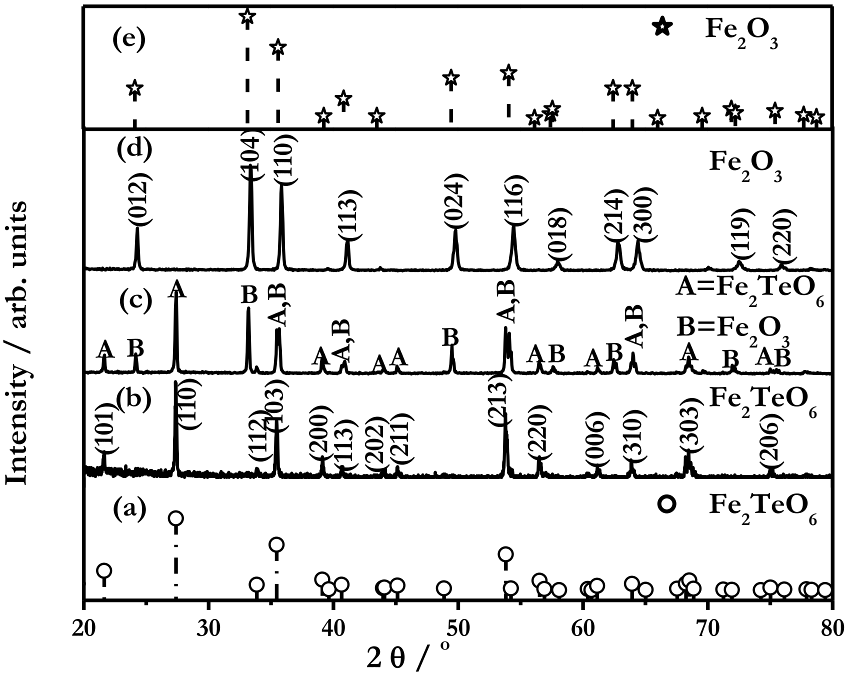

Fig. 4.7 X-ray diffraction patterns of (a) JCPDF 04-009-3444 (b) Fe_2TeO_6 (s) (c) intermediate (d) final product (e) JCPDF 00-33-0664

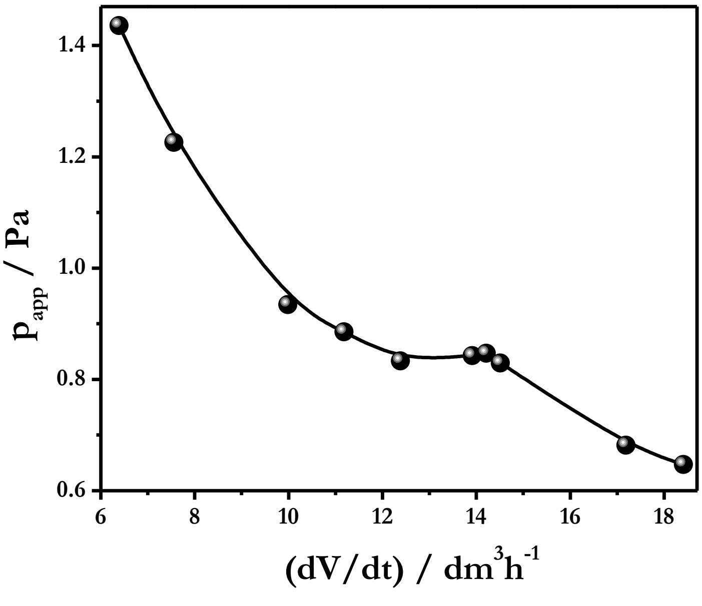

Fig. 4.8 A plot of apparent vapour pressure versus flow rate of carrier gas at 1123 K for Fe_2TeO_6 (s)

The standard Gibbs energy change, ΔG_r^o for the reaction (4.16) could be expressed by the following expression eqn. (4.18)

$$\Delta G_r^o / (\text{kJ mol}^{-1}) \pm 0.6 \quad = \quad 379.4 - 0.2394\ T \quad (1103 - 1203\ \text{K}) \quad (4.18)$$

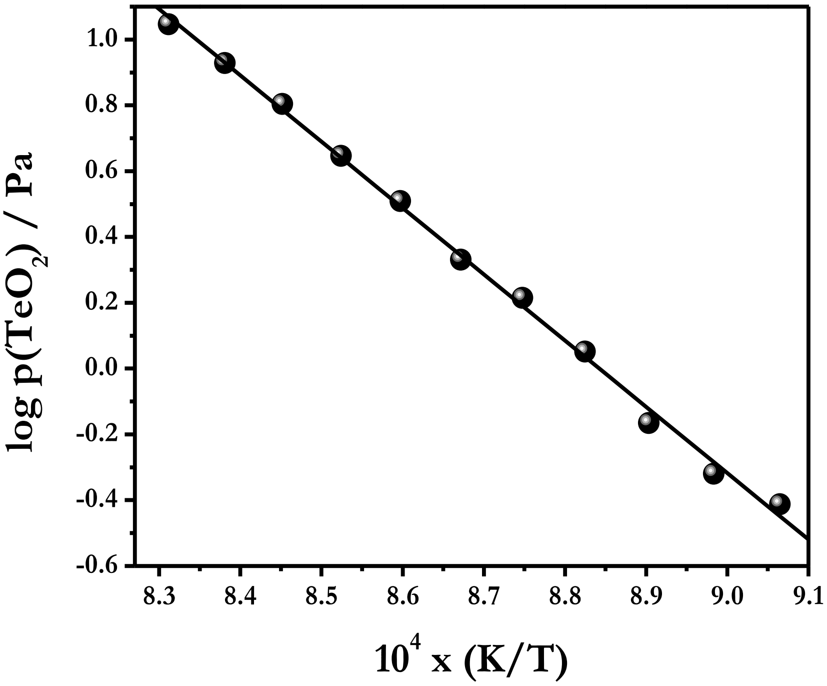

Fig. 4.9 Temperature dependence of equilibrium vapour pressure of TeO_2 (g) over the phase field Fe_2O_3 (s) + Fe_2TeO_6 (s)

The standard Gibbs energy of formation of Fe_2TeO_6 (s) could be expressed in terms of the partial pressure of TeO_2 (g) over the phase mixture Fe_2TeO_6 (s) and Fe_2O_3 (s) by the following equation (4.19):

$$\Delta G_f^o\ (Fe_2TeO_6, s) = \Delta G_f^o\ (Fe_2O_3, s) + \Delta G_f^o\ (TeO_2, g) - \Delta G_r^o \qquad (4.19)$$

Incorporating the values of ΔG_f^o (Fe_2O_3, s) and ΔG_f^o (TeO_2, g) cited in ref. [20] in Eqn. (4.19), the temperature dependence of ΔG_f^o (Fe_2TeO_6, s) could be derived (eqn. (4.20)).

ΔG_f^o(Fe$_2$TeO$_6$, s)/ (kJ mol^{-1}) ±11 = -1276.3 + 0.507 T (1103-1203 K) (4.20)

ΔG_f^o (Fe$_2$TeO$_6$, s) was also determined (Eq. (4.21)) using TeO$_2$ (l) as the reference state as the temperature of present study was above melting point of TeO$_2$ (s).

ΔG_f^o(Fe$_2$TeO$_6$, s) / (kJ mol^{-1}) ± 11.5 = -1271.1 + 0.506 T (1103-1203 K) (4.21)

ΔG_f^o (Fe$_2$TeO$_6$, s) values obtained from eq. (4.20) and (4.21) at different temperatures are compared in Table 4.3.

Table 4.3 Data on the vapour pressure and standard Gibb's energy of formation of Fe$_2$TeO$_6$

T / K	m_{TeO_2} /mg	V_c /dm^3	P /Pa		ΔG_f^o (Fe$_2$TeO$_6$,s)/kJ mol^{-1}	
			$p_{TeO_2}^{(a)}$	$p_{TeO_2}^{o}$	(b)	(c)
1103	0.355	13.5	0.371	63.054	-713.2	-712.5
1113	0.45	13.5	0.471	78.484	-709.3	-708.7
1123	0.609	12.6	0.683	97.310	-704.1	-703.6
1133	1.01	12.9	1.106	120.195	-697.8	-697.4
1143	1.416	12.3	1.626	147.913	-692.3	-692.0
1153	1.935	12.9	2.120	181.371	-687.9	-687.7
1163	2.88	12.9	3.155	221.617	-682.2	-682.1
1173	4.006	13.2	4.289	269.871	-677.3	-677.3
1183	5.688	13.2	6.089	327.539	-671.9	-672.0
1193	7.462	13.2	7.988	396.241	-667.3	-667.5
1203	9.715	13.5	10.170	477.839	-662.9	-663.2

$p_{TeO_2}^{(a)}$ calculated using eq.(4.17), $p_{TeO_2}^{o}$ extrapolated values from Ref. [24], (b) ΔG_f^o (Fe$_2$TeO$_6$,s) using Eq. (4.20), (c) ΔG_f^o (Fe$_2$TeO$_6$,s) using Eq. (4.21)

The slope and intercept pertaining to eqn. (4.20) and (4.21) correspond to the standard molar enthalpy and entropy of formation of Fe_2TeO_6 (s) from the elements in the temperature range of 1103–1203 K. Thus the average second-law enthalpy of formation of Fe_2TeO_6 (s) obtained from the present work was found to be -1273.7 ± 6.5 kJ mol^{-1} at 1153 K, the mean temperature of measurement.

ΔG_f^o (Fe_2TeO_6, (s)) obtained in this study has been compared with that reported in the literature. Upon extrapolation, the standard Gibbs energy of formation of Fe_2TeO_6 (s) at 1000 K was found to be -765.1 kJ mol^{-1}(eqn. 4.21) which is in good agreement with the value (-761.4 kJ mol^{-1}) obtained by Krishnan et al. [5]. Recently ΔG_f^o (Fe_2TeO_6, (s)) has been determined by Sahu et al. [10] by using a transpiration technique over the temperature range 949 – 1053 K. The value of ΔG_f^o (Fe_2TeO_6, s) obtained in Ref. [10] at 1000 K (-736.5 kJ mol^{-1}) is 28.6 and 24.9 kJ mol^{-1} higher than that obtained in the present study and ref. [5] respectively. Sahu et al. [10] have calibrated their transpiration apparatus by measuring the vapour pressure of TeO_2 (g) over TeO_2 (s) at 800 K and established the plateau in the flow rate region of 0.04-0.06 dm^3 min^{-1}. Subsequently they have measured the vapour pressure of TeO_2 (g) over the biphasic mixture Fe_2TeO_6 (s) + Fe_2O_3 (s) in the temperature range 949-1053 K at a carrier gas flow rate of 0.045 dm^3 min^{-1} assuming that the flow rate plateau region established for the system TeO_2 (s) at 800 K is valid for the system Fe_2TeO_6 (s) + Fe_2O_3 (s) over the temperature range 949-1053 K also. The validity of this assumption has not been established by these authors. Hence this assumption could have led to errors in the vapour pressure measurements by transpiration technique. In addition Sahu et al. [10] have derived the vapour pressure by measuring the weight of the condensate, TeO_2 (s). Though the details of the weight measurement have not been reported, it is clear that this small weight (e.g. 40 μg at 949 K), was obtained by subtraction of two large numbers which could lead to substantial errors in the weight measurement. However, in the present study as well as by Krishnan et al. [5], mass-loss was obtained in-situ by a sensitive microbalance. The flow rate plateau region was also established for the system Fe_2TeO_6 (s) + Fe_2O_3 (s) unambiguously in this study. In view of the above, the values of standard Gibbs energy of formation of Fe_2TeO_6 (s) reported in this study as well as by Krishnan et al. [5] are recommended.

4.2.4 Vapour pressure measurement of Ni_3TeO_6 (s)

4.2.4.1 Phase Identification

The purity of the compound Ni_3TeO_6(s) synthesized in this study was ascertained by powder XRD technique (Fig. 4.10). The XRD pattern showed peaks corresponding to Ni_3TeO_6(s) (PDF-4+ 2013 file no. 00-020-0794) only and were devoid of starting compounds NiO(s) and TeO_2(s).

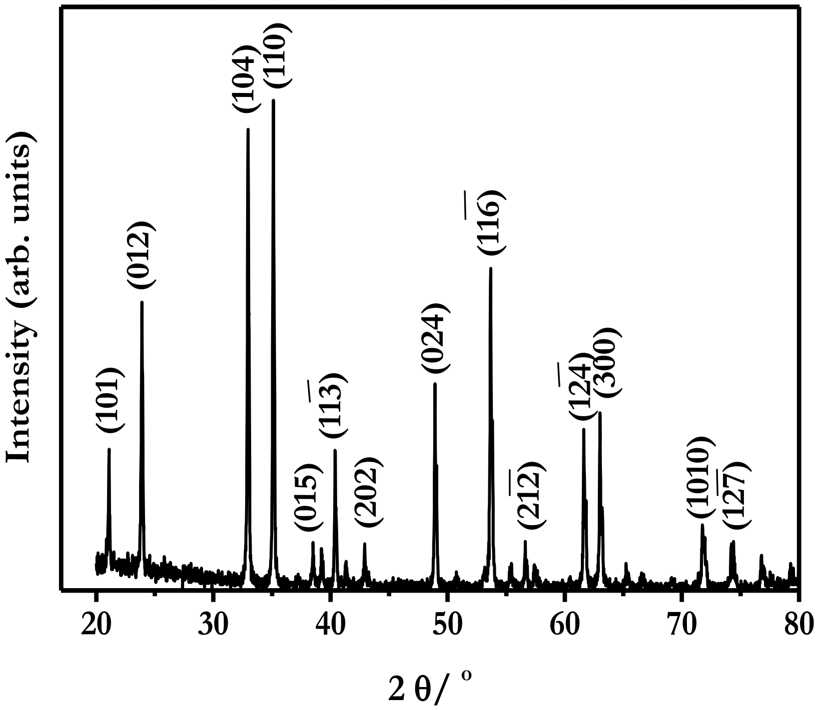

Fig. 4.10 X-ray diffraction pattern of Ni_3TeO_6

4.2.4.2 Non-Isothermal TG of Ni_3TeO_6 (s)

Non-isothermal TG experiments at scan rate 10 K min^{-1} on Ni_3TeO_6 were carried out in order to identify the mass-loss steps and to determine the decomposition temperature under oxygen atmosphere. Ni_3TeO_6 decomposes incongruently through the following chemical reaction (Eq. (4.22)) evolving O_2 (g) and TeO_2 (g) as the gaseous products [7, 8, 10]

$$Ni_3TeO_6\,(s) \rightarrow 3NiO(s) + TeO_2\,(g) + 0.5\,O_2\,(g) \qquad (4.22)$$

4.2.4.3 Vapour pressure of Ni_3TeO_6 (s)

Ni_3TeO_6 decomposes incongruently according to Eq. (4.22), hence the vapour pressure of TeO_2 is invariant at a given temperature and an oxygen pressure of 1 atm. The mass-loss of the sample per unit volume of the carrier gas swept over Ni_3TeO_6 was monitored as a function of flow rate at 1222 K. The results are shown in Fig. 4.11(a). The mass-loss was found to remain constant (plateau region) in the range of flow rate between 3.6 and 4.8 $dm^3\ h^{-1}$ thereby indicating the saturation of the carrier gas with TeO_2 vapour in this flow rate range. The linear relation between dm/dt and dV/dt as shown in Fig. 4.11(b) indicates that the condition for true transpiration is satisfied. Hence, in the present study the measurement of vapour pressure of TeO_2 over biphasic mixture of NiO + Ni_3TeO_6 was carried out at a flow rate in the range of 3.6 – 4.8 dm^3h^{-1} over the temperature range 1143-1272 K. The temperature dependence of vapour pressure (Fig. 4.12) is expressed as Eq. (4.23)

$$\log p\,(\text{Pa})\,(\pm 0.05) = 19.32 - 23085/T\,(\text{K}) \quad (1143 - 1272\ \text{K}) \qquad (4.23)$$

The standard Gibbs energy of formation of Ni_3TeO_6 could be expressed as

$$\Delta G_f^o\,(Ni_3TeO_6, (s)) = 3\,\Delta G_f^o\,(NiO, (s)) + \Delta G_f^o\,(TeO_2, (g)) - \Delta G_r^o \qquad (4.24)$$

where ΔG_r^o is the standard Gibbs energy change, ΔG° for the reaction (4.22)

$\Delta G_r^o = - RT \ln p_{TeO_2}$ where p_{TeO_2} is the partial pressure of TeO_2 over the phase mixture NiO + Ni_3TeO_6.

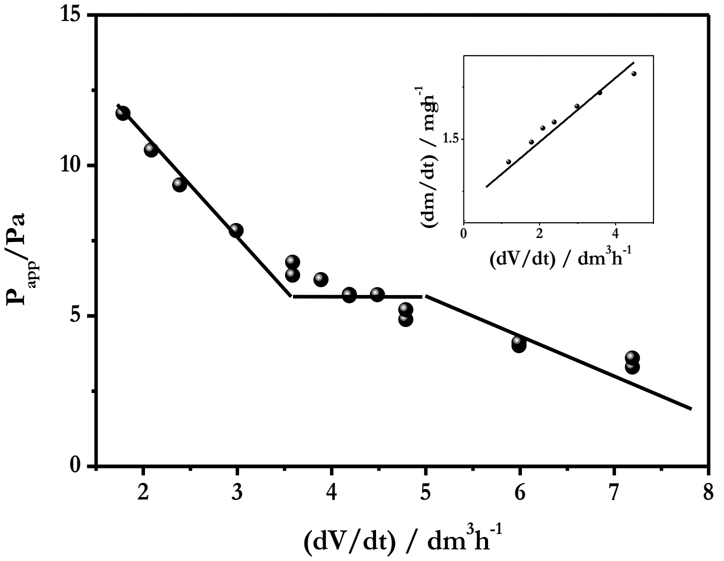

Fig. 4.11 A plot of apparent vapour pressure versus flow rate of carrier gas at 1222 K for Ni_3TeO_6(s)

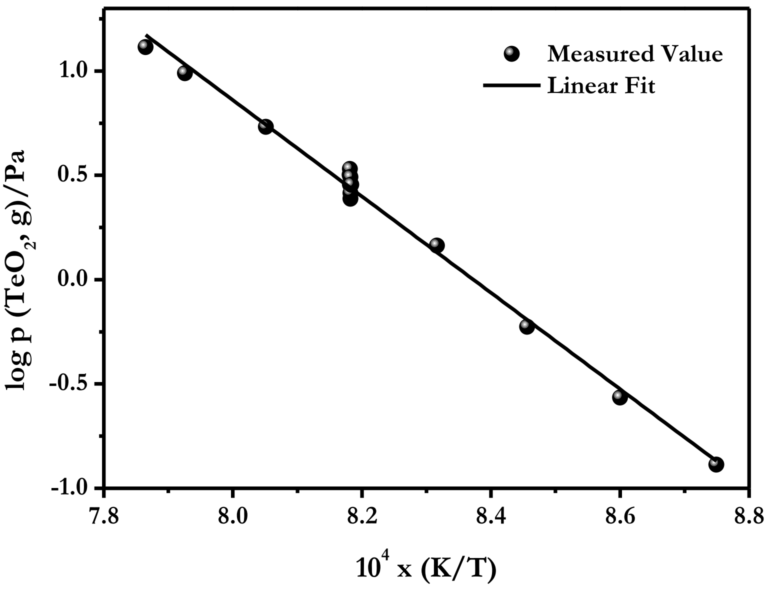

Fig. 4.12 Temperature dependence of equilibrium vapour pressure of TeO_2 (g) over the phase field NiO(s) + Ni_3TeO_6 (s)

ΔG_f^o (Ni_3TeO_6, (s)) is derived by incorporating the values of ΔG_f^o (NiO, (s)) and ΔG_f^o (TeO_2, (g)) from the Ref. [20], in Eq. (4.24). The temperature dependence of ΔG_f^o (Ni_3TeO_6, (s)) is expressed as Eq. (4.25)

$$\Delta G_f^o(\mathrm{Ni_3TeO_6, (s)}) / \ (\mathrm{kJ\ mol^{-1}}) \pm\ 10.5 = -1235.1 + 0.5509\ T \qquad (4.25)$$

The slope and intercept of Eq. (4.25) correspond to the standard molar enthalpy and entropy of formation of Ni_3TeO_6 (s) respectively in the temperature range of 1143–1272 K. Since all the vapour pressure measurements have been carried out at temperatures which lie above the melting temperature of TeO_2(s) (1006 K), the ΔG_f^o (Ni_3TeO_6, (s)) was also calculated taking TeO_2 (l) as the reference state. By incorporating the values of ΔG_f^o(NiO, (s)), ΔG_f^o (TeO_2, (l)) taken from Ref. [20] and temperature dependence of vapour pressure of TeO_2 (g) ($p_{TeO_2}^o$) over pure TeO_2 (l) [24], Gibb's energy of formation of Ni_3TeO_6(s) was derived (Eq. (4.26)).

$$\Delta G_f^o(\mathrm{Ni_3TeO_6, (s)}) / \ (\mathrm{kJ\ mol^{-1}}) \pm\ 11.0 = -1229.8 + 0.556T \qquad (4.26)$$

ΔG_f^o(Ni_3TeO_6, (s)) values obtained from Eq. (4.25) and (4.26) at various temperatures are compared in Table 4.4. The average second-law enthalpy of formation of Ni_3TeO_6 obtained from the present work was found to be -1232.5 ± 11 kJ mol^{-1} at 1208 K, the mean temperature of measurement.

ΔG_f^o(Ni_3TeO_6, s) values obtained in this study were compared with those reported in the literature (Table 4.5). On extrapolation, the standard Gibbs energy of formation of Ni_3TeO_6 at 1000 K was found to be -673.8 kJ mol^{-1} (using Eq. (4.26)) which is in good agreement with the value (-667 kJ mol^{-1}) obtained by Ali et al. [7]. ΔG_f^o(Ni_3TeO_6, s, 1000 K) reported by Mallika et al. [11] and Sahu et al. [10] are -630.3, -631.5 kJ mol^{-1}

which are 43.5, 42.3 kJ mol^{-1} respectively more positive than the value reported in this study.

Table 4.4 Data on the vapour pressure and standard Gibb's energy of formation of Ni_3TeO_6

T / K	m_{TeO_2} /μg	V_c /dm^3	P /Pa		ΔG_f^o (Ni_3TeO_6,s)/kJ mol^{-1}	
			$p_{TeO_2}^{(a)}$	$p_{TeO_2}^{o}$	(b)	(c)
1143	66	3.588	0.130	147.458	-605.4	-594.3
1163	150	3.888	0.272	220.958	-594.4	-583.2
1183	403	4.788	0.594	326.597	-583.4	-572.1
1202	864	4.188	1.457	467.734	-572.9	-561.5
1222	1722	3.588	3.389	674.458	-561.9	-550.4
1222	1679	4.188	2.831	674.458	-561.9	-550.4
1222	1763	4.788	2.600	674.458	-561.9	-550.4
1222	1708	3.888	3.102	674.458	-561.9	-550.4
1222	1813	4.488	2.853	674.458	-561.9	-550.4
1242	3198	4.188	5.393	961.151	-550.9	-539.2
1262	5792	4.188	9.767	1354.418	-539.9	-528.1
1272	7708	4.188	12.998	1601.315	-534.4	-522.6

$p_{TeO_2}^{(a)}$ calculated using Eq.(4.23), $p_{TeO_2}^{o}$ extrapolated values from Ref. [24], (b) ΔG_f^o (Ni_3TeO_6,s) using Eq. (4.25), (c) ΔG_f^o (Ni_3TeO_6,s) using Eq. (4.26)

However, ΔG_f^o(Ni_3TeO_6, s, 1000 K) obtained by Krishnan et al. [8] is -698.7 kJ mol^{-1} which is 24.9 kJ mol^{-1} more negative than the value obtained in this study. Data on ΔG_f^o obtained by Krishnan et al. [8] suffer from the assumption that Knudsen cell wall was inert to O_2, which need not be correct as reported by Ali et al. [7]. Mallika et al. [11]

have obtained ΔG_f^o of Ni_3TeO_6 using EMF technique taking NiO, $NiTeO_3$, Ni_3TeO_6 as the coexisting phases. It has been established that the coexisting phase along with NiO and Ni_3TeO_6 is $Ni_2Te_3O_8$ and not $NiTeO_3$ [8, 25, 26, 27]. Hence, there is difference in the values of ΔG_f^o (Ni_3TeO_6, s) reported in this study and those reported in the literature [8, 11].

Table 4.5 A comparison of ΔG_f^o (Ni_3TeO_6, s)/kJ mol^{-1}measured in the present study with that of reported in literature (extrapolated at 1000 K)

Reference	**Method Used**	**ΔG_f^o (Ni_3TeO_6,s)/kJ mol^{-1}**
Mallika et. al. [11]	EMF	-630.3
Ali et. al. [7]	Transpiration	-667
Krishnan [8]	KEML	-698.7
Sahu [10]	Transpiration	-631.5
This study	Transpiration	-673.8

4.3 Calculation of tellurium potential

From the $\Delta_f G^o$ of various tellurates (Cr_2TeO_6, Fe_2TeO_6, Ni_3TeO_6) obtained in the present study threshold tellurium potential ($\Delta\mu_2$ (Te) – minimum chemical potential of tellurium ($\Delta\mu = RT \ln a$ where a is the activity of tellurium) required for the formation of these tellurates) is calculated at various oxygen potentials of the fuel $(U_mPu_{1-m})O_{2\pm x}$ according to following expressions

$$\Delta\mu_2\ (Te)\ (Cr_2TeO_6) = RT \ln a(Te) = \Delta_f G^o\ (Cr_2TeO_6) - 3RT \ln p_{o_2} - 2RT \ln a(Cr) \quad (4.27)$$

$$\Delta\mu_2\ (Te)\ (Fe_2TeO_6) = RT \ln a(Te) = \Delta_f G^o\ (Fe_2TeO_6) - 3RT \ln p_{o_2} - 2RT \ln a(Fe) \quad (4.28)$$

$$\Delta\mu_2\ (Te)\ (Ni_3TeO_6) = RT \ln a(Te) = \Delta_f G^o\ (Ni_3TeO_6) - 3RT \ln p_{o_2} - 3RT \ln a(Ni) \quad (4.29)$$

The corresponding values of tellurium potential ($\Delta\mu_1$ (Te)) that are likely to be available in the fuel clad gap were computed by evaluating the equilibrium [2, 27, 28]

$$Cs_2Te(s) + (U_mPu_{1-m})O_{2\pm x}(s) + (2\pm x)/2\ O_2(g) = Cs_2(U,Pu)O_4(s) + Te(l) \quad (4.30)$$

A comparison between $\Delta\mu_1$ (Te) and $\Delta\mu_2$ (Te) at various O/M ratio (1.9998, 2.0000, 2.0002) for Pu fraction (0.2 and 0.3) is given in Tables 4.6, 4.7 and 4.8 for Cr_2TeO_6, Fe_2TeO_6, Ni_3TeO_6 respectively. The oxygen potential values of $(U_mPu_{1-m})O_{2\pm x}$ and activity of SS components have been taken from Ref. [29] and [30] respectively.

If $\Delta\mu_1$ (Te) > $\Delta\mu_2$ (Te) there is possibility of formation of these ternary tellurates which is the case for Cr_2TeO_6 at higher O/M ratio. At low O/M ratio, since $\Delta\mu_1$ (Te) < $\Delta\mu_2$ (Te) these tellurates might not be formed on SS clad. Hence oxygen potential also plays an important role in promoting the chemical attack by reactive fission product Tellurium on SS clad.

Table 4.6 A comparison between values of tellurium potential in fuel – clad gap and threshold tellurium potential required for the formation of Cr_2TeO_6 phase on SS 316 clad at 900 K at different O/M ratio of fuel $(U_mPu_{1-m})O_{2\pm x}$ and different plutonium content

O/M ratio (M= U_mPu_{1-m})	Oxygen potential (kJ mol^{-1})	Tellurium potential in fuel-clad gap (kJ mol^{-1})	Tellurium potential required for formation of Cr_2TeO_6 on SS 316 clad (kJ mol^{-1})
		Pu fraction = 0.2	
1.9998	-601	-108	679
2	-463	30	265
2.0002	-336	157	-116
		Pu fraction = 0.3	
1.9998	-589	-96	643
2	-457	36	247
2.0002	-328	165	-140

Table 4.7 A comparison between values of tellurium potential in fuel – clad gap and threshold tellurium potential required for the formation of Fe_2TeO_6 phase on SS 316 clad at 900 K at different O/M ratio of fuel $(U_mPu_{1-m})O_{2\pm x}$ and different plutonium content

O/M ratio ($M= U_mPu_{1-m}$)	Oxygen potential (kJ mol^{-1})	Tellurium potential in fuel-clad gap (kJ mol^{-1})	Tellurium potential required for formation of Fe_2TeO_6 on SS 316 clad (kJ mol^{-1})
		Pu fraction = 0.2	
1.9998	-601	-108	991
2	-463	30	577
2.0002	-336	157	196
		Pu fraction = 0.3	
1.9998	-589	-96	955
2	-457	36	559
2.0002	-328	165	172

Table 4.8 A comparison between values of tellurium potential in fuel – clad gap and threshold tellurium potential required for the formation of Ni_3TeO_6 phase on SS 316 clad at 900 K at different O/M ratio of fuel $(U_mPu_{1-m})O_{2\pm x}$ and different plutonium content

O/M ratio ($M= U_mPu_{1-m}$)	Oxygen potential (kJ mol^{-1})	Tellurium potential in fuel-clad gap (kJ mol^{-1})	Tellurium potential required for formation of Ni_3TeO_6 on SS 316 clad (kJ mol^{-1})
		Pu fraction = 0.2	
1.9998	-601	-108	1089
2	-463	30	675
2.0002	-336	157	294
		Pu fraction = 0.3	
1.9998	-589	-96	1053
2	-457	36	657
2.0002	-328	165	270

4.4 Conclusions

The values of ΔG_f^o (Cr_2TeO_6 (s), ΔG_f^o (Fe_2TeO_6 (s)) and ΔG_f^o (Ni_3TeO_6 (s)) were derived from the experimentally measured values of vapour pressure of TeO_2 (g) by using a transpiration technique. The standard Gibbs energy of formation of Cr_2TeO_6 (s) is being reported for the first time by transpiration method.

An average value of -1622.5 ± 4.1 kJ mol^{-1} at 1238 K, -1273.7 ± 6.5 kJ mol^{-1} at 1153 K and -1232.5 ± 11 kJ mol^{-1} at 1208 K of ‘second-law’ enthalpy of formation were obtained for Cr_2TeO_6, Fe_2TeO_6 and Ni_3TeO_6 respectively, where the temperature mentioned above is the mean temperature of measurement.

This study served to obtain thermodynamic information of these tellurates and also it helped in deducing the possibility of formation of these phases in a nuclear reactor and in gaining better understanding of the clad corrosion. From the present study it can be concluded that there is a possibility of formation of Cr_2TeO_6 phase at higher O/M ratio (higher burn up) upon Te attack on SS clad compared to other tellurates.

References

[1] Kleykamp H. Chemical States of the Fission Products in Oxide Fuels. J Nucl Mater. 1985; 131: 221-46.

[2] Adamson M G, Aitken E A, Lindemer T B. Chemical thermodynamics of Cs and Te fission product interactions in irradiated LMFBR mixed-oxide fuel pins. J Nucl Mater. 1985; 130: 375-92.

[3] Chattopadhyay G, Juneja J M. A thermodynamic database for tellurium bearing systems relevant to nuclear technology. J Nucl Mater. 1993; 202: 10-28.

[4] Cordfunke E H P, Konings R J M. Chemical Interaction in Water Cooled Nuclear Fuel: A Thermochemical Approach. J Nucl Mater. 1988; 152: 301-09.

[5] Krishnan K, Mudher K D S, Rama Rao G A, Venugopal V. Structural and thermochemical studies on Cr_2TeO_6 and Fe_2TeO_6. J Alloys Compd. 2001; 316: 264-68.

[6] Gospodinov G, Atanasova L. Specific thermal and thermodynamic properties of the tellurites $Fe_2(TeO_3)_3$, Fe_2TeO_5 and $Fe_2Te_4O_{11}$. J Therm Anal Calorim. 2008; 91: 655-57.

[7] Ali (Basu) M, Mishra R, Kerkar A S, Bharadwaj S R, Das D. Gibbs energy of formation of solid Ni_3TeO_6 from transpiration studies. J Nucl Mater. 2002; 301: 183-86.

[8] Krishnan K, Rama Rao G A, Mudhler K D S, Venugopal V. Vaporization behavior and Gibbs energy of formation of $Ni_2Te_3O_8$, $NiTe_2O_5$ and Ni_3TeO_6. J Alloys Compd. 1999; 288: 96-101.

[9] Khadilkar H V, Bhojane S M, Kulkarni J, Kulkarni S G. Thermal properties of Na_2TeO_4(s) and $TiTe_3O_8$(s). J Therm Anal Calorim. 2012; DOI 10.1007/s10973-012-2332-4.

[10] Sahu M, Rawat D, Vats B G, Saxena M K, Dash S. Thermo 113hysic-chemical investigations on A–Te–O (A = Cr, Fe, Ni) system. Thermochim Acta. 2014; 585: 50-62.

[11] Mallika C, Sreedharan O.M. Thermodynamic stabilities of $NiTeO_3$ and Ni_3TeO_6 by solid oxide electrolyte e.m.f. method. Thermochim Acta. 1991; 190: 217-224.

[12] Pankajavalli R, Jain A, Sharma A, Anthonysamy S, Ganesan V. Thermodynamic investigation on M–Te–O (M = Sc, Y) system. J Therm Anal Calorim. 2013; 112: 83-93.

[13] Moss H I. Ph.D. Thesis, Indiana University. 1961.

[14] Keneshea F J, Cubicciotti D D. Vapour Pressure of cadmium chloride and thermodynamic data for $CdCl_2$ gas. J Chem Phys. 1964; 40: 1778-79.

[15] Skudlarski K, Dudek J, Kapala J. Thermodynamics of sublimation of cadmium halides investigated by the mass-spectrometric method. J Chem Thermodyn. 1987; 19: 857-62.

[16] Barton J L, Bloom H. A boiling point method for determination of vapour pressures of molten salts. J Phys Chem. 1956; 60: 1413-16.

[17] Bloom H, Welch B J. The vapour pressure of cadmium and zinc chlorides. J Phys Chem. 1958; 62: 1594-95.

[18] Niwa K. Determination of the vapour pressure of solid salts. J Fac Sci. Hakkaido Univ Ser III. 1940; 3: 17-61.

[19] Topor L. Thermodynamic study of alkali metal vapours in equilibrium with the liquid phase. J Chem Thermodyn. 1972; 4: 739-44.

[20] Knacke O, Kubaschewski O, Hesselmann K. Thermochemical Properties of Inorganic Substances. 2nd ed. Germany: Springer-Verlag; 1991.

[21] Cristol B, Houriez J, Balesdent D. Détermination par ébullition isobare de la pression de vapeur de $CdCl_2$ pur et du mélange binaire fondu $CdCl_2$-KCl. J Less-

Common Met. 1985; 113: 43-57.

[22] Dharwadkar S D, Kerkar A S, Samant M S. A microthermogravimetric system for the measurement of vapour pressure by a transpiration method. Thermochim Acta. 1993 ; 217 : 175-86.

[23] Muenow D W, Hastie J W, Hauge R, Bautista R, Margrave J L. Vapourization, thermodynamics and structures of species in the tellurium + oxygen system. Trans Faraday Soc. 1969; 65: 3210-20.

[24] Balakrishnan S, Pankajavalli R, Anthonysamy S, Ananthasivan K. Thermodynamic Stability of Sm_2TeO_6. Thermochim Acta. 2008; 467: 80-85.

[25] Tromel V M, Schmid D. Tellurite des zweiwertigen Mangans, Kobalts und Nickels. Z Anorg Allg Chem. 1972; 387: 230-240.

[26] Lesar A, Popovic A, Marsel J. J Less Common Met. 1988; 143: 151-157.

[27] Lakshmi Narasimhan T S, Nalini S, Sai baba M. Vaporization studies over (NiO + $Ni_2Te_3O_8$) in the Ni–Te–O system by transpiration thermogravimetry and Knudsen effusion mass spectrometry. ThermochimActa. 2015; 600: 67-76.

[28] Lakshmi Narasimhan T S, Nalini S, Manikandan P, Trinadh V V, Sai baba M. Thermodynamic properties over ($Ni_2Te_3O_8$ + $NiTe_2O_5$) in the Ni–Te–O system:

Transpiration thermogravimetric and Knudsen effusion mass spectrometric studies. Int J Mater Res. 2016; 107(2): 158-67.

[29] Krishnaiah MV, Sriramamurthi P. Computational model for the oxygen potentials of mixed uranium-plutonium oxide. J Am Ceram Soc. 1984; 67: 568-71.

[30] Azad M, Sreedharan O M, Gnanamoorthy J B. A novel determination of thermodynamic activities of metals in an AISI 316 stainless steel by a metastable EMF method. J Nucl Mater. 1987; 144: 94-104.

Chapter 5

Thermochemical studies on Cr-Te-O system using EMF technique

5

5.1 Introduction

Thermochemical studies on Cr-Te-O system using EMF technique are presented in this chapter. There are three compounds, viz., Cr_2TeO_6, $Cr_2Te_3O_9$ and $Cr_2Te_4O_{11}$ in the system Cr-Te-O. Oxygen potentials over various phase fields were determined using a two compartment cell assembly. From the measured EMF, Gibbs energies of formation of various ternary oxides were determined. The standard Gibbs energies of formation of $Cr_2Te_3O_9$ and $Cr_2Te_4O_{11}$ were determined for the first time in this study.

5.2 Validation of experimental assembly

Details regarding the twin compartment assembly used in this study are given in the experimental section. The experimental system was validated for EMF measurements by measuring EMF of the following cells

1. (-) Pt, air (P_{O2} = 0.21 atm) | CSZ | O_2(1 atm), Pt (+)
2. (-) Pt, Ni, NiO | CSZ | air (P_{O2} = 0.21 atm), Pt (+)
3. (-) Pt, Cu,Cu_2O | CSZ | air (P_{O2} = 0.21 atm), Pt (+)

The attainment of thermodynamic equilibrium at each temperature of measurement was confirmed by constancy of EMF. EMF was measured precisely using a $5\frac{1}{2}$ digit high impedance meter (input impedance > 10 G ohm). The reproducibility of EMF was established by thermal cycling and also by changing the mole ratio of components of test electrode.

Using cell1, EMF was measured across air (p_{O2} = 0.21 atm) and pure O_2 (p_{O2} = 1 atm) electrodes and was compared with theoretical EMF obtained using Nernst equation. The overall cell reaction can be written as,

$$O_2 + 4e^- \rightarrow 2O^{2-} \tag{5.1}$$

The number of electrons participating in the cell reaction, n, is 4. The measured EMF is related to difference in oxygen activity of two electrodes by

$$4FE = RT \ln p_{o_2} - RT \ln p'_{O_2} \tag{5.2}$$

Where RT ln p'_{O_2} = oxygen potential of sample electrode (pure O_2)

RT ln p_{o_2} = oxygen potential of reference electrode (air)

F = Faraday Constant

It was found to be very close to the theoretical expression E = 0.0337 T. Fig. 5.1 shows the comparison between theoretical and measured values.

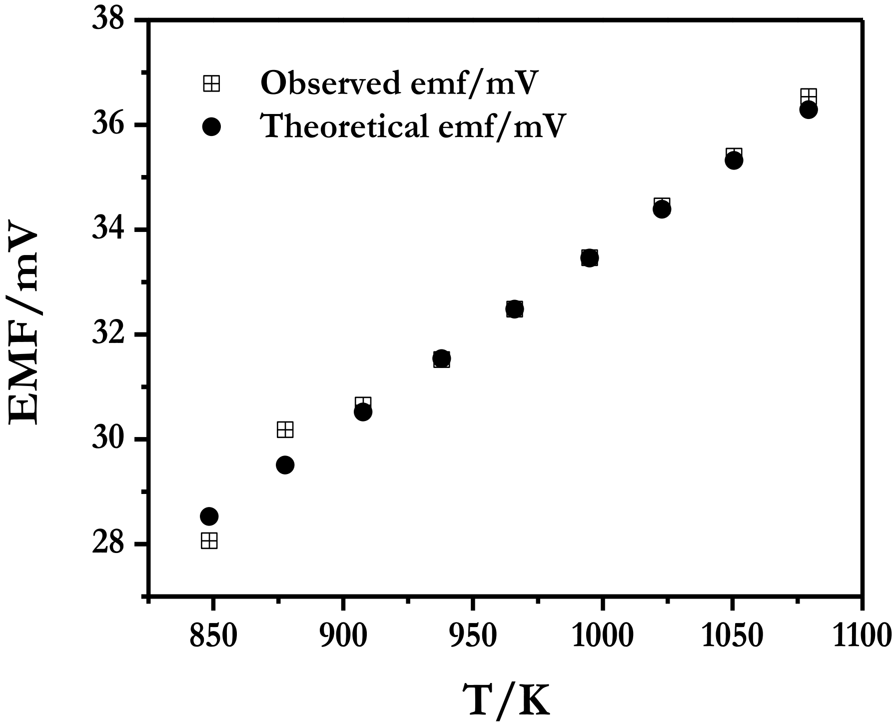

Fig. 5.1 EMF vs Temperature for cell (-) Pt, air (P_{O2} = 0.21 atm) │CSZ│O_2 (1 atm), Pt (+)

Using cell 2 and 3, the standard Gibbs energy of formation of NiO and Cu_2O were determined using the measured EMF values and corrected with respect to pure O_2. A comparison between $\Delta_f G^o$ NiO(s) and $\Delta_f G^o$ Cu_2O(s) obtained in this study and Ref. [1] is shown in Fig. 5.2 and 5.3 respectively.

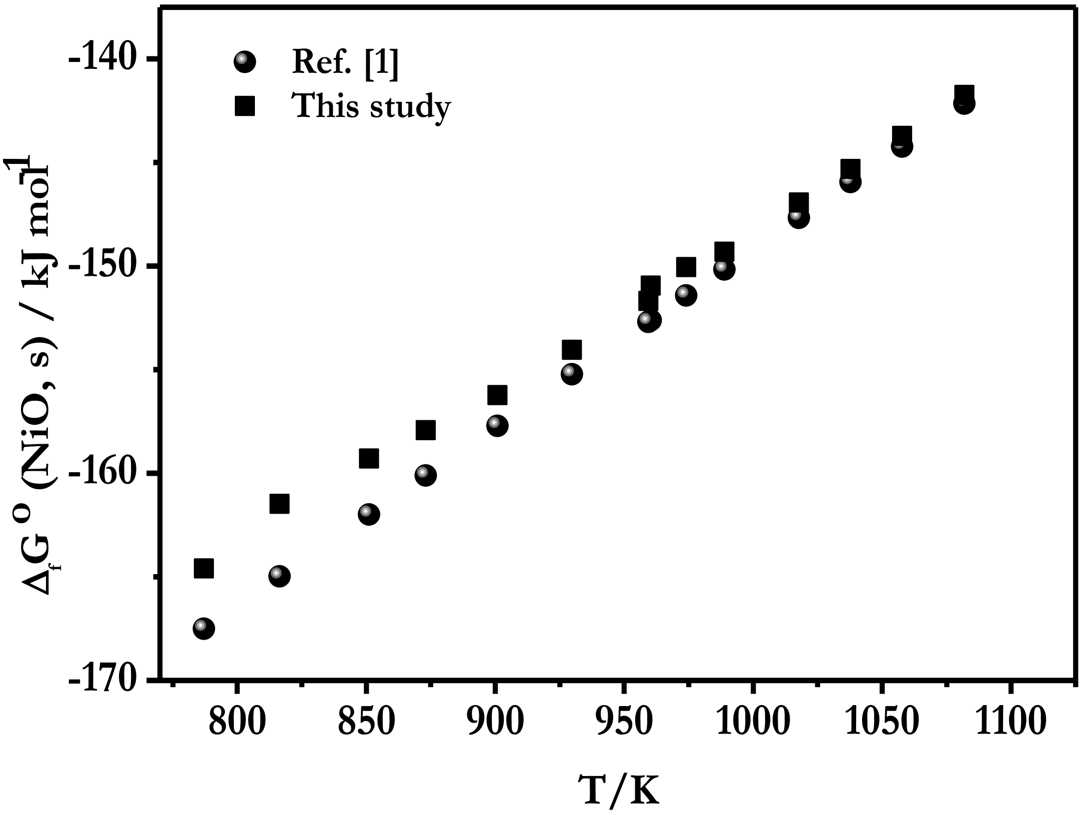

Fig. 5.2 A variation of $\Delta_f G^o$ NiO(s) with temperature obtained using cell 2

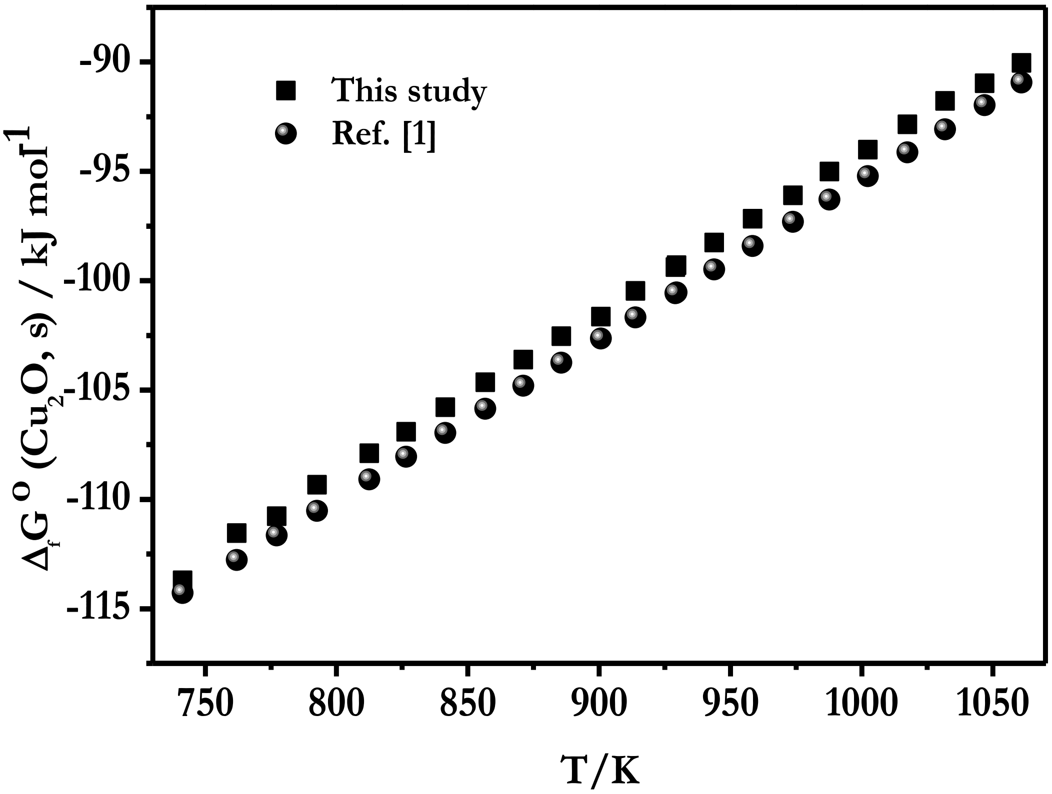

Fig. 5.3 A variation of $\Delta_f G^o$ $Cu_2O(s)$ with temperature obtained using cell 3

$\Delta_f G^o$ NiO(s) and $\Delta_f G^o$ $Cu_2O(s)$ can be represented as following least square expressions (5.3) and (5.4)

Cell 2 $\Delta_f G^o$ NiO(s) = -224.6 + 0.076 T (787<T/K<1082) (5.3)

Cell 3 $\Delta_f G^o$ $Cu_2O(s)$ = -167.7 + 0.074 T (741<T/K<1061) (5.4)

5.3 Thermochemical studies on Cr-Te-O system

After validating the EMF assembly, Gibbs energy of formation of various ternary oxides in the system Cr-Te-O was determined using measured EMF between test and reference electrodes. As discussed in the experimental section (Chapter 2), following phase fields in Cr-Te-O system were established through phase equilibration studies.

(1) $Cr_2O_3(s)$, Te(s), $Cr_2TeO_6(s)$

(2) $Cr_2Te_3O_9(s)$, Te(s), $Cr_2TeO_6(s)$

(3) $Cr_2Te_4O_{11}(s)$, $TeO_2(s)$, $Cr_2TeO_6(s)$

(4) $Cr_2Te_4O_{11}(s)$, Te(s), $Cr_2Te_3O_9(s)$

(5) $Cr_2Te_4O_{11}(s)$, $Cr_2Te_3O_9(s)$, $Cr_2TeO_6(s)$

The following cells were assembled and EMF of these cells were measured. Pt, air (P_{O2} = 0.21 atm) was used as the reference electrode in all the cells. Appropriate three phase mixtures (in the system Cr-Te-O) in the form of compacts (e.g in cell 1, $Cr_2O_3(s)$, Te(s), $Cr_2TeO_6(s)$ in 1:1:1 weight ratio) were used as test electrodes.

I. (-) Pt, $Cr_2O_3(s)$, Te(s), $Cr_2TeO_6(s)$ │ CSZ │ air (P_{O2} = 0.21 atm), Pt (+)

II. (-) Pt, $Cr_2O_3(s)$, Te(l), $Cr_2TeO_6(s)$ │ CSZ │ air (P_{O2} = 0.21 atm), Pt (+)

III. (-) Pt, $Cr_2Te_3O_9(s)$, Te(s), $Cr_2TeO_6(s)$ │ CSZ │ air (P_{O2} = 0.21 atm), Pt (+)

IV. (-) Pt, $Cr_2Te_4O_{11}(s)$, $TeO_2(s)$, $Cr_2TeO_6(s)$ │ CSZ │ air (P_{O2} = 0.21 atm), Pt (+)

V. (-) Pt, $Cr_2Te_4O_{11}(s)$, Te(s), $Cr_2Te_3O_9(s)$ │ CSZ │ air (P_{O2} = 0.21 atm), Pt (+)

VI. (-) Pt, $Cr_2Te_4O_{11}(s)$, $Cr_2TeO_6(s)$, $Cr_2Te_3O_9(s)$ │ CSZ │ air (P_{O2} = 0.21 atm), Pt (+)

EMF values obtained from these cells were corrected with respect to pure O_2 (1 atm) in order to determine standard Gibbs energy of formation of ternary compounds.

5.3.1 Standard Gibbs energy of formation of $Cr_2TeO_6(s)$

The standard Gibbs energy of formation of $Cr_2TeO_6(s)$ was determined using measured EMF between test and reference electrodes (cell I and II).

The EMF is generated due to following cell reactions at anode and cathode of cell I:

$$Cr_2O_3(s) + Te(s) + 3\ O^{2-} = Cr_2TeO_6(s) + 6\ e^- \qquad \text{at anode} \qquad (5.5)$$

$$3/2\ O_2(g) + 6\ e^- = 3\ O^{2-} \qquad \text{at cathode} \qquad (5.6)$$

The net cell reaction is given as:

$$Cr_2O_3(s) + Te(s) + 3/2\ O_2(g) = Cr_2TeO_6(s) \qquad (5.7)$$

Similarly the net cell reaction for cell II is given as:

$$Cr_2O_3(s) + Te(l) + 3/2\ O_2(g) = Cr_2TeO_6(s) \qquad (5.8)$$

The EMF generated in these cells at different experimental temperatures due to the reactions (5.7) and (5.8) are listed in Tables 5.1 and 5.2.

The linear least square fitted expressions for EMF of cell I and II could be expressed as:

$$E\text{ /mV} \pm 3 = 856.3 - 0.5209.(T/\text{K}) \tag{5.9}$$

$$E\text{ /mV} \pm 1.5 = 885.1 - 0.5609.(T/\text{K}) \tag{5.10}$$

Table 5.1: Variation of EMF with temperature for Cell:

(-) Pt, Cr_2O_3(s), Te(s), Cr_2TeO_6(s) │ CSZ │ air (P_{O2} = 0.21 atm), Pt (+)

***T* /K**	***E* /mV**	***T*/K**	***E* /mV**
685	499.9	708	484.1
694.5	498.6	718	483.9
698.5	488.3	718	479.8
707	489.8	722.5	482.2

Table 5.2: Variation of EMF with temperature for Cell:

(-) Pt, Cr_2O_3(s), Te(l), Cr_2TeO_6(s) │ CSZ │ air (P_{O2} = 0.21 atm), Pt (+)

***T* /K**	***E* /mV**	***T*/K**	***E* /mV**	***T* /K**	***E* /mV**	***T*/K**	***E* /mV**
725	475.4	756.5	464.3	787.5	443.8	823	422.5
726	476.1	758.5	460.4	787.5	443.7	828	421.7
728.5	477.3	761	456.4	791	440.4	832	416.6
732	471.4	761.5	457.8	796	439.8	835	418.2
733	473.1	767	456.7	798	438.3	838	415.9
737	473.5	769	454.8	801	435.0	841	410.5
737.5	470.0	772	450.6	805.5	434.2	847.5	410.2
738	471.6	773	451.9	806	434.5	849.5	409.9

746.5	465.9	776	449.7	808	432.8	858	403.5
747	463.8	776.5	450.8	812.5	428.5	864	402.3
747	469.1	782	445.5	818	427.2	867.5	397.0
748.5	465.9	786.5	445.1	820	426.1	877.5	389.2

A variation of cell EMF (I and II) with temperature is shown in Fig. 5.4

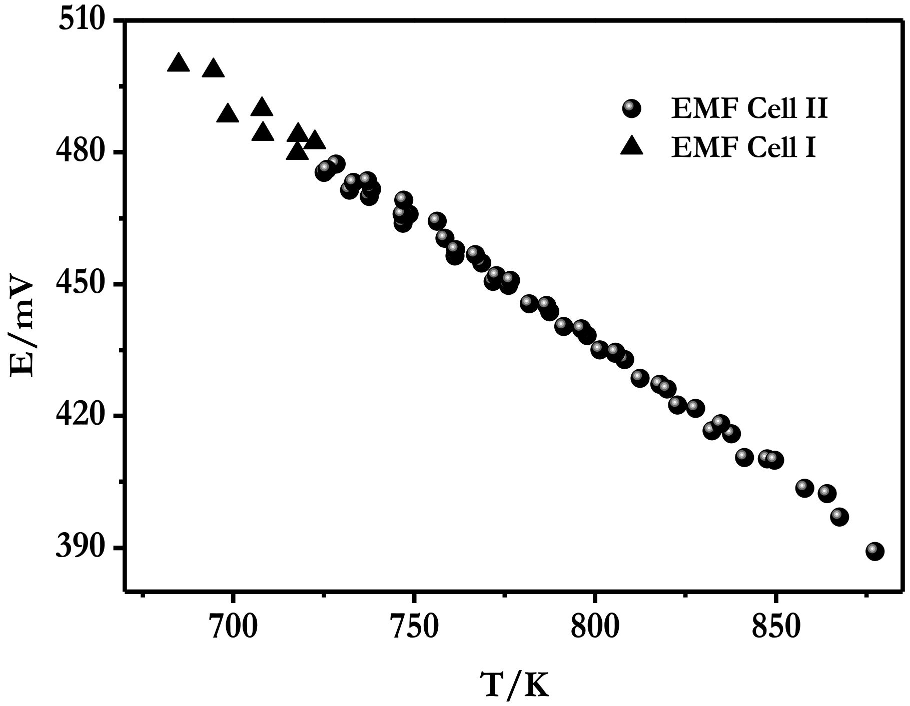

Fig. 5.4 EMF vs Temperature for cells I and II

EMF values obtained from cells I and II were corrected with respect to pure O_2 (1 atm). Using Eqns. (5.9) and (5.10) the standard Gibbs energy of formation of Cr_2TeO_6(s) was determined. For determining Δ_fG^o Cr_2TeO_6(s), Δ_fG^o Cr_2O_3(s) has been taken from Ref. [1]. Δ_fG^o Cr_2TeO_6(s) is represented as the following least square expressions

Cell I Δ_fG^o (Cr_2TeO_6, s) (±11 kJ mol^{-1}) = -1624.3 + 0.5346 T (685<T/K<723) (5.11)

Cell II Δ_fG^o (Cr_2TeO_6, s) (±11 kJ mol^{-1}) = -1644.2 + 0.5606 T (725<T/K<877) (5.12)

The results were compared with those obtained using transpiration technique [Chapter 4] and KEMS technique [2]. A comparison of $\Delta_f G^o$ Cr_2TeO_6 / kJ mol^{-1} at T=1000K is shown in Table 5.3.

Table 5.3 A comparison of $\Delta_f G^o$ Cr_2TeO_6 / kJ mol^{-1} at T=1000K

Cell I EMF	Cell II EMF	Transpiration	Ref [6] KEMS
-1089.8	-1083.6	-1087.9	-1083.3

Using cell I and II enthalpy of transition and transition temperature of Te(s) → Te(l) were calculated. $\Delta_m H^o$ was found to be 17.4 kJ mol^{-1} and transition temperature to be 726 K which are in good agreement with the values of 16.6 kJ mol^{-1} and 723 K respectively reported in literature [1].

5.3.2 Standard Gibbs energy of formation of $Cr_2Te_3O_9$(s)

Using cell III, the standard Gibbs energy of formation of $Cr_2Te_3O_9$(s) was determined employing standard Gibbs energy of formation of Cr_2TeO_6 which was determined using cell II. The cell reactions at anode and cathode of cell III are represented below as Eqn. (5.13) and (5.14):

$$Cr_2TeO_6(s) + 2Te(s) + 3\ O^{2-} = Cr_2Te_3O_9(s) + 6\ e^- \quad \text{at anode} \quad (5.13)$$

$$3/2\ O_2(g) + 6\ e^- = 3\ O^{2-} \quad \text{at cathode} \quad (5.14)$$

The EMF generated in this cell at different experimental temperatures due to the following reaction is listed in Table 5.4.

$$Cr_2TeO_6(s) + 2Te(s) + 3/2\ O_2(g) = Cr_2Te_3O_9(s) \quad (5.15)$$

The linear least square fitted expressions for EMF of cell III could be expressed as:

$$E\ /\text{mV} \pm 1 = 906.8 - 0.5883.(T/\text{K})\ (725<T/\text{K}< 874) \quad (5.16)$$

Table 5.4 Variation of EMF with temperature for Cell:

(-) Pt, $Cr_2Te_3O_9$(s), Te(s), Cr_2TeO_6(s) │ CSZ │ air (P_{O2} = 0.21 atm), Pt (+)

T **/K**	***E*** **/mV**	***T*****/K**	***E*** **/mV**	***T*** **/K**	***E*** **/mV**
725.5	480.5	769	455.1	814	425.4
735	474.5	775	450	814.5	427.7
740	472.5	784	444.6	824	419
744	469	784.5	444.5	829	419.5
754.5	463.3	794	438.7	844	411.3
755	464.7	799.5	435.9	859	403.1
765	456.2	804	432	873.5	394.7

A variation of cell III EMF with temperature is shown in Fig. 5.5

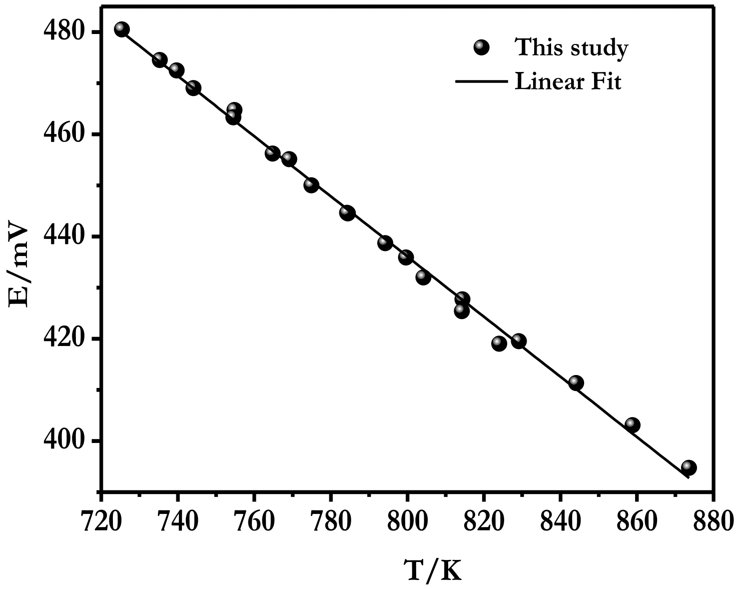

Fig. 5.5 EMF vs Temperature for cell III

EMF values obtained from cell III were corrected with respect to pure O_2 (1 atm). Using Eqn. (5.9) and standard Gibbs energy of formation of Cr_2TeO_6(s) from cell II, Δ_fG^o $Cr_2Te_3O_9$(s) was determined. Δ_fG^o $Cr_2Te_3O_9$(s) is represented as the following least square expression

Δ_fG^o ($Cr_2Te_3O_9$, s) (±11 kJ mol^{-1}) = -2169.2 + 0.8817 T (725<T/K< 874) (5.17)

5.3.3 Standard Gibbs energy of formation of $Cr_2Te_4O_{11}$(s)

Using cells IV, V and VI the standard Gibbs energy of formation of $Cr_2Te_4O_{11}$(s) was determined employing standard Gibbs energy of formation of Cr_2TeO_6 and $Cr_2Te_3O_9$ obtained using cells II and III.

5.3.3.1 Standard Gibbs energy of formation of $Cr_2Te_4O_{11}$(s) using cell IV

The cell reactions at anode and cathode of cell IV are represented below as Eqn. (5.18) and (5.19):

$Cr_2Te_4O_{11}(s) + O^{2-} = Cr_2TeO_6(s) + 3TeO_2(s) + 2\,e^-$ at anode (5.18)

$\frac{1}{2}\,O_2(g) + 2\,e^- = O^{2-}$ at cathode (5.19)

The EMF generated in this cell at different experimental temperatures due reaction (5.20) is listed in Table 5.5.

$Cr_2Te_4O_{11}(s) + 1/2\,O_2(g) = Cr_2TeO_6(s) + 3TeO_2(s)$ (5.20)

The linear least square fitted expression for EMF of cell IV could be expressed as:

E /mV ± 2.6 = 997.5 – 0.7146.(T/K) (704<T/K< 843) (5.21)

Table 5.5 Variation of EMF with temperature for Cell:

(-) Pt, $Cr_2Te_4O_{11}$(s), TeO_2(s), Cr_2TeO_6(s) │ CSZ │ air (P_{O2} = 0.21 atm), Pt (+)

T /K	*E* /mV	*T*/K	*E* /mV	*T* /K	*E* /mV
705	492.0	753	458.0	779	439.0

705	489.0	753	457.8	783	441.6
715.5	484.0	755	460.0	784	435.0
720	488.0	760	453.2	790	430.0
725.5	479.0	763	453.0	793	432.0
730	475.0	765	452.0	793.5	434.3
735	474.9	770	454.0	804	423.8
739.5	468.9	770	446.0	813.5	417.2
745	466.0	772.5	446.0	823	410.5
749	460.0	773	448.3	833	400.2
752	459.5	774.5	444.0	843	390.0

A variation of cell IV EMF with temperature is shown in Fig. 5.6

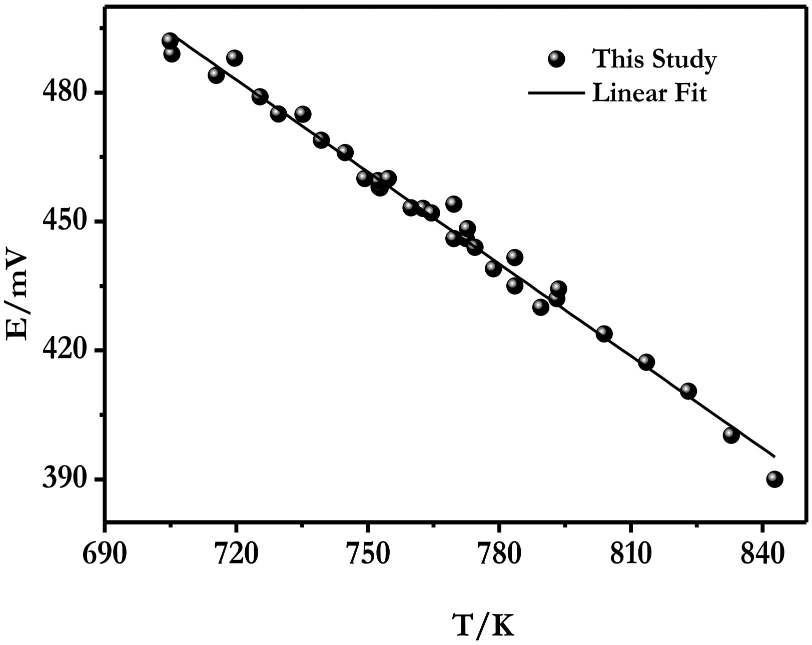

Fig. 5.6 EMF vs Temperature for cell IV

EMF values obtained from cell IV were corrected with respect to pure O_2 (1 atm). Using Eqn. (5.21) and $\Delta_f G^\circ$ Cr_2TeO_6(s) from cell II, $\Delta_f G^\circ$ TeO_2(s) from Ref. [1] the standard Gibbs energy of formation of $Cr_2Te_4O_{11}(s)$ was determined. $\Delta_f G^o$ $Cr_2Te_4O_{11}(s)$ is represented as the following least square expression

$$\Delta_f G^o\ (Cr_2Te_4O_{11}, s)\ (\pm 12\ kJ\ mol^{-1}) = -2458.2 + 1.013\ T\ \ (705<T/K< 843) \quad (5.22)$$

5.3.3.2 Standard Gibbs energy of formation of $Cr_2Te_4O_{11}(s)$ using cell V

The cell reactions at anode and cathode of cell V are represented below as Eqn. (5.23) and (5.24):

$$Cr_2Te_3O_9(s) + Te + 2O^{2-} = Cr_2Te_4O_{11}(s) + 4\ e^- \quad \text{at anode} \quad (5.23)$$

$$O_2(g) + 4\ e^- = 2O^{2-} \quad \text{at cathode} \quad (5.24)$$

The EMF generated in this cell at different experimental temperatures due to reaction (5.25) is listed in Table 5.6.

$$Cr_2Te_3O_9(s) + Te + O_2(g) = Cr_2Te_4O_{11}(s) \quad (5.25)$$

The linear least square fitted expressions for EMF of cell V could be expressed as:

$$E\ /mV \pm 2.6 = 866.8 - 0.5404.(T/K)\ (725<T/K<879) \quad (5.26)$$

Table 5.6 Variation of EMF with temperature for Cell:

(-) Pt, $Cr_2Te_4O_{11}(s)$, Te(s), $Cr_2Te_3O_9(s)$ │ CSZ │ air (P_{O2} = 0.21 atm), Pt (+)

***T* /K**	***E* /mV**	***T*/K**	***E* /mV**	***T* /K**	***E* /mV**	***T*/K**	***E* /mV**
725	471	760	457	794	439.7	835	412.4
730	472.8	761	456	796	438.5	840	413.6
734	466	764	455	800	436.3	843	411.5
735	466	764.5	454	804.5	434.9	850	407.7
734	468	765	454.5	805	432.5	854	404.3
740	468.2	770	451	810	430.6	859.5	401.6
744	463	773	450	814	428.5	864	397.75
745	462	774	449.6	815	426	869.5	395.5

746	463	776	449.6	820	425.3	873.5	391.1
750	462.8	780	447	824.5	422.6	879	390.1
753	458	783.5	445.4	826	419.4		
753.5	459	785	444	830.5	419		
755	459.4	790	441.6	834	417.2		

A variation of cell V EMF with temperature is shown in Fig. 5.7

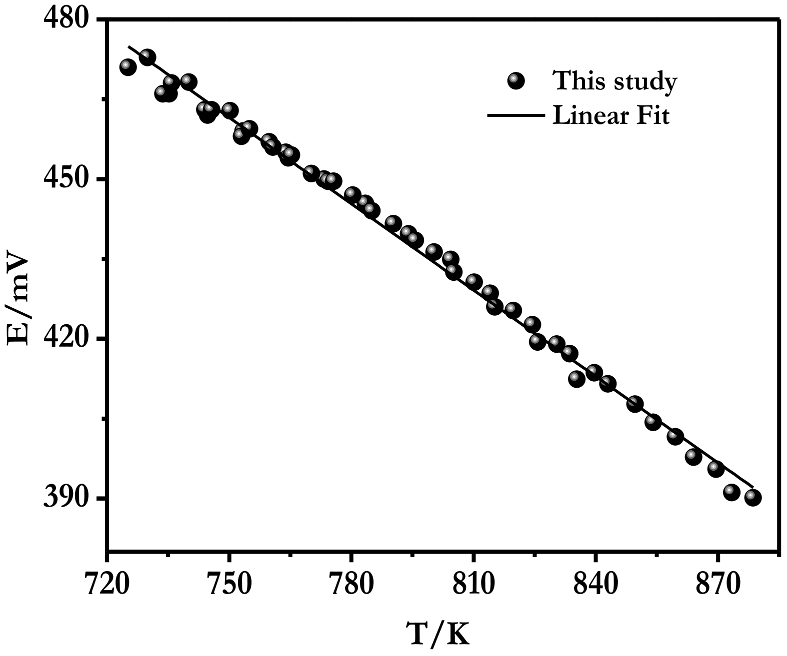

Fig. 5.7 EMF vs Temperature for cell V

EMF values obtained from cell V were corrected with respect to pure O_2 (1 atm). Using Eqn. (5.2) and $\Delta_f G^o$ $Cr_2Te_3O_9$(s) from cell III, the standard Gibbs energy of formation of $Cr_2Te_4O_{11}$(s) was determined. $\Delta_f G^o$ $Cr_2Te_4O_{11}$(s) is represented as the following least square expression:

$\Delta_f G^o$ ($Cr_2Te_4O_{11}$, s) (± 11.3 kJ mol^{-1}) = $-2503.7 + 1.077\ T$ ($725 < T/K < 879$) (5.27)

5.3.3.3 Standard Gibbs energy of formation of $Cr_2Te_4O_{11}$(s) using cell VI

The cell reactions at anode and cathode of cell VI are represented below as Eqn. (5.28) and (5.29):

$3Cr_2Te_3O_9(s) + O^{2-} = 2Cr_2Te_4O_{11}(s) + Cr_2TeO_6(s) + 2\,e^-$ at anode (5.28)

$\frac{1}{2}\,O_2(g) + 2\,e^- = O^{2-}$ at cathode (5.29)

The EMF generated in this cell at different experimental temperatures due to reaction (5.30) is listed in Table 5.7.

$Cr_2Te_3O_9(s) + Te + O_2(g) = Cr_2Te_4O_{11}(s)$ (5.30)

The linear least square fitted expressions for EMF of cell VI could be expressed as:

E /mV ± 3 = 944.8 – 0.6044.(T/K) (720<T/K<856) (5.31)

Table 5.7 Variation of EMF with temperature for Cell:

(-) Pt, $Cr_2Te_4O_{11}(s)$, $Cr_2TeO_6(s)$, $Cr_2Te_3O_9(s)$ │ CSZ │ air (P_{O2} = 0.21 atm), Pt (+)

T **/K**	***E*** **/mV**	***T*****/K**	***E*** **/mV**	***T*** **/K**	***E*** **/mV**
720	507	763	486	818	457
735	499	794	467.9	837	439.8
749	492.6	808.5	453	856.5	421.3

A variation of cell VI EMF with temperature is shown in Fig. 5.8

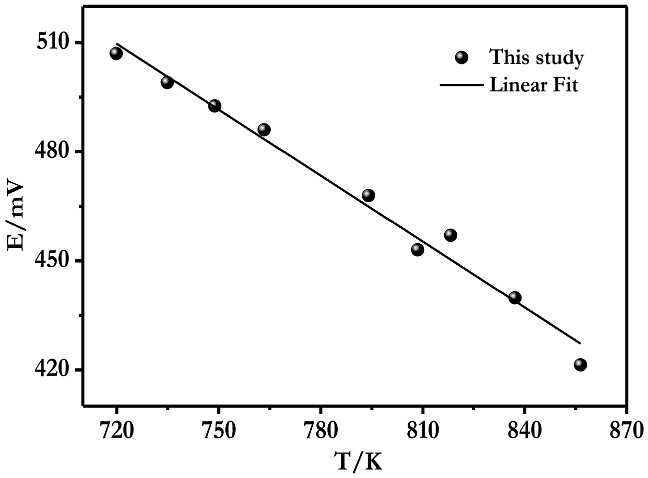

Fig. 5.8 EMF vs Temperature for cell VI

EMF values obtained from cell V were corrected with respect to pure O_2 (1 atm). Using Eqn. (5.26), Δ_fG^o Cr_2TeO_6(s) from cell II and Δ_fG^o $Cr_2Te_3O_9$(s) from cell III, the standard Gibbs energy of formation of $Cr_2Te_4O_{11}$(s) was determined. Δ_fG^o $Cr_2Te_4O_{11}$(s) is represented as the following least square expression:

Δ_fG^o ($Cr_2Te_4O_{11}$, s) (±16 kJ mol^{-1}) = -2522.8 + 1.097 T (720<T/K<856) (5.32)

Δ_fG^o $Cr_2Te_4O_{11}$(s) values obtained from cell IV, V and VI were compared. A comparison of Δ_fG^o $Cr_2Te_4O_{11}$(s) / kJ mol^{-1} at T=800K is shown in Table 5.8.

Table 5.8 A comparison of Δ_fG^o $Cr_2Te_4O_{11}$(s) / kJ mol^{-1} at T=800K

Cell IV	Cell V	Cell VI
-1647.8	-1642.1	-1645.2

5.4 Calculation of tellurium potential

As discussed in chapter 4, threshold tellurium potential ($\Delta\mu_2$ (Te) – minimum chemical potential of tellurium ($\Delta\mu$ = RT ln a where a is the activity of tellurium) required for the formation of $Cr_2Te_3O_9$ and $Cr_2Te_4O_{11}$) is calculated at various oxygen potentials of the fuel $(U_mPu_{1-m})O_{2\pm x}$ according to the following expressions:

$$\Delta\mu_2\,(Te)\,(Cr_2Te_3O_9) = RT\ln a(Te) =$$

$$[\Delta_f G^o\,(Cr_2Te_3O_9) - 9/2\,RT\ln p_{o_2} - 2RT\ln a(Cr)]/3 \qquad (5.33)$$

$$\Delta\mu_2\,(Te)\,(Cr_2Te_4O_{11}) = RT\ln a(Te) =$$

$$[\Delta_f G^o\,(Fe_2TeO_6) - 11/2\,RT\ln p_{o_2} - 2RT\ln a(Cr)\,]/4 \qquad (5.34)$$

The possibility of formation of Cr_2TeO_6 phase on SS clad has already been discussed in chapter 4. The corresponding values of tellurium potential ($\Delta\mu_1$ (Te)) that are likely to be available in the fuel clad gap are computed by evaluating the equilibrium given in (4.30).

A comparison between $\Delta\mu_1$ (Te) and $\Delta\mu_2$ (Te) at various O/M ratios (1.9998, 2.0000, 2.0002) for Pu fraction (0.2 and 0.3) is presented in Tables 5.9, 5.10 for $Cr_2Te_3O_9$ and $Cr_2Te_4O_{11}$ respectively. The oxygen potential values of $(U_mPu_{1-m})O_{2\pm x}$ and activity of Cr in SS 316 ($a(Cr) = 0.316$) has been taken from Ref. [3] and [4] respectively. If $\Delta\mu_2$ (Te) < $\Delta\mu_1$ (Te) there is a possibility of formation of these phases on SS clad. From the positive values of tellurium potential (being meaningless) required for the formation of $Cr_2Te_3O_9$ and $Cr_2Te_4O_{11}$ it can be inferred that formation of these compounds might not occur on SS clad under normal operating conditions.

Table 5.9 A comparison between values of tellurium potential in fuel – clad gap and the threshold tellurium potential required for the formation of $Cr_2Te_3O_9$ phase on SS 316 clad at 900 K at different O/M ratio of fuel $(U_mPu_{1-m})O_{2\pm x}$ and different plutonium content

O/M ratio (M= U_mPu_{1-m})	Oxygen potential	Tellurium potential in fuel-clad gap	Tellurium potential required for formation of $Cr_2Te_3O_9$ on

	(kJ mol^{-1})	(kJ mol^{-1})	SS 316 clad (kJ mol^{-1})
Pu fraction = 0.2			
1.9998	-601	-108	
2	-463	30	449
2.0002	-336	157	242
			51
Pu fraction = 0.3			
1.9998	-589	-96	
2	-457	36	431
2.0002	-328	165	233
			39

Table 5.10 A comparison between values of tellurium potential in fuel – clad gap and the threshold tellurium potential required for the formation of $Cr_2Te_4O_{11}$ phase on SS 316 clad at 900 K at different O/M ratio of fuel $(U_mPu_{1-m})O_{2\pm x}$ and different plutonium content

O/M ratio (M= U_mPu_{1-m})	Oxygen potential (kJ mol^{-1})	Tellurium potential in fuel-clad gap (kJ mol^{-1})	Tellurium potential required for formation of $Cr_2Te_4O_{11}$ on SS 316 clad (kJ mol^{-1})
Pu fraction = 0.2			
1.9998	-601	-108	447
2	-463	30	257
2.0002	-336	157	82
Pu fraction = 0.3			
1.9998	-589	-96	431
2	-457	36	249
2.0002	-328	165	72

5.5 Conclusions

The standard Gibbs energy of formation of Cr_2TeO_6 was determined using EMF technique in this study and was compared with the values reported in the literature. Δ_fG^o Cr_2TeO_6 obtained from two different techniques (EMF and transpiration) is in excellent agreement with each other and also with those reported by other investigators. Δ_fG^o of $Cr_2Te_3O_9$(s) and $Cr_2Te_4O_{11}$(s) were reported for the first time in this study. Δ_fG^o $Cr_2Te_4O_{11}$(s) obtained using cell IV, V and VI matches very well.

The present study served to obtain thermodynamic information of various tellurates and tellurites in Cr-Te-O system. It also helped in deducing the possibility of formation of these phases in a nuclear reactor and in gaining better understanding of the clad corrosion. From the present study it can be concluded that formation of phases $Cr_2Te_3O_9$ and $Cr_2Te_4O_{11}$ might not occur under normal reactor operating conditions.

References

[1] Knacke O, Kubaschewski O, Hesselmann K. Thermochemical Properties of Inorganic Substances. 2nd ed. Germany: Springer-Verlag; 1991.

[2] Krishnan K, Mudher K D S, Rama Rao G A, Venugopal V. Structural and thermochemical studies on Cr_2TeO_6 and Fe_2TeO_6. J Alloys Compd. 2001; 316: 264-68.

[3] Krishnaiah M V, Sriramamurthi P. Computational model for the oxygen potentials of mixed uranium-plutonium oxide. J Am Ceram Soc. 1984; 67: 568-71.

[4] Azad M, Sreedharan O M, Gnanamoorthy J B. A novel determination of thermodynamic activities of metals in an AISI 316 stainless steel by a metastable EMF method. J Nucl Mater. 1987; 144: 94-104.

Chapter 6

Thermochemical studies on Cr_2TeO_6, Fe_2TeO_6, Ni_3TeO_6, $Ni_2Te_3O_8$ and $NiTe_2O_5$ using calorimetric technique

6

6.1 Introduction

Thermochemical studies on various tellurates and tellurides which can be formed due to possible attack of reactive fission product Te with clad components [1-4] using calorimetric technique are reported. The thermodynamic properties such as enthalpy and heat capacity of these compounds are required for reactor safety calculations. These data are essential for the performance analysis of fuel-clad assembly (fuel pin) under normal and off normal conditions [5]. Enthalpy increments of Cr_2TeO_6, Fe_2TeO_6, Ni_3TeO_6, $Ni_2Te_3O_8$ and $NiTe_2O_5$ have been measured for the first time and using measured enthalpy increments other thermodynamic parameters viz., heat capacity, entropy and free energy function (FEF) have been derived. ‘Third-law’ analysis [6] of vapour pressure data of Cr_2TeO_6, Fe_2TeO_6 and Ni_3TeO_6 has been carried out using these derived FEF and enthalpy of formation at 298 K of these compounds has been determined.

6.2 Calorimetric measurements

Drop calorimeter of isoperibol type [7, 8] was employed for the measurement of enthalpy increments of Cr_2TeO_6 and a high temperature inverse drop calorimeter (MHTC-96 supplied by M/s Setaram, France) was employed for the measurement of enthalpy increments of Fe_2TeO_6, Ni_3TeO_6, $Ni_2Te_3O_8$ and $NiTe_2O_5$. All the measurements were carried out in an atmosphere of ultra-high pure argon. The reference material employed in this study was the calorimetric standard, synthetic sapphire (α-alumina, SRM-720) obtained from NIST, USA.

6.2.1 Method of measurement

In a typical experiment in inverse drop calorimeter, carried out at an isothermal temperature T, five pairs of the samples of α-alumina reference (SRM 720) and sample pellet, each weighing about 150-200 mg, were dropped one after the other from the specimen chamber maintained at the ambient temperature in to the sample crucible kept in the calorimeter maintained at a constant temperature T, at an interval of 25 to 30 minutes. This time interval was found to be sufficient for the re-stabilization of both the temperature and the heat flow. The resultant output of the calorimetric detector was amplified and monitored continuously by using a high-impedance multimeter and the data were acquired using a computer. From the resultant heat flow signals corresponding to the α-alumina reference (Q_R) and the sample pellets (Q_S), the enthalpy increments $(H_T^0 - H_{298}^0)_S$ of samples were determined using the critically assessed enthalpy increment values $(H_T^0 - H_{298}^0)_R$ of the α-alumina reference reported in Ref. [9] :

$$(H_T^0 - H_{298}^0)_S = \frac{\int Q_S dt}{\int Q_R dt} \cdot \frac{M_S}{m_S} \cdot \frac{m_R}{M_R} \cdot (H_T^0 - H_{298}^0)_R \qquad (6.1)$$

where M_R and m_R are the molar mass and mass of the α-alumina reference material respectively and M_S and m_S are the molar mass and mass of the sample pellets respectively. The mean of the five heat flow values for the reference α-alumina and that for the sample pellets were used to compute the enthalpy increment at that temperature T. Further, two or three measurements were carried out for a given temperature and the mean value of the enthalpy increments from these runs at temperature, T were used for fitting.

The method employed in drop calorimeter for measurement of enthalpy increments was the same as mentioned above except the sample and reference are dropped from a desired temperature T to ambient temperature. The sample or reference materials were placed in a furnace at the desired temperature for a period of 25-30 mins to ensure temperature equilibration.

The measured enthalpy increments of Cr_2TeO_6, Fe_2TeO_6, Ni_3TeO_6, $Ni_2Te_3O_8$ and $NiTe_2O_5$ were fitted to 4-term polynomial in temperature of the following form by the least squares method:

$$H^o_T - H^o_{298K} = \mathrm{A}*T + \mathrm{B}*T^2 + \mathrm{C}*T^{-1} + \mathrm{D} \quad (6.2)$$

Heat capacity was obtained upon differentiation of the above equation over the given temperature range:

$$\mathrm{C}^0_\mathrm{p} = \mathrm{A} + 2*\mathrm{B}*T - \mathrm{C}*T^{-2} \quad (6.3)$$

6.2.2 Measurement of enthalpy increments of Cr_2TeO_6

The enthalpy increments of Cr_2TeO_6 were measured in the temperature 373-973 K by the drop calorimetric method. The measured enthalpy increments of Cr_2TeO_6 were fitted to a 4-term polynomial in temperature of the following form by the least-squares method:

$$H^o_T - H^o_{298K} \,/\, (\mathrm{kJ\ mol^{-1}})$$

$$= 0.20611\,(T/\mathrm{K}) + 0.34428 \times 10^{-5}\,(T/\mathrm{K})^2 + 0.96889 \times 10^3\,(\mathrm{K}/T) - 65.009 \quad (6.4)$$

Three constraints were used for fitting the data: (a) $H^o_T - H^o_{298K} = 0$ at 298 K (b) the derivative of the function at 298 K is equal to the value of heat capacity of Cr_2TeO_6 at 298 K, which was estimated from the values of $C^o_{p,298K}$ pertaining to Cr_2O_3 [10] and TeO_3 [11] by applying Neumann-Kopp's molar additivity rule and (c) the second derivative of the function at 298 K is equal to dC_p/dT of Cr_2TeO_6 at 298 K which was also estimated using $C^o_{p,298K}$ of Cr_2O_3 [10] and TeO_3 [11]. The value of S^o_{298K} of Cr_2TeO_6 was computed by combining the S^o_{298K} values of TeO_3 and Cr_2O_3 [10] using Neumann-Kopp's molar additivity rule. The S^o_{298K} of TeO_3 was estimated by combining S^o_{298K} of TeO_2 [10] and the difference between S^o_{298K} of A_2TeO_3 and A_2TeO_4 (where A = alkali metal) from Ref. [12]. The estimated standard deviation of this fit was 5.5 kJ mol^{-1}. The measured as well as fit values of the enthalpy increment are given in Table 6.1 and Fig. 6.1. The other thermodynamic parameters viz., heat capacity, entropy, free energy function derived from the enthalpy increment data using expression (6.4) are presented in Table 6.2. The heat capacity values obtained using enthalpy increment data are compared with those obtained using Neumann-Kopp's molar additivity rule in Fig. 6.2. The agreement between the present heat capacity data with those obtained using Neumann-Kopp's molar additivity rule in the temperature range 298 to 1000 K is within 5 % .

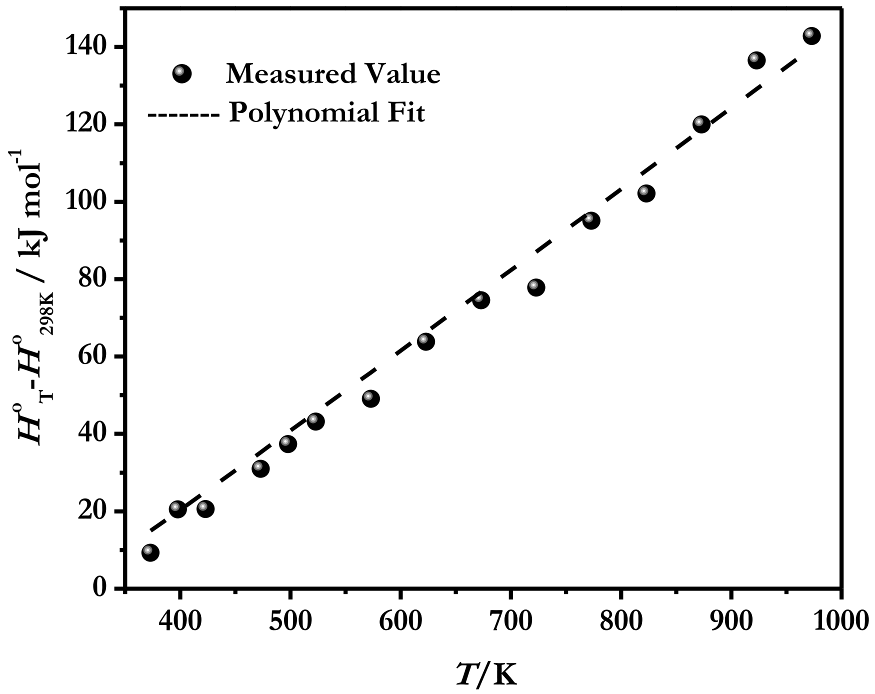

Fig. 6.1 Enthalpy increments of Cr_2TeO_6 (s)

Table 6.1 Experimentally measured enthalpy increments of Cr_2TeO_6

T / K	H^o_T - H^o_{298K} / (kJ mol^{-1})	
	Measured Value	**Fit Value**
373	9.28	14.95
398	20.43	20.00
423	20.52	25.08
473	30.99	35.30
498	37.32	40.44
523	43.15	45.58
573	49.03	55.92
623	63.81	66.29
673	74.48	76.71
723	77.81	87.15
773	95.04	97.63
823	102.11	108.13
873	119.91	118.66
923	136.47	129.22
973	142.83	139.80

Table 6.2 Thermodynamic functions of Cr_2TeO_6 derived from the values of enthalpy increment

T / K	H_T^o - H_{298K}^o/ (kJ mol^{-1})	C_p^o/(J K^{-1}mol^{-1})	S_T^o/(J K^{-1}mol^{-1})	$-\{(G_T^o - H_{298K}^o)/T\}$/ (J K^{-1}mol^{-1})
298	0	197.27	158.76	158.76
300	3.65	197.42	159.98	158.76
400	20.42	202.82	217.61	166.53
500	40.85	205.68	263.20	181.29
600	61.51	207.56	300.88	197.95
700	82.34	208.96	332.98	214.79
800	103.30	210.11	360.96	231.19
900	124.36	211.12	385.77	246.92
1000	145.52	212.03	408.06	261.93

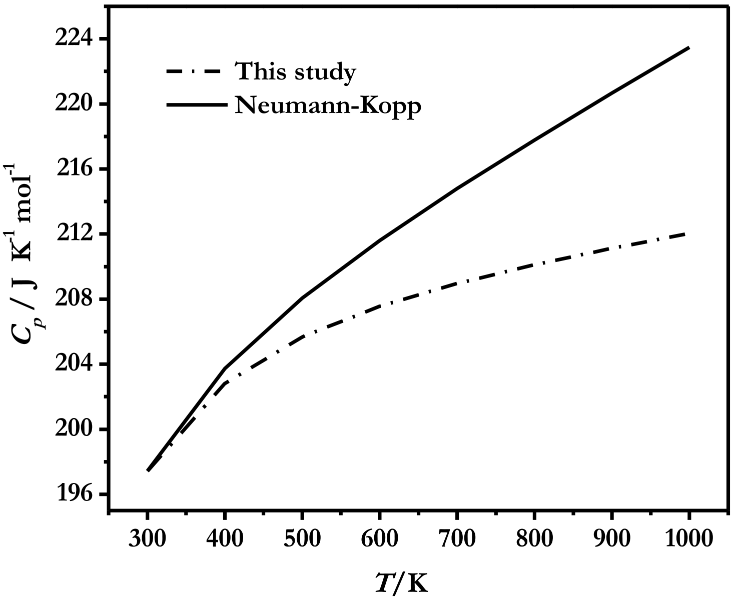

Fig. 6.2 Heat Capacity of Cr_2TeO_6 (s)

6.2.3 Measurement of enthalpy increments of Fe_2TeO_6

Enthalpy increments of Fe_2TeO_6 (s) were measured by drop calorimetry in the temperature range 483-1083 K. The accuracy of these enthalpy increment measurements was estimated to be ± 2 kJ mol^{-1}. The temperature of the sample was measured with an accuracy of ± 0.1 K.

The fit equation thus obtained for Fe_2TeO_6 (s) is given below:

$$(H^o_T - H^o_{298K}) / (\mathrm{J\ mol^{-1}})$$

$$= 213.036\,(T/K) + 25.462 \times 10^{-3}\,(T/K)^2 + 56.304 \times 10^{5}\,(K/T) - 84665 (483\text{-}1083\,K) \qquad (6.5)$$

The following constraints were used for fitting these data: (a) $(H^o_T - H^o_{298K}) = 0$ at 298 K and (b) the derivative of the function at 298 K is equal to the value of heat capacity at 298 K (164.88 J K^{-1} mol^{-1}) of Fe_2TeO_6 (s). The value of $C^o_{p,298K}$ pertaining to Fe_2TeO_6 (s) cited in Ref. [13] has been used in arriving at an expression for the temperature dependence of enthalpy increments of Fe_2TeO_6 (s). The S^o_{298K} value needed for the computation of the entropy as well as Gibbs energy functions of Fe_2TeO_6 (s) was estimated by combining the S^o_{298K} values of Fe_2O_3(s) [10] and TeO_3 (s) [14] using Neumann–Kopp's rule.

The standard error and the estimated standard deviation of the fit were 0.2% and 183 J mol^{-1} respectively. The measured values of the enthalpy increment obtained from the calorimetric experiments as well as the values computed by using the above fit equation at the experimental temperature are given in Table 6.3. The estimates of the other thermodynamic functions viz., heat capacity, entropy and Gibbs energy functions at regular intervals of temperature are given in Table 6.4. The temperature dependence of the enthalpy increments of Fe_2TeO_6 (s) along with the fit values as a function of 'T' are shown in Fig. 6.3. The temperature dependence of heat capacity values of Fe_2TeO_6 (s) computed from the fit equation is shown in Fig. 6.4. The values of heat capacity of Fe_2TeO_6 obtained in this study have been compared with those reported in Ref. 13 (Fig. 6.4).

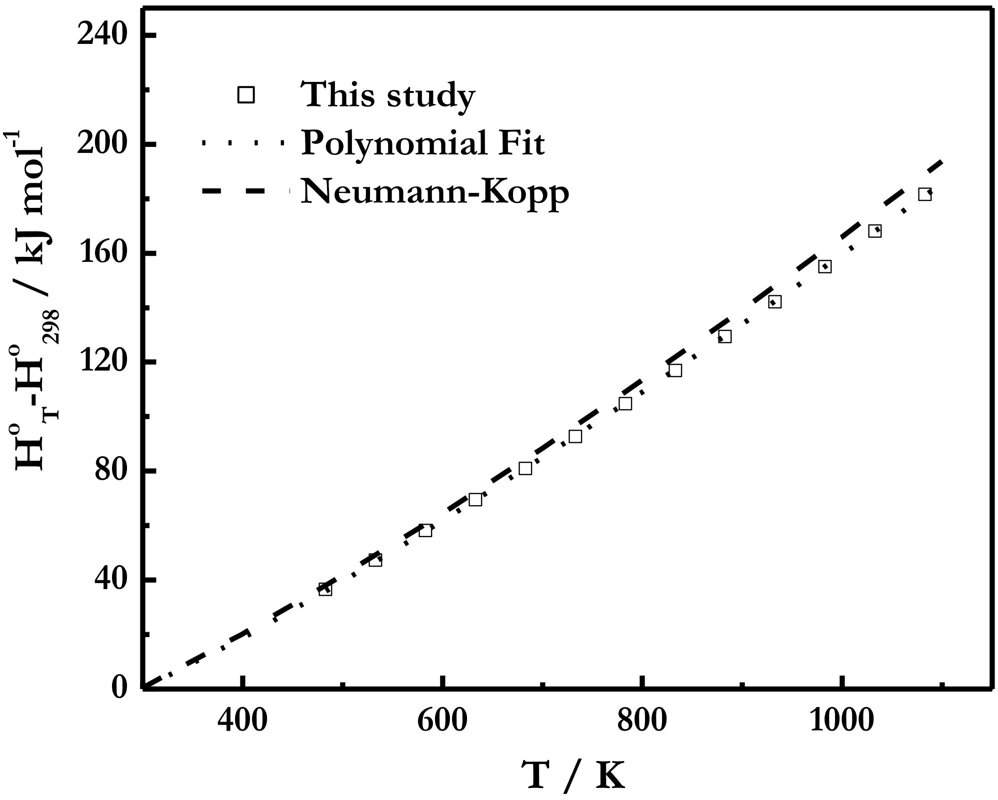

Fig. 6.3 Enthalpy increments pertaining to Fe_2TeO_6 (s)

Table 6.3 Enthalpy increments pertaining to Fe_2TeO_6 (s)

T / K	$H_T^o - H_{298}^o$ / J mol^{-1}	
	Measured	**Fit**
483	36517	35828
533	47216	46680
583	58199	57847
633	69490	69284
683	80956	80960
733	92709	92852
783	104703	104943
833	116931	117221
883	129391	129675
933	142080	142297
983	154995	155081
1033	168133	168022
1083	181495	1881116

Table 6.4 Thermodynamic functions pertaining to Fe_2TeO_6 (s)

T / K	H^o_T - H^o_{298} / J mol^{-1}	C^o_p / J K^{-1} mol^{-1}	S^o_T / J K^{-1} mol^{-1}	-(G_T- H^o_{298}) / T / J K^{-1} mol^{-1}
298	0	164.9	165.3	165.3
300	305.8	165.8	166.3	165.3
400	18699.8	198.2	219.0	172.2
500	39479.8	216.0	265.3	186.3
600	61707.4	228.0	305.8	203.0
700	84980.5	237.2	341.6	220.2
800	109098.0	245.0	373.8	237.4
900	133948.2	252.0	403.1	254.2
1000	159464.0	258.3	430.0	270.5
1100	185602.8	264.4	454.9	286.1
1200	212336.1	270.2	478.1	301.2

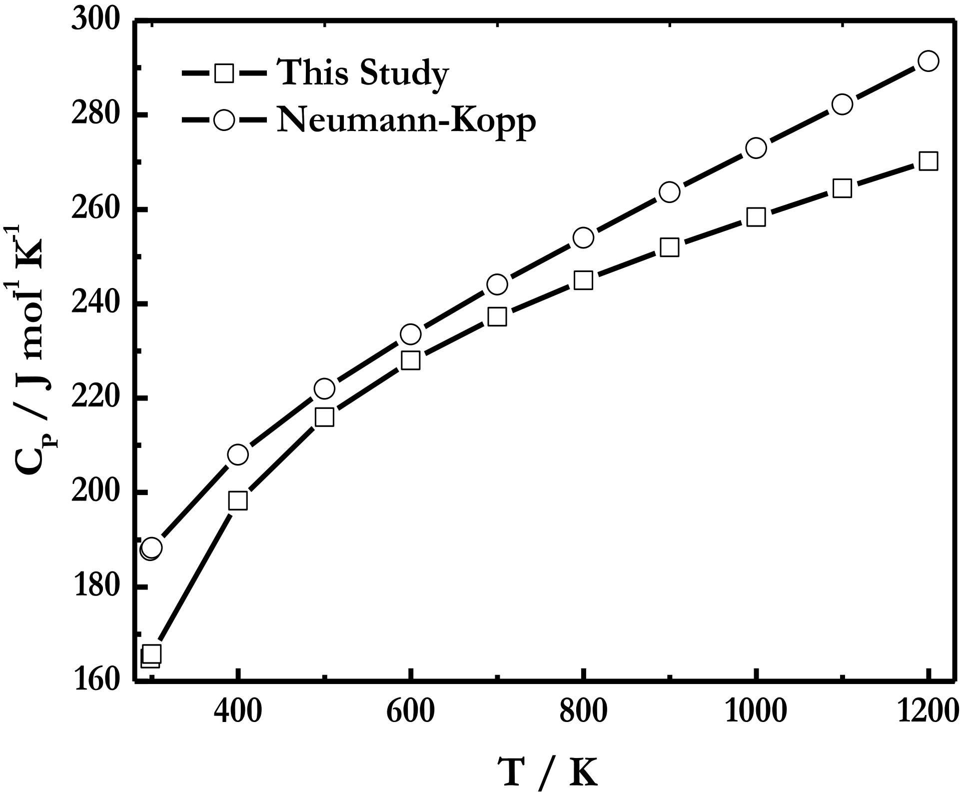

Fig. 6.4 Temperature dependence of C_p values derived from the measured values of the enthalpy increments pertaining to Fe_2TeO_6 (s)

6.2.4 Measurement of enthalpy increments of Ni_3TeO_6 (s), $Ni_2Te_3O_8$ (s) and $NiTe_2O_5$(s)

Enthalpy increments of Ni_3TeO_6 (s), $Ni_2Te_3O_8$(s) and $NiTe_2O_5$(s) were measured by "inverse drop calorimetry" technique in the temperature range 483-1087 K. The fit equations thus obtained for Ni_3TeO_6 (s), $Ni_2Te_3O_8$ (s) and $NiTe_2O_5$ (s) are given below:

$$(H^o_T - H^o_{298K}) / (\text{J mol}^{-1}) =$$

$$247.704(T/K) + 4.397\times10^{-3}(T/K)^2 + 52.817\times10^5(K/T) - 91959 \qquad (6.6)$$

$$(H^o_T - H^o_{298K}) / (\text{J mol}^{-1}) =$$

$$318.809(T/K) + 16.932\times10^{-3}(T/K)^2 + 43.278\times10^5(K/T) - 111073 \qquad (6.7)$$

$$(H^o_T - H^o_{298K}) / (\text{J mol}^{-1}) =$$

$$156.312(T/K) + 27.773x10^{-3}(T/K)^2 + 1.621x10^5(K/T) - 49617 \qquad (6.8)$$

The following constraints were used for fitting the data: (a) $H^0_T - H^0_{298}$ = 0 at 298 K and (b) the derivative of the function at 298 K is equal to the value of heat capacity of Ni_3TeO_6 (s), $Ni_2Te_3O_8$ (s) and $NiTe_2O_5$ (s) at 298 K (190.91, 280.22 and 171.05 J K^{-1} mol^{-1} respectively). The value of $C^0_{p,298}$ pertaining to Ni_3TeO_6 (s) cited in Ref. [13] has been used. For $Ni_2Te_3O_8$ (s) and $NiTe_2O_5$ (s), $C^0_{p,298}$was estimated from the values of $C^0_{p,298}$ pertaining to NiO (s) and TeO_2 (s) [10] by applying Neuman-Kopp's molar additivity rule. The S^0_{298} value needed for the computation of the entropy and Gibbs energy functions of Ni_3TeO_6 (s) was taken from Ref. [13]. For $Ni_2Te_3O_8$ (s) and $NiTe_2O_5$ (s), S^0_{298} values were estimated by combining S^0_{298} values of NiO (s) and TeO_2 (s) [10] by applying Neuman-Kopp's molar additivity rule. The standard error of the fit is 3-4% and the estimate of the standard deviation for the fit is 4-6 kJ mol^{-1}. The temperature dependence of heat capacity of Ni_3TeO_6 (s), $Ni_2Te_3O_8$ (s) and $NiTe_2O_5$ (s) derived from their respective fitted enthalpy increment equations (6.9), (6.10), (6.11) are given below:

$$C^0_p\ (Ni_3TeO_6, (s)) / (J\ mol^{-1}) = 247.704 + 8.794\ x10^{-3}(T/K) - 52.817x10^5(K/T)^2 \qquad (6.9)$$

$$C^0_p\ (Ni_2Te_3O_8, (s)) / (J\ mol^{-1}) = 318.809 + 33.864\ x10^{-3}(T/K) - 43.278x10^5(K/T)^2 \qquad (6.10)$$

$$C^0_p\ (NiTe_2O_5, (s)) / (J\ mol^{-1}) = 156.312 + 55.546\ x10^{-3}(T/K) - 1.621x10^5(K/T)^2 \qquad (6.11)$$

The measured values of the enthalpy increment obtained from the calorimetric experiments as well as the values computed by using the above fit equations at the experimental temperatures are given in Tables 6.5, 6.6 and 6.7. The estimates of the other thermodynamic functions, viz. heat capacity, entropy and Gibbs energy functions at regular intervals of temperature are also given in Tables 6.5, 6.6 and 6.7. The temperature dependence of the enthalpy increments of Ni_3TeO_6 (s), $Ni_2Te_3O_8$ (s) and $NiTe_2O_5$ (s) along with the fit values as a function of temperature is shown in Fig. 6.5. The temperature dependence of heat capacity values of Ni_3TeO_6 (s), $Ni_2Te_3O_8$ (s) and $NiTe_2O_5$ (s) obtained in this study is shown in Fig. 6.6. The computed values of heat capacity of Ni_3TeO_6 (s), $Ni_2Te_3O_8$ (s) and $NiTe_2O_5$ (s) have also been compared with those reported in Ref. [13] in Fig. 6.6. The variation between C_p values of $Ni_2Te_3O_8$ (s) obtained in the present study and those reported in Ref. [13] is large compared to the values of Ni_3TeO_6 (s) for which the difference is large only above 800 K. C_p values of $NiTe_2O_5$ (s) obtained in this study matches very well with that of Ref. [13].

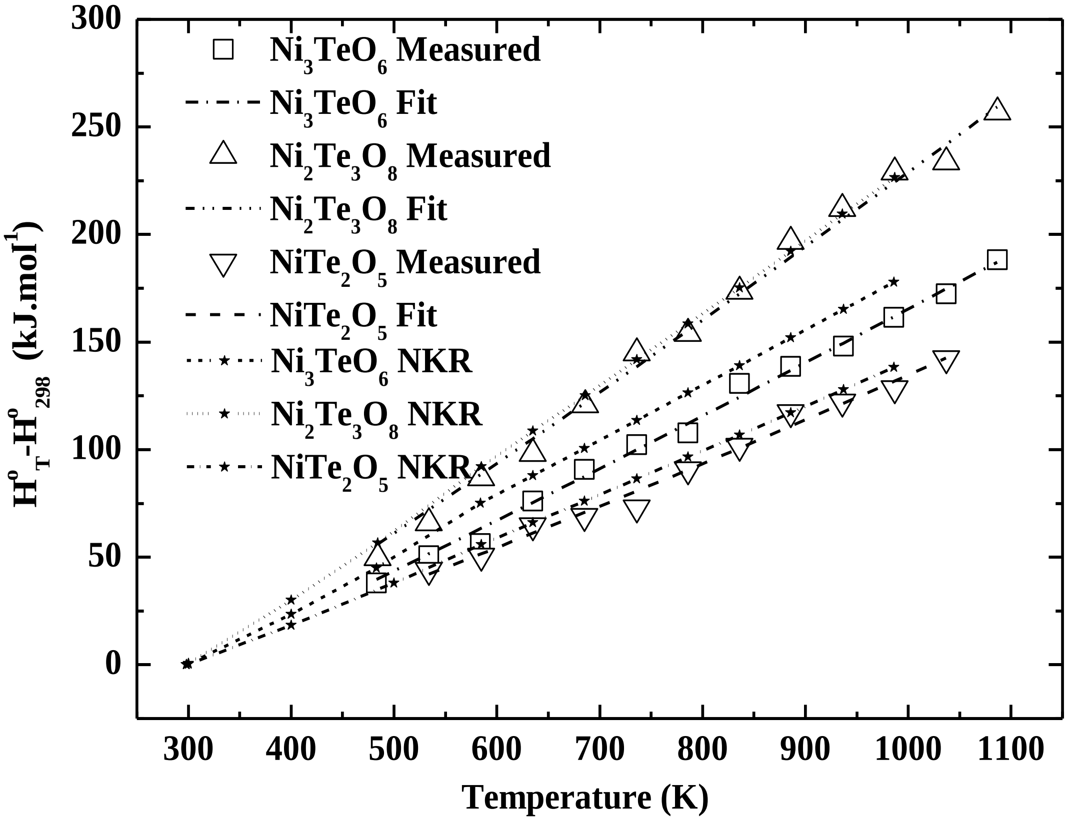

Fig. 6.5 Temperature dependence of the enthalpy increments of Ni_3TeO_6 (s), $Ni_2Te_3O_8$ (s) and $NiTe_2O_5$ (s)

Table 6.5 Thermodynamic functions of Ni_3TeO_6

T/K	$H_T^o - H_{298}^o$/kJ mol^{-1}		T	$H_T^o - H_{298}^o$	C_P^o	S_T^o	$-(G_T^o - H_{298}^o)/T$
	Measured	Fit	K	kJ mol^{-1}	J K^{-1} mol^{-1}		
483	38.039	39.643	298	0	190.910	179.900	179.900
534	50.611	51.459	300	0.354	191.657	181.083	179.904
584	56.232	63.244	400	21.031	218.211	240.385	187.809
635	76.017	75.424	500	43.556	230.974	290.596	203.484
685	90.738	87.492	600	67.050	238.309	333.410	221.661
736	102.189	99.909	700	91.134	243.081	370.527	240.335
786	107.789	112.172	800	115.621	246.487	403.219	258.693
836	130.633	124.512	900	140.405	249.098	432.408	276.402
886	138.564	136.920	1000	165.424	251.216	458.766	293.342
937	147.999	149.637	1100	190.638	253.012	482.796	309.489
986	161.453	161.909					
1037	172.371	174.732					
1087	188.255	187.350					

Table 6.6 Thermodynamic functions of $Ni_2Te_3O_8$

T/K	$H_T^o - H_{298}^o$/kJ mol^{-1} Measured	$H_T^o - H_{298}^o$/kJ mol^{-1} Fit	T K	$H_T^o - H_{298}^o$ kJ mol^{-1}	C_P^o J K^{-1} mol^{-1}	S_T^o J K^{-1} mol^{-1}	$-(G_T^o - H_{298}^o)/T$ J K^{-1} mol^{-1}
484	49.589	56.138	298	0	280.220	298.910	298.910
534	65.825	72.103	300	0.519	280.881	300.645	298.915
585	86.696	88.622	400	29.979	305.306	385.228	310.282
635	98.182	105.013	500	61.219	318.430	454.886	332.447
686	120.766	121.906	600	93.520	327.106	513.754	357.886
736	144.907	138.622	700	126.572	333.681	564.690	383.873
786	153.933	155.477	800	169.220	339.138	609.612	409.337
836	173.596	172.461	900	194.378	343.944	649.839	433.864
886	196.737	189.567	1000	228.995	348.345	686.308	457.313
936	211.938	206.789	1100	264.038	352.483	719.705	479.670
987	228.965	224.470					
1037	233.664	241.913					
1087	256.748	259.460					

Table 6.7 Thermodynamic functions of $NiTe_2O_5$

T/K	$H^o_T - H^o_{298}$/kJ mol^{-1}		T	$H^o_T - H^o_{298}$	C^o_P	S^o_T	$-(G^o_T - H^o_{298})/T$
	Measured	Fit	K	kJ mol^{-1}	J K^{-1} mol^{-1}		
534	43.966	42.077	298	0	171.050	186.610	186.610
585	50.603	51.607	300	0.317	171.175	187.668	186.613
635	64.826	61.095	400	17.757	177.518	237.797	193.405
685	69.030	70.725	500	35.807	183.437	278.050	206.437
736	73.109	80.693	600	54.439	189.189	312.004	221.273
786	90.714	90.609	700	73.642	194.863	341.595	236.392
836	101.684	100.664	800	93.410	200.495	367.983	251.221
886	117.346	110.860	900	113.740	206.103	391.922	265.544
936	122.154	121.196	1000	134.631	211.696	413.927	279.296
987	128.511	131.883	1100	156.079	217.278	434.365	292.475
1037	142.338	142.501					

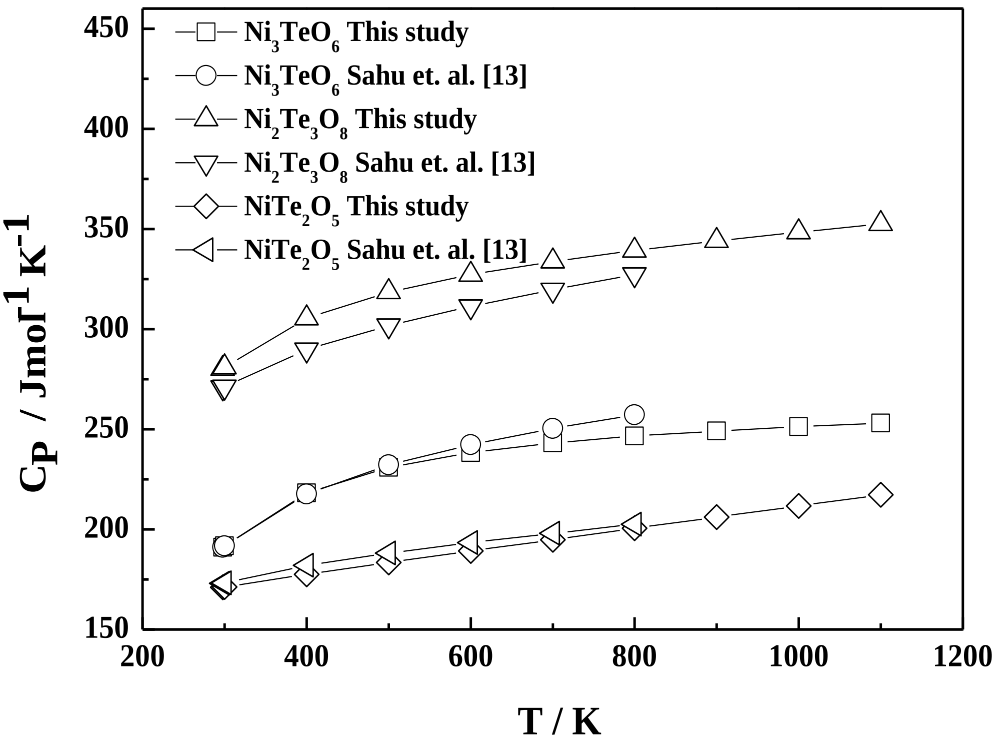

Fig. 6.6 Comparison of temperature dependence of the C_P values of Ni_3TeO_6 (s), $Ni_2Te_3O_8$ (s) and $NiTe_2O_5$ (s) derived from the present measured values of enthalpy increments with Sahu et al. [13]

6.3 Third-law analysis of vapour pressure data

A "third-law" analysis of the data on the vapour pressure of TeO_2 (g) over the phase mixture (i) Cr_2O_3 (s) + Cr_2TeO_6 (s) (ii) Fe_2O_3 (s) + Fe_2TeO_6 (s) (iii) NiO (s) + Ni_3TeO_6 (s) measured by the transpiration technique (Chapter – 4) was carried out in order to assess the temperature dependent systematic errors. The change in free energy function (Δfef) for the formation of (i) Cr_2TeO_6 (ii) Fe_2TeO_6 and (iii) Ni_3TeO_6 was calculated using the free energy functions derived from the present drop calorimetric data (Table 6.2, 6.4, 6.5) along with the free energy functions of the elements (i) Cr, Te and O_2

(ii) Fe, Te and O_2 and (iii) Ni, Te and O_2 [16]. For the computation of $\Delta H^o_{f,298K}$ the following expression was used.

$$\Delta H^o_{f,298K} = \Delta G^o_f - T\ (\Delta fef) \qquad (6.12)$$

The Δfef values extrapolated at the experimental temperatures were combined with the values of ΔG^o_f of Cr_2TeO_6, Fe_2TeO_6 and Ni_3TeO_6 in order to obtain their $\Delta H^o_{f,298K}$ corresponding to each experimental measurement. The dependence of $\Delta H^o_{f,298K}$ on temperature for Cr_2TeO_6, Fe_2TeO_6 and Ni_3TeO_6 is shown in Fig. 6.7, 6.8 and 6.9 respectively. The mean value of $\Delta H^o_{f,298K}$ was found to be -1636.9 ± 0.8 / (kJ mol^{-1}) for Cr_2TeO_6, -1318.1 ± 0.9 / kJ mol^{-1} for Fe_2TeO_6 and -1265.1 ± 1.5 kJ mol^{-1} for $Ni_3TeO_6(s)$. The scatter in the values of $\Delta H^o_{f,298K}$ around the mean value confirms that the vapour pressure measurements are free from temperature dependent systematic errors.

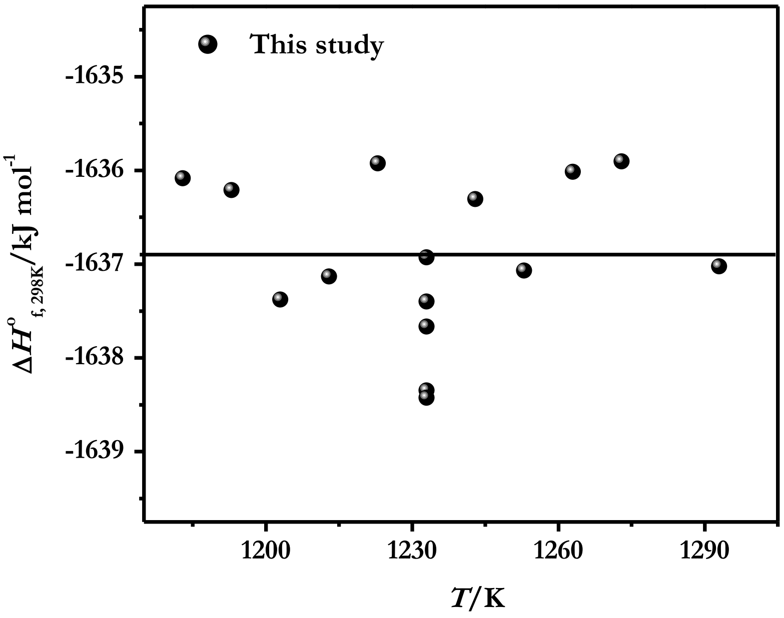

Fig. 6.7 A "third-law" analysis plot ($\Delta_f H^o_{298K}$(Cr_2TeO_6, s) vs T) of the data obtained from transpiration experiments for $Cr_2TeO_6(s)$

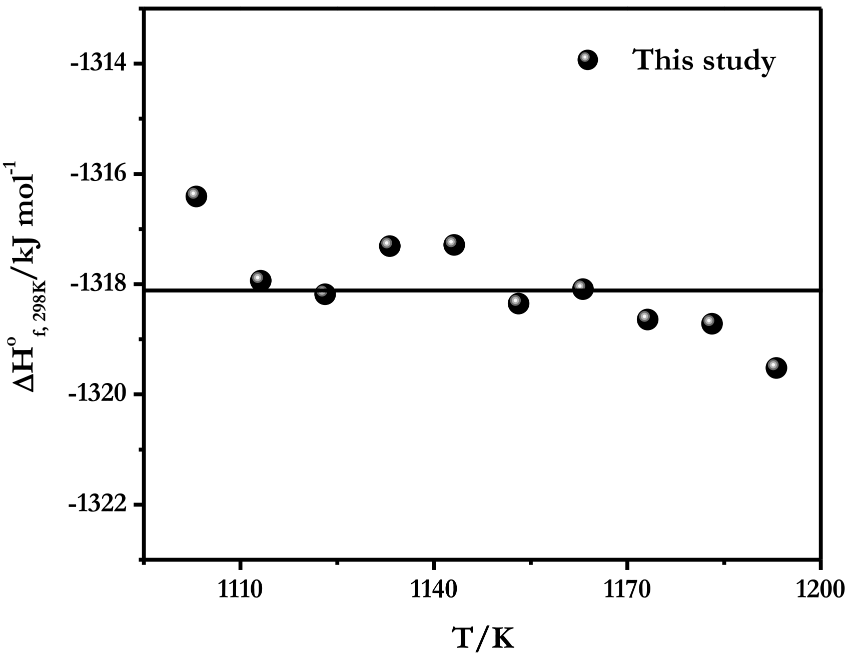

Fig. 6.8 A "third-law" analysis plot ($\Delta_f H^o_{298K}$(Fe_2TeO_6, s) vs T) of the data obtained from transpiration experiments for Fe_2TeO_6(s)

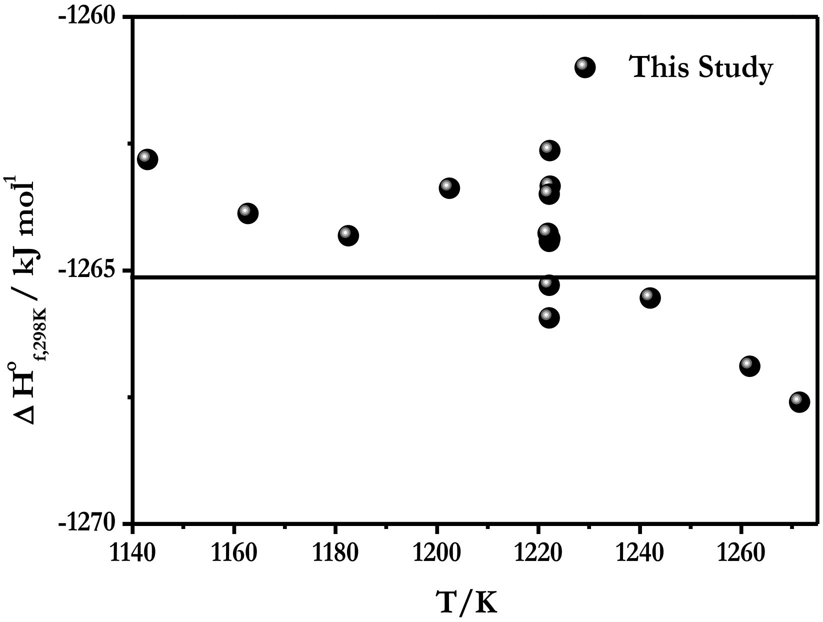

Fig. 6.9 A "third-law" analysis plot ($\Delta_f H^o_{298K}$(Ni_3TeO_6, s) vs T) of the data obtained from transpiration experiments for Ni_3TeO_6(s)

6.4 Conclusions

Enthalpy increments of Cr_2TeO_6, Fe_2TeO_6, Ni_3TeO_6, $Ni_2Te_3O_8$ and $NiTe_2O_5$ have been measured for the first time and from the measured enthalpy increment values other thermodynamic parameters viz., heat capacity, entropy and free energy function (FEF) were derived. From the derived FEF, $\Delta H^{o}_{f,298K}$ was computed from the 'third-law' analysis of vapour pressure data of Cr_2TeO_6, Fe_2TeO_6, Ni_3TeO_6 measured in this study. The scatter in the values of $\Delta H^{o}_{f,298K}$ around the mean value confirmed that the vapour pressure measurements were free from temperature dependent systematic errors.

References

[1] Kleykamp H. Chemical States of the Fission Products in Oxide Fuels. J Nucl Mater. 1985; 131: 221-46.

[2] Adamson M G, Aitken E A, Lindemer T B. Chemical thermodynamics of Cs and Te fission product interactions in irradiated LMFBR mixed-oxide fuel pins. J Nucl Mater. 1985; 130: 375-92.

[3] Chattopadhyay G, Juneja J M. A thermodynamic database for tellurium bearing systems relevant to nuclear technology. J Nucl Mater. 1993; 202: 10-28.

[4] Cordfunke E H P, Konings R J M. Chemical Interaction in Water Cooled Nuclear Fuel: A Thermochemical Approach. J Nucl Mater. 1988; 152: 301-09.

[5] Manideepa Ali, "Thermochemical studies on some alloys and refractory oxides of importance in nuclear technology" Ph.D. Thesis, University of Mumbai (2003).

[6] Cater E D: in Techniques of Metals Research, R.F. Bunshah, ed., vol. IV, Physiochemical Measurements in Metals Research, parts 1 and 2, R.A. Rapp, ed., Interscience Publishers, New York, NY, 1970.

[7] Krishnaiah M V. Ph. D. Thesis, University of Madras, 1999.

[8] Babu R, Kandan R, Jena H, Kutty K V G, Nagarajan K. Calorimetric investigations on cubic $BaTiO_3$ and $Ba_{0.9}Nd_{0.1}TiO_3$ systems. J Alloys Compd. 2010; 506: 565-68.

[9] Synthetic Sapphire Al_2O_3, Certificate of Standard Reference Materials, SRM 720, 1982. (National Bureau of Standards, U.S. Department of Commerce, Washington, DC20234, USA).

[10] Knacke O, Kubaschewski O, Hesselmann K. Thermochemical Properties of Inorganic Substances. 2nd ed. Germany: Springer-Verlag; 1991.

[11] Aggarwal R, Singh Z. Enthalpy increments of $Ba_2Te_3O_8$(s) and $Ba_3Te_2O_9$(s) compounds. J Alloys Compd. 2006; 414: 230-34.

[12] Lindemer T B, Bessman T M. Thermodynamic review and calculations—alkali-metal oxide systems with nuclear fuels, fission products, and structural materials. J. Nucl. Mater. 1981; 100: 178-226.

[13] Sahu M, Rawat D, Vats B G, Saxena M K, Dash S. Thermo physico-chemical investigations on A–Te–O (A = Cr, Fe, Ni) system. Thermochim Acta. 2014; 585: 50-62.

[14] Pankajavalli R, Jain A, Babu R, Anthonysamy S, Ananthasivan K, Ganesan V, Nagarajan K. Thermodynamic characterization of lanthanum tellurate. J. Nucl. Mater. 2010; 397: 116-21.

[15] Venkata Krishnan R, Nagarajan K. Evaluation of heat capacity measurements by temperature-modulated differential scanning calorimetry. J Therm Anal Calorim. 2010; 102: 1135-40.

[16] Hultgren R, Desai P D, Hawkins D T, Gleiser M, Kelley K K, Selected Values of the Thermodynamic Properties of Elements. Ohio, USA: American Society for Metals, Metals Park; 1973.

Chapter 7

Kinetics of formation of La_2TeO_6

7

7.1 Introduction

Rare earths and tellurium are among the major fission products (fp) formed during the burn up of a fast reactor fuel [1, 2]. Hence, there is a possibility of formation of lanthanum tellurate (La_2TeO_6) due to interaction between fission products La and Te. The standard Gibbs energy of formation of La_2TeO_6 was determined by using thermogravimetry (TG) based transpiration technique by Pankajavalli et. al. [3] in our laboratory at Indira Gandhi Centre for Atomic Research (IGCAR), India. Data on the kinetics of formation of La_2TeO_6 are useful in evaluating the behaviour of the fuel under normal and accidental reactor operating conditions. These data will be of use for the basic understanding of formation of lanthanum tellurate also. Hence studies were carried out to evaluate the data on the kinetics of formation of La_2TeO_6 for the first time.

7.2 Kinetics of formation of La_2TeO_6

The kinetics of formation of La_2TeO_6 was studied by employing a Theromogravimetry-Differential Thermal Analysis (TG-DTA) apparatus (SETSYS Evolution 16/18, obtained from M/s Setaram, France). All details regarding this instrument and experiment have been given in experimental section (Chapter 2).

7.2.1 Formation of La_2TeO_6

La_2TeO_6 was formed by heating a homogeneous mixture of $La(OH)_3$ and TeO_2 (2:1 mole ratio) in a flowing stream of oxygen from room temperature to 1203 K. The TG curve for the decomposition of $La(OH)_3$ showed two weight-loss steps corresponding to the chemical reaction represented by Eqn. 7.1 and 7.2

$$La(OH)_3 \xrightarrow{558\ K} LaO(OH) + H_2O \qquad (7.1)$$

$$2LaO(OH) \xrightarrow{738K} La_2O_3 + H_2O \qquad (7.2)$$

These results were in accordance with the results reported earlier [4, 5]. La_2O_3 thus formed in-situ reacts with TeO_2 in the presence of O_2 to form La_2TeO_6. It has been ascertained through the TG experiments and subsequent XRD characterization of the reaction products that the formation of La_2TeO_6 takes place only in the temperature range 1023-1203 K under the present experimental conditions. Hence experiments to study the kinetics of formation of La_2TeO_6 were carried out in the temperature range 1023 to 1203 K at different heating rates of 2, 3, 5, 10, 15 K min^{-1}. X-ray diffraction patterns of the products obtained from experiments with heating rates of 2 and 15 K min^{-1} are shown in Fig. 7.1. The XRD patterns showed the presence of only La_2TeO_6 (JCPDS file no. 78-0998). In order to elucidate the nature of the formation reaction, isothermal experiments were carried out at 1025 K and 1045 K. X-ray diffraction pattern of the product obtained after heat treatment of the reaction mixture at 1025 K (Fig. 7.2 (a)) showed the presence of La_2O_3 and TeO_2 in addition to La_2TeO_6. XRD patterns of the sample obtained by heating $La(OH)_3$ and TeO_2 mixture isothermally at 1073 K for 16 h (Fig. 7.2 (b)) and 1123 K for 12 h (Fig. 7.2 (c)) showed the presence of La_2TeO_6 only. This was further confirmed by a number of XRD patterns of the products obtained by heating the homogeneous mixture of $La(OH)_3$ and TeO_2 in a tubular furnace at 1123 K for 12 h and 24 h in an independent set of experiments. It is clear from these experiments that both the temperature and reaction time influence the formation of La_2TeO_6 under isothermal conditions.

7.2.2 Morphology

A typical SEM micrograph of the product obtained after heating the reaction mixture at 1123 K for 12 h, as shown in Fig. 7.3, indicates the product to be highly porous. It is probable that diffusion of oxygen through the product layer plays an important role in deciding the kinetics of this formation reaction. However factors such as melting of TeO_2 at these temperatures would influence the rate of diffusion of oxygen through the product layer.

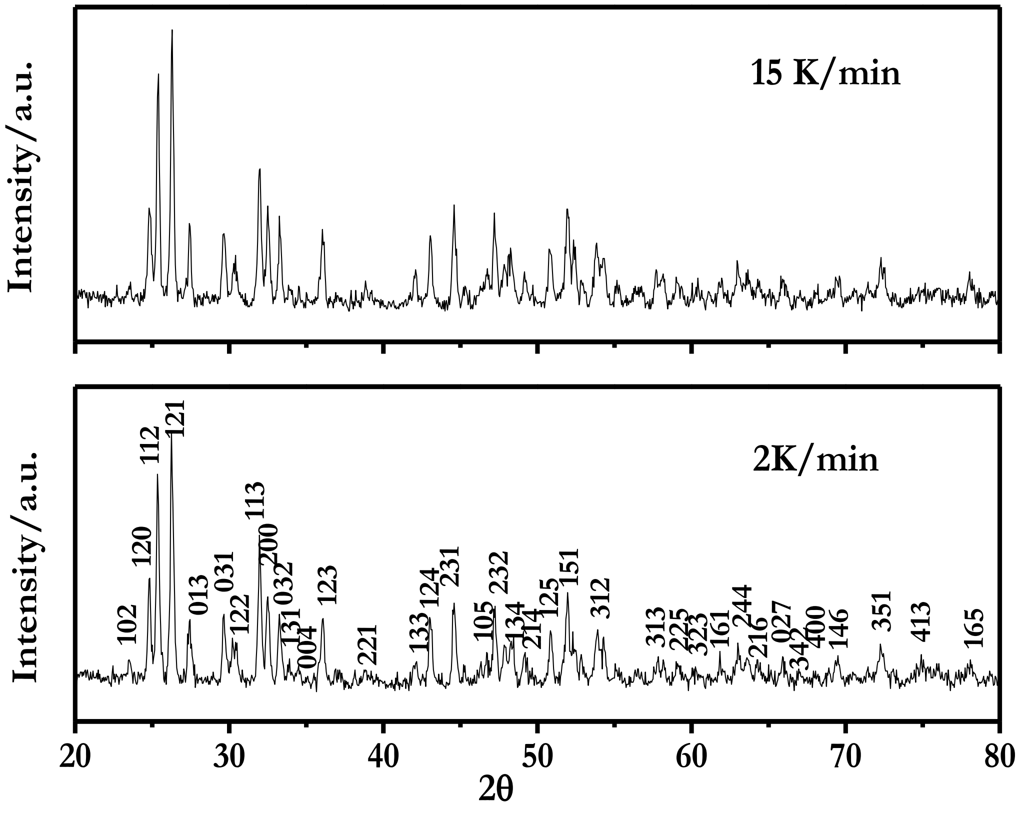

Fig. 7.1 XRD patterns of the products obtained after non-isothermal experiments at heating rates (a) 2 K min^{-1} (b) 15 K min^{-1}

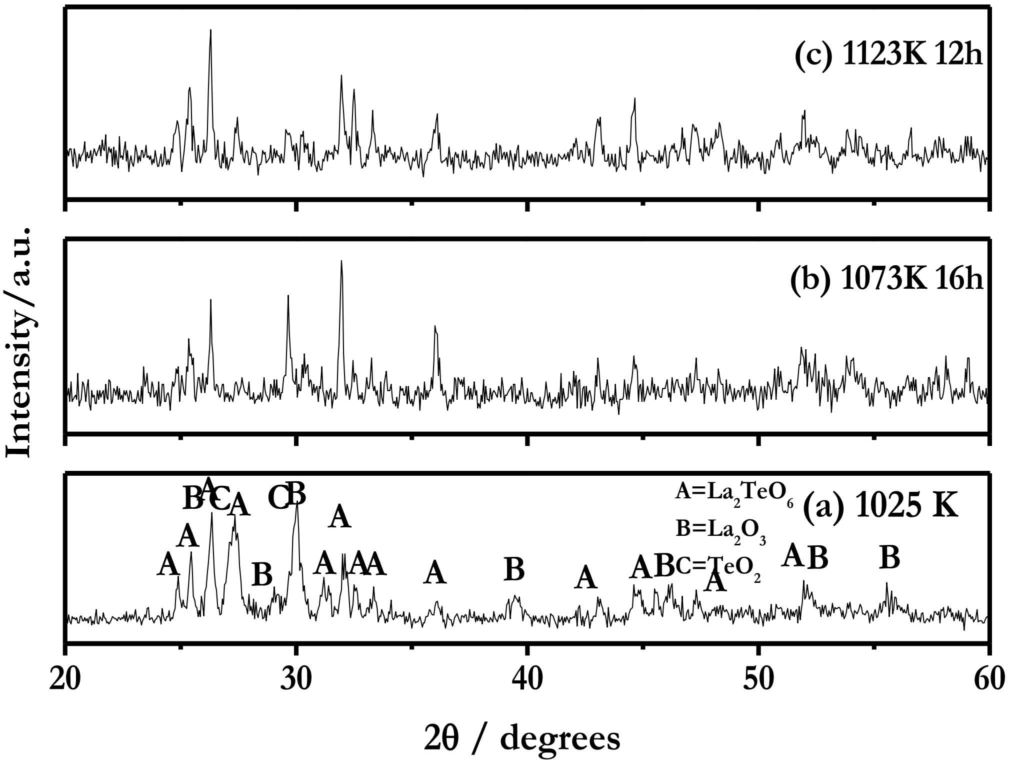

Fig. 7.2 XRD patterns of the products obtained after isothermal experiments at temperatures (a) 1025 K (b) 1073 K (c) 1123 K

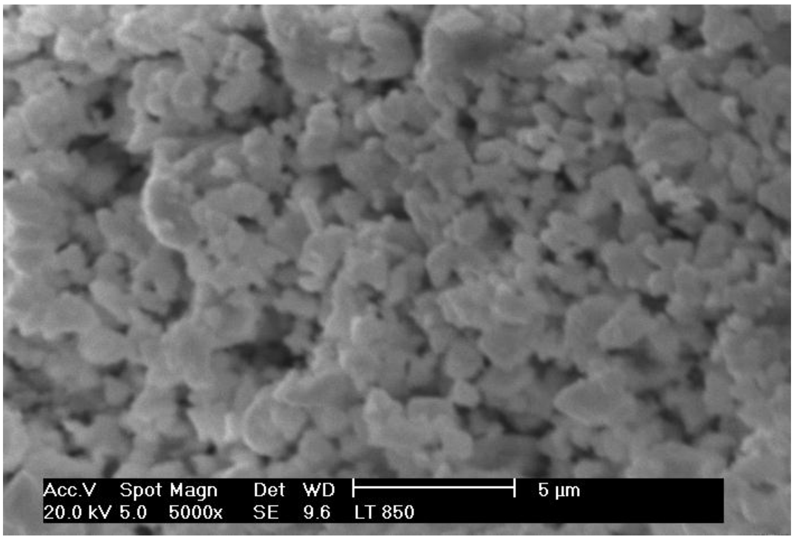

Fig. 7.3 SEM micrograph of product obtained after isothermal heating at 1123 K for 12 h

7.2.2 Thermal analysis of the formation of lanthanum tellurate

Typical thermal analysis curves [TGA, DTG and DTA] of the sample (homogeneous mixture of $La(OH)_3$ and TeO_2) heated from 1023 to 1203 K at a heating rate of 10 K min^{-1} are shown in Fig. 7.4. TGA curve shows that there is no measurable weight-gain beyond 1203 K which indicates completion of the reaction (Eqn. 7.3).

$$La_2O_3 + TeO_2 + \frac{1}{2} O_2 \rightarrow La_2TeO_6 \qquad (7.3)$$

The multi-step nature of this reaction is clear from DTG curve which is not much clear from TG curve. The same is clear from DTA curve which shows the presence of multiple exothermic peaks.

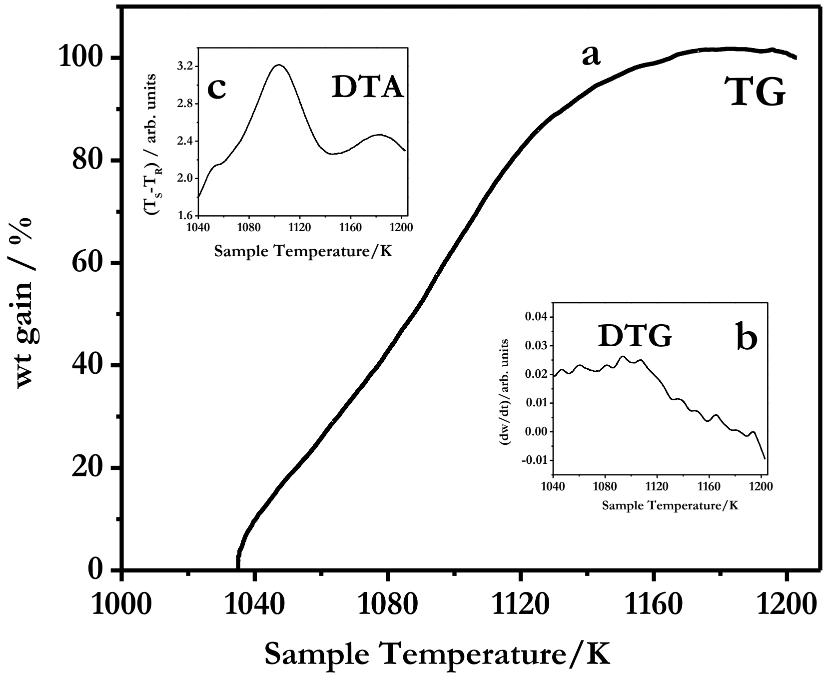

Fig. 7.4 Thermal analysis curves for the formation of La_2TeO_6 (a) Thermogravimetry curve (b) derivative thermogravimetry curve (c) differential thermal analysis curve

For the purpose of calculation, the weight obtained after the completion of the TG experiment was taken as the final weight gain w_T for the formation reaction as explained in Ref. [6]. The fraction of formation of La_2TeO_6, ‘α’, was calculated by the relation

$$\alpha = \frac{w_t - w_i}{w_T - w_i} \qquad (7.4)$$

where w_i, w_T and w_t are weights corresponding to initial, final and intermediate weight respectively.

7.3 Kinetic analysis of the formation of lanthanum tellurate by isoconversional method

7.3.1 Non-isothermal kinetics

The variation of α with temperature at various heating rates is shown in Fig. 7.5. The rate of any heterogeneous reaction under non-isothermal condition can be expressed as [7, 8]

$$\frac{d\alpha}{dt} = k(T)\, f(\alpha) \qquad (7.5)$$

where f(α) is the conversion function which is dependent on the mechanism of the reaction, T is the absolute temperature and k(T) is the temperature dependent Arrhenius rate constant.

$$k(T) = A \exp\left[\frac{-E_a}{RT}\right] \qquad (7.6)$$

where A is the pre-exponential factor, E_a is the activation energy of the reaction and R is the universal gas constant.

Combining Eqn. (7.5) and (7.6), the integral form of Eqn. (7.5) can be expressed as

$$g(\alpha) \cong \int_0^{\alpha} \frac{d\alpha}{f(\alpha)} = \int_0^{T} \frac{A}{\beta} \exp\left[\frac{-E_a}{RT}\right] dT \qquad (7.7)$$

where g(α) is the integral form of f(α) and β (= dT/dt) is the heating rate.

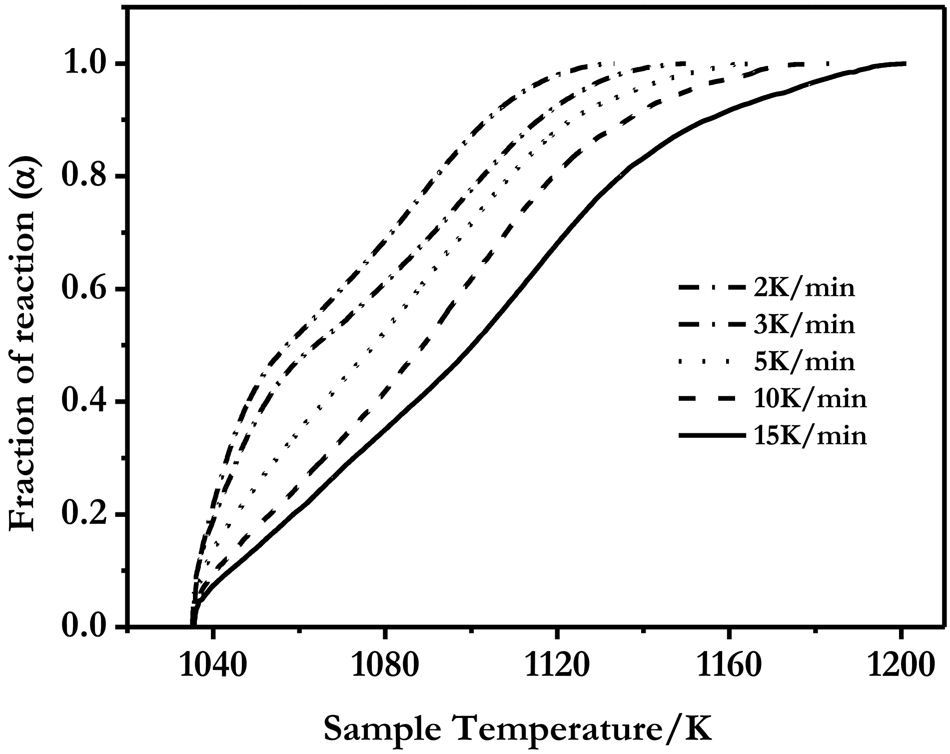

Fig. 7.5 A plot of fraction of reaction vs sample temperature at various heating rates

Kinetic analyses of TGA data by integral methods are generally considered to be more accurate and precise [9]. The dependence of activation energy as a function of extent of reaction can be obtained by model-free isoconversional method. All isoconversional methods are based on the principle which states that the transformation rate, $d\alpha / dt$, at constant extent of conversion is only a function of temperature and f(α) is independent of the heating rates [10 - 12]. If the Arrhenius equation is applicable, the following relation can be stated:

$$\left[\frac{d\ln(d\alpha/dt)}{dT^{-1}}\right]_{\alpha} = -\frac{E_\alpha}{R} \tag{7.8}$$

where the subscript α indicates isoconversional values, $(\alpha_i)_1 = (\alpha_i)_2 = \ldots(\alpha_i)_n$ for each one of the experiments (1,2,…n) and at each temperature. This criterion allows an estimation of E_α without the assumption of any reaction model and hence allows one to explore multi step kinetics [13, 14]. Kissinger-Akahira-Sunose (KAS) (also termed as generalized Kissinger method) is one of the most widely used integral isoconversional methods [15] for obtaining E_α with good accuracy. It takes the form

$$\ln\frac{\beta_i}{T_{\alpha,i}^2} = const - \frac{E_\alpha}{RT_{\alpha,i}} \tag{7.9}$$

where the subscript 'i' denotes various heating rates. The slope of the plot $\ln \beta_i / T_{\alpha,i}^2$ vs $1/T_{\alpha,i}$ gives the value of the effective activation energy E_α [16]. The plot of E_α as a function of α is shown in Fig. 7.6.

This plot reveals the complex nature of the reaction which indicates typical behaviour of a competitive reaction. The variation of effective activation energy E_α with α is divided into three regions. For the first region i.e. α = 0 to 0.44 E_α decreases with increasing α which shows that the rate of formation of La_2TeO_6 increases with increasing temperature. During the second stage (α=0.44 to 0.74) E_α increases with increasing α which indicates that the rate of the reaction decreases with temperature. In the third region (α = 0.74 to 1) E_α decreases again with increasing α. The formation of La_2TeO_6 involves diffusion of oxygen through the reaction mixture which leads to the formation and growth of La_2TeO_6 nuclei. In the first region nucleation and diffusion may be the dominating processes. In the second region, due to the occurrence of many parallel reactions (e.g. diffusion of oxygen, nucleation and growth and sintering of La_2TeO_6) E_α

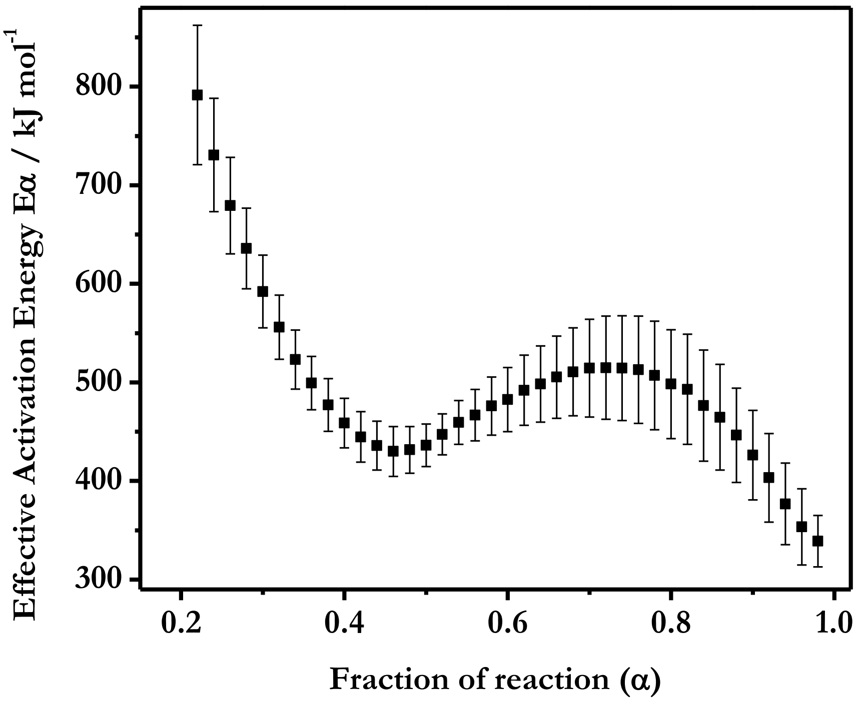

Fig. 7.6 A plot of effective activation energy (Eα) vs extent of reaction (α)

Increases with α. In the last region, due to competitive processes of diffusion of oxygen and growth of La_2TeO_6 nuclei E_α decreases with α. The effective E_α values for the formation reaction vary from 350 to 790 kJ mol^{-1}. In order to get further insight into the reaction mechanism isothermal kinetic studies on the formation of La_2TeO_6 were carried out.

7.3.2 Isothermal Kinetics

In order to determine the nature of the formation reaction (accelerating or decelerating etc.) the conversion curves obtained from isothermal experiments were used [9]. Under isothermal conditions the reaction rate is influenced only by f(α) [k(T) = constant in this case]. Hence isothermal experiments can give reliable information on the reaction model which describes the nature of the formation reaction. Conversion curves obtained from isothermal experiments at 1025 and 1045 K are shown in Fig. 7.7. It is clear from these curves that the reaction follows decelerating model.

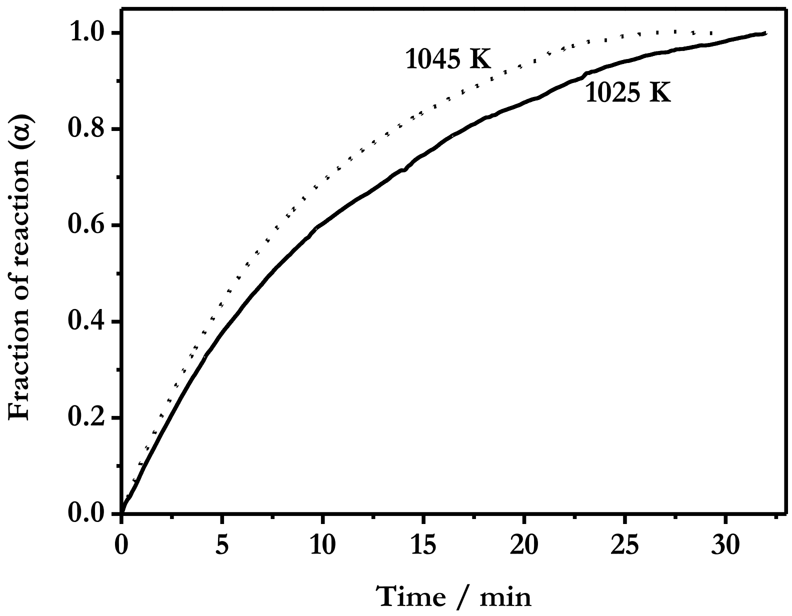

Fig. 7.7 A plot of fraction of reaction as a function of time at temperatures 1025 K and 1045 K

The melting point of TeO_2 is 1006 K. Hence, there is a possibility of loss of TeO_2 due to volatilization during experimental conditions. In order to exclude the possibility of significant loss of TeO_2 during the reaction, the amount of Te in the reaction product was measured by energy dispersive X-Ray fluorescence (EDXRF) and neutron activation analysis (NAA) techniques. The amount of La and Te in the reaction product was estimated by using the calibration plot. The results of the analyses confirmed that the loss of Te during the reaction was insignificant. The amount of Te in the sample obtained after heat treatment of the reaction mixture isothermally at 1045 K (calculated as per stoichiometric Eqn. 7.3 with material balance) was found to be in good agreement with those obtained from NAA experiments as shown in Table 7.1.

Table 7.1 EDXRF and NAA results for quantification of Te and La

	EDXRF		NAA		
	Te ppm	La ppm	^{131m}Te 150 keV γ ppm	La 487 keV γ ppm	La 1596 keV γ ppm
	182	444	191	420	425
	185	460	181	426	422
	196	487	198	423	426
	194	472	188	415	420
	188	417	183	441	411
	185	446	191	421	399
	203	391	198	428	423
Mean	190	445	190	425	418
S.D.	8	33	7	8	10
% error	4.2	7.4	3.7	1.9	2.4

In addition to this, EDS studies of the product obtained from heating of the reaction mixture at 1045 K showed the concentrations of La and Te to be in the atom ratio of 2:1 (La Lα (25.26 at.%) Te Lα (12.27 at.%)) which further confirmed that the loss of Te was insignificant.

From the above studies it is concluded that the loss of Te due to its volatilization during isothermal experiments is insignificant. The incompleteness of formation reaction during isothermal experiments at 1025 K and 1045 K is due to sluggish nature of the reaction at these temperatures.

7.4 Mechanism of formation of Lanthanum tellurate

The reaction mechanism can be deduced from the variation in the slope of the plot of $(E_a)_\alpha$ vs α. Since the isoconversional analysis of non-isothermal TG data is a model-free approach by definition, it does not permit conclusions regarding the reaction mechanism. Hence the complex nature of the mechanism of formation can be sorted out by model fit approach reported by Coats and Redfern [Eqn. (7.10)]. This approximation was used to obtain the most probable reaction mechanism [17].

$$\ln\left[\frac{g(\alpha)}{T^2}\right] = \ln\left[\frac{AR}{E_a\beta}\left(1-\frac{2RT}{E_a}\right)\right] - \left[\frac{E_a}{RT}\right] \qquad (7.10)$$

where g(α) function describes the mechanism of the reaction. The probable mechanism was chosen based on the best linear fit ($\ln\left[\frac{g(\alpha)}{T^2}\right]$ vs 1/T) with highest correlation coefficient and lowest standard deviation. Different models (Table 7.2) were chosen to describe the reaction mechanism.

Table 7.2 Set of reaction models used in this study

Model	Integral form g(α)
Nucleation models	
Power Law Pn (n=2,3,4)	$\alpha^{1/n}$
Avarami-Erofe'ev An (n=2,3,4)	$\left[-\ln(1-\alpha)\right]^{1/n}$
Geometrical contraction models	
Contracting Area (R2)	$\left[1-(1-\alpha)^{1/2}\right]$
Contracting Volume (R3)	$\left[1-(1-\alpha)^{1/3}\right]$
Diffusion models	
1 D Diffusion (D1)	α^{2}
2 D Diffusion (D2)	$(1-\alpha)\ln(1-\alpha)+\alpha$
3 D Diffusion (D3) , Jander	$\left[1-(1-\alpha)^{1/3}\right]^{2}$
3 D Diffusion (D4), Ginstling and Brounstein	$[(1-2\alpha/3)-(1-\alpha)^{2/3}]$
Reaction-order models	
First-order (F1)	$-\ln(1-\alpha)$
Second-order (F2)	$1/(1-\alpha)$
Third-order (F3)	$\left[1/(1-\alpha)^{2}\right]$

It is observed in the present study that no single model could describe the mechanism of the complete formation of La_2TeO_6. During the initial stage of the reaction (α=0 to 0.44), the process is dominated by reaction order model. Second order reaction, F2, is found to be the reaction mechanism which show that La_2TeO_6 nuclei form as reaction progresses, the growth of which did not control the kinetics. Second order reaction F2, third order reaction F3 mechanisms have been found probable for the homogeneous systems [18]. During the formation of La_2TeO_6 under the present experimental conditions, there are chances of TeO_2 local melting. During the second stage (α = 0.44 to 0.74) increase of E_α with α is due to nucleation and two dimensional growth of the reaction product represented by Avrami Erofeev A3 model, R3-area contraction and sintering of La_2TeO_6 nuclei, F1-first order reaction model and D3-Jander's equation of diffusion. For higher values of α, reaction mechanism represented by A3, R3, F1 models were found to be appropriate. Due to their combined effect, E_α decreases with α which clearly shows the complex nature of the formation of La_2TeO_6.

7.5 Conclusions

The kinetics of formation of lanthanum tellurate was studied under non-isothermal as well as isothermal conditions. The activation energy for this formation reaction under non-isothermal conditions using model-free isoconversional method was found to vary between 335 to 790 kJ mol^{-1}. The decelerating nature of this reaction was predicted using isothermal experiments. The formation of lanthanum tellurate was found to be complex in which a number of parallel reactions were found to be operative over different regions of reaction.

References

[1] Kleykamp H. Chemical States of the Fission Products in Oxide Fuels. J Nucl Mater. 1985; 131: 221-46.

[2] Cordfunke E H P, Konings R J M. Chemical interaction in water cooled nuclear fuel: a thermochemical approach. J Nucl Mater. 1988; 152: 301-09.

[3] Pankajavalli R, Jain A, Babu R, Ananthasivan K, Anthonysamy S, Ganesan V. Thermodynamic characterization of lanthanum tellurate. J Nucl Mater. 2010; 397: 116-21.

[4] Neumann A, Walter D. Investigation on the thermal decomposition of aged La_2O_3. Thermochim Acta. 2006; 445: 200-04.

[5] Shu Q, Liu J, Zhang J, Zhang M. The thermal transformation from lanthanum hydroxide to lanthanum hydroxide oxide. J Univ Sci Technol B Mineral Metallurgy Material. 2006; 13: 456-60.

[6] Jain A, Joseph K, Anthonysamy S, Gupta G S. Kinetics of oxidation of boron powder. Thermochim Acta. 2011; 514: 67-73.

[7] Brown M E, Dollimore D, Galwey A K. Comprehensive Chemical Kinetics, Vol 22. Elsevier: Amsterdam; 1988. pp. 99.

[8] Sestak J. Thermophysical Properties of Solids Comprehensive Analytical Chemistry, Vol 12 D. Elesvier: Amsterdam; 1984.

[9] Vyazovkin S, Burnham A K, Criado J M, Maqueda L A P, Popescu C, Sbirrazzuoli N. ICTAC Kinetics Committee recommendations for performing kinetic computations on thermal analysis data. Thermochim Acta. 2011; 520: 1-19.

[10] Vyazovkin S, Wight C A. Model-free and model-fitting approaches to kinetic analysis of isothermal and nonisothermal data. Thermochim Acta. 1999; 340-41: 53-68.

[11] Vyazovkin S, Wight C A. Kinetics in solids. Annu Rev Phys Chem. 1997; 48: 125-49.

[12] Grigiante M, Brighenti M, Antolini D. Analysis of the impact of TG data sets on activation energy (E_a). J Therm Anal Calorim. 2017; DOI: 10.1007/s10973-017-6122-x.

[13] Vyazovkin S. A unified approach to kinetic processing of nonisothermal data. Int J Chem Kinet. 1996; 28: 95-101.

[14] Vyazovkin S, Sbirrazzuoli N. Isoconversional kinetic analysis of thermally stimulated processes in polymers. Macromol Rapid Commun. 2006; 27: 1515-32.

[15] Akahira T, Sunose T. Trans Joint Convention of Four Electrical Institutes, 1969; 246 Research Report, Chiba Institute of Technology, Sci Technol. 1971; 16: 22-31.

[16] Maiti S C, Ghoroi C. Thermo-kinetic analysis of Ni–Al intermetallic phase formation in powder system. J Therm Anal Calorim. 2016; 124: 1039. DOI: 10.1007/s10973-015-5171-2.

[17] Coats A N, Redfern J P. Kinetic parameters from thermogravimetric data. Nature. 1964; 201: 68-69.

[18] Galwey A K. The thermal decomposition of salts of mellitic acid Part I, Aluminium mellitate and natural mellite. J Chem Soc. 1965; 5433-38.

Chapter 8

Summary and Conclusions

8

This chapter summarizes the results of the work presented in the thesis. The principal objective of this study is to carry out thermochemical studies on oxide nuclear fuel materials. The conclusions drawn based on several investigations that are centralized about this objective are elaborated in this chapter.

8.1 Measurement of oxygen potential of urania-plutonia solid solution $(U_{0.54}Pu_{0.46})O_{2-x}$

Oxygen potentials of unirradiated urania-plutonia solid solution $(U_{0.54}Pu_{0.46})O_{2-x}$were measured by using gas equilibration coupled with EMF technique in the temperature range 1073 – 1473 K and O/M range 1.98 to 2.00. The oxide sample was characterized by chemical analysis and XRD. Ar-H_2 gas mixture saturated with H_2O vapour was used as the carrier gas (equilibration gas mixture) for fixing the oxygen potential in the gas phase. Complete equilibration between sample and gas phase was ensured by the constancy in the value of EMF measured between reference electrode (a mixture of In/In_2O_3) and the sample electrode (equilibration gas mixture) of the electrochemical oxygen sensor. The total error in the values of oxygen potential measured in this study was ±2 kJ mol^{-1} and ±0.001 in O/M. The studies led to the following conclusions:

1. XRD pattern showed that the MOX pellets of $(U_{0.54}Pu_{0.46})O_{2-x}$ were single phasic and homogenous. The lattice parameter of the sample was found to be 5.439 Å.
2. The oxygen potential of $(U_{0.54} Pu_{0.46})O_{2-x}$ obtained in this study was found to increase with temperature and O/M ratio.
3. In the present study reduction of MOX pellets of composition $(U_{0.54}Pu_{0.46})O_{2-x}$ below an O/M = 1.985 did not occur. The resistance to reduction in O/M observed in this

study suggests that perhaps one of the fcc phases segregated (with an O/M close to 2.00) inhibited further reduction.

4. From the temperature dependence of oxygen potential at fixed O/M, partial molar quantities (enthalpy and entropy) were calculated in the present study. The values of partial molar enthalpy and the partial molar entropy are -752.4 kJ mol^{-1} and 0.25 kJ mol^{-1} K^{-1} respectively.

8.2 Thermodynamic stability of Cr_2TeO_6, Fe_2TeO_6, Ni_3TeO_6 by transpiration technique

The thermodynamic stabilities of Cr_2TeO_6, Fe_2TeO_6 and Ni_3TeO_6 were determined in the temperature range 1183 - 1293 K, 1103 - 1203 K and 1143 - 1272 K respectively by employing transpiration technique. Thermodynamic stabilities of these ternary oxides (Cr_2TeO_6, Fe_2TeO_6 and Ni_3TeO_6) were obtained by measuring the vapour pressure of volatile TeO_2 using oxygen as carrier gas. The present study served to obtain thermodynamic information of the above compounds and also in deducing the possibility of formation of these phases in a nuclear reactor and in gaining better understanding of the clad corrosion. The studies led to following conclusions:

1. The temperature dependence of standard Gibbs energy of formation of the above tellurates can be expressed as follows:

$$\Delta G_f^o\ (Cr_2TeO_6, s) / (kJ\ mol^{-1}) \pm 4.3 = -1620.5 + 0.5326\ T\ (K)\quad (1183<T/K<1293)$$

$$\Delta G_f^o (Fe_2TeO_6, s) / (kJ\ mol^{-1}) \pm\ 7.0 = -1271.1 + 0.506\ T(K)\quad (1103<T/K<1203)$$

$$\Delta G_f^o (Ni_3TeO_6, (s)) /\ (kJ\ mol^{-1}) \pm\ 11.0 = -1229.8 + 0.556T\ (K)\ (1143<T/K<1272)$$

2. An average 'second-law' enthalpy of formation value of -1622.5 ± 4.1 kJ mol^{-1} at 1238 K, -1273.7 ± 6.5 kJ mol^{-1} at 1153 K and -1232.5 ± 11 kJ mol^{-1} at 1208 K were obtained for Cr_2TeO_6, Fe_2TeO_6 and Ni_3TeO_6 respectively, where temperature mentioned above is the mean temperature of measurement.

3. There is a possibility of formation of Cr_2TeO_6 phase at higher O/M ratio (higher burn up) upon Te attack on SS clad.

8.3 Thermochemical studies on Cr-Te-O system using EMF technique

In the present study the thermodynamic stabilities of Cr_2TeO_6, $Cr_2Te_3O_9$ and $Cr_2Te_4O_{11}$ in the temperature range 684 - 877 K, 725 - 824 K and 704 - 878 K respectively were obtained using solid state EMF technique. Oxygen potential over various phase fields was determined using a two compartment cell assembly. The co-existence of these phases was confirmed by phase equilibration studies. The studies led to following conclusions:

1. The temperature dependence of standard Gibbs energy of formation of these compounds can be expressed as follows:

$\Delta_f G^o\ Cr_2TeO_6(s) = -1624.3 + 0.5346\ T$	Cell I	(685<T/K<723)
$\Delta_f G^o\ Cr_2TeO_6(s) = -1644.2 + 0.5606\ T$	Cell II	(725<T/K<877)
$\Delta_f G^o\ Cr_2Te_3O_9(s) = -2169.2 + 0.8817\ T$	Cell III	(725<T/K<874)
$\Delta_f G^o\ Cr_2Te_4O_{11}(s) = -2458.2 + 1.013\ T$	Cell IV	(705<T/K<843)
$\Delta_f G^o\ Cr_2Te_4O_{11}(s) = -2503.7 + 1.077\ T$	Cell V	(725<T/K<879)
$\Delta_f G^o\ Cr_2Te_4O_{11}(s) = -2522.8 + 1.097\ T$	Cell VI	(720<T/K<856)

2. $\Delta_f G^o\ Cr_2TeO_6$ values obtained from two different techniques (EMF and transpiration) were found to be in excellent agreement with each other and also with the values reported

in the literature. Δ_fG^o of $Cr_2Te_3O_9$(s) and $Cr_2Te_4O_{11}$(s) were reported for the first time in this study. The values of Δ_fG^o $Cr_2Te_4O_{11}$(s) obtained using cells IV, V and VI match very well.

3. There is a possibility of formation of these compounds at higher O/M ratio (O/M >2) (higher burn up) upon Te attack on SS clad.

8.4 Thermochemical studies on Cr_2TeO_6, Fe_2TeO_6, Ni_3TeO_6, $Ni_2Te_3O_8$ and $NiTe_2O_5$ using calorimetric technique

In this study enthalpy increments of the above compounds have been measured using isoperibol type high temperature calorimeter. Enthalpy increments of samples were determined and fitted in a polynomial of type AT + BT^2 + C/T +D using constraints (a) $H^o_T - H^o_{298K} = 0$ at T = 298 K (b) the derivative of this function at 298 K is equal to the value of the heat capacity of the respective compound. From the measured enthalpy increments other thermodynamic properties viz., heat capacity, entropy and free energy function (FEF) have been derived. Using FEF values enthalpy of formation of these compounds at 298 K has been calculated using 'third-law'. The studies led to following conclusions:

1. The temperature dependence of enthalpy increments of these compounds can be expressed as follows:

$H^o_T - H^o_{298K}$ (Cr_2TeO_6)/ (J mol^{-1}) =

$$206.11\,(T\,/\,\mathrm{K}) + 3.443 \times 10^{-3}(T\,/\,\mathrm{K})^2 + 9.689 \times 10^3\,(\mathrm{K}/\,T) - 65009 \qquad (373<T/\mathrm{K}<973)$$

$H^o_T - H^o_{298K}$ (Fe_2TeO_6) / (J mol^{-1}) =

$213.04\,(T\,/\,\mathrm{K}) + 25.462 \times 10^{-3}\,(T/\mathrm{K})^2 + 56.304 \times 10^5\,(\mathrm{K}\,/\,T) - 84665$ $(483<T/\mathrm{K}<1083)$

$H^o_T - H^o_{298K}$ (Ni_3TeO_6) / (J mol^{-1}) =

$247.704\,(T\,/\,\mathrm{K}) + 4.397 \times 10^{-3}\,(T/\mathrm{K})^2 + 52.817 \times 10^5\,(\mathrm{K}/\,T) - 91959$ $(483<T/\mathrm{K}<1087)$

$H^o_T - H^o_{298K}$ $(Ni_2Te_3O_8)$/ (J mol^{-1}) =

$318.809(T/\mathrm{K}) + 16.932\mathrm{x}10^{-3}(T/\mathrm{K})^2 + 43.278\mathrm{x}10^5(\mathrm{K}/T) -111073$ $(483<T/\mathrm{K}<1087)$

$H^o_T - H^o_{298K}$ $(NiTe_2O_5)$/ (J mol^{-1}) =

$156.312(T/\mathrm{K}) + 27.773\mathrm{x}10^{-3}(T/\mathrm{K})^2 + 1.621\mathrm{x}10^5(\mathrm{K}/T) - 49617$ $(483<T/\mathrm{K}<1087)$

2. From the measured enthalpy increment values other thermodynamic parameters viz., heat capacity, entropy and free energy function (FEF) were derived.

3. From the derived FEF, $\Delta H^o_{f,298K}$ was computed from the 'third-law' analysis of vapour pressure data of Cr_2TeO_6, Fe_2TeO_6, Ni_3TeO_6. $\Delta H^o_{f,298K}$ was found to be -1636.9 ± 0.8 / (kJ mol^{-1}) for Cr_2TeO_6, -1318.1 ± 0.9 / kJ mol^{-1} for Fe_2TeO_6 and -1265.1 ± 1.5 kJ mol^{-1} for Ni_3TeO_6(s).

8.5 Kinetics of formation of La_2TeO_6

The kinetics of formation of La_2TeO_6 in the temperature range 1023 – 1203 K was studied by means of thermogravimetric (TG) technique. The kinetics of formation was studied by carrying out the TG experiments under isothermal as well as non-isothermal conditions. Model-free isoconversional method (Kissinger-Akahira-Sunose (KAS)) was employed to derive the kinetic parameters and to establish the dependence of effective activation energy on progress of the formation reaction. The studies led to following conclusions:

1. The activation energy for the formation reaction under non-isothermal conditions using model-free isoconversional method was found to vary between 335 to 790 kJ mol^{-1}
2. The decelerating nature of the reaction was predicted using isothermal experiments.
3. The formation of lanthanum tellurate was found to be complex in which a number of parallel reactions were found to be operative over different regions of reaction.

Chapter 9

Future Perspectives

9

9.1 Scope for future studies

In the present study oxygen potential of (U, Pu) mixed oxide $(U_yPu_{1-y})O_{2\pm x}$ fuel containing 46 mol.% plutonium has been measured. There are many reports on the oxygen potential of (U, Pu) mixed oxides containing up to 30 mol.% of plutonium. It will be of interest to measure the oxygen potential of urania - plutonia solid solutions over the entire composition range (O/M ratio and Pu content). From the dependence of x on the oxygen partial pressure the defect structure of $(U_yPu_{1-y})O_{2\pm x}$ can be explained. The defect structure can be elucidated based on the defect model consisting of interstitial oxygen (Type-I and II) and oxygen vacancies (Willi's model for $UO_{2\pm x}$) [1].

XPS studies can also be carried out to determine U and Pu valency in $(U_yPu_{1-y})O_{2\pm x}$ solid solution as a function of x. This study will help in estimating oxygen potential of MOX fuel as a function of nonstoichiometry.

A thermogravimetric analyzer can be employed for on-line weight change monitoring. It will not only reduce the error in O/M measurement but also facilitate studies on the kinetics of oxidation of $(U_yPu_{1-y})O_{2\pm x}$ and establishing mechanism of oxidation of the mixed oxides.

Stabilities of a few tellurate and tellurite phases in the ternary system Cr-Te-O, Fe-Te-O and Ni-Te-O are determined in the present study. Thermodynamic stability of other phases which can be formed by Te attack on SS components i.e., Fe, Cr, Ni, Mn etc (tellurides, tellurites and tellurates) whose data are not available in the literature can also be studied.

In the present study, enthalpy increments of various ternary compounds were measured and fitted into a polynomial of temperature. For fitting, the value of heat capacities at 298.15 K of a few compounds which were not available in the literature were obtained by Neumann-Kopp rule (molar addition of respective component oxides). Hence, studies can be carried out to measure their heat capacities using low temperature calorimetric techniques.

References

1. Willis B T M. Structures of UO_2, UO_{2+x} and U_4O_9 by neutron diffraction. J de Phys. 1964; 25(5): 431-39.

Appendix 1

Some of the important thermodynamic properties of tellurium and tellurium dioxide

Property	Te	TeO_2
Melting Point / K	723 [1]	1006 [1]
Boiling Point / K	1327 [1]	1518 [1]
Heat of sublimation / kJ mol^{-1}	2 Te (s) → Te_2 (g)	TeO_2 (s) → TeO_2 (g)
$\Delta_{sub}H^{o}_{m,298K}$	158 ± 6.6 [2]	272.5 ± 3.8 [3]

References –

1. Knacke O, Kubaschewski O, Hesselmann K. Thermochemical Properties of Inorganic Substances. 2nd ed. Germany: Springer-Verlag; 1991.
2. Viswanathan R, Balasubramanian R, Darwin Albert Raj D, Sai baba M, Lakshmi Narasimhan. Vaporization studies on elemental tellurium and selenium by Knudsen effusion mass spectrometry. J Alloys Compd. 2014; 603: 75-85.
3. Lakshmi Narasimhan T S, Balasubramanian R, Nalini S, Sai baba M. Vaporisation studies on tellurium dioxide: A Knudsen effusion mass spectrometric study. J Nucl Mater. 1997; 247: 28-32.